Design and Control of Hydrogen Supply and Recirculation System for Proton Exchange Membrane Fuel Cell Systems

by

Keda Xu
M.Sc., Tongji University, 2011
B.Eng., Nanjing Tech University, 2008

A Thesis Submitted in Partial Fulfillment
of the Requirements for the Degree of

Master of Applied Science

in the Department of Mechanical Engineering

Supervisory Committee

Design and Control of Hydrogen Supply and Recirculation System for Proton Exchange Membrane Fuel Cell Systems

by

Keda Xu

M.Sc., Tongji University, 2011

B.Eng., Nanjing Tech University, 2008

Supervisory Committee

Dr. Zuomin Dong, Department of Mechanical Engineering

Supervisor

Dr. Rustom Bhiladvala, Department of Mechanical Engineering

Departmental Member

Abstract

Proton Exchange Membrane Fuel Cell (PEMFC) systems require more than the theoretically needed hydrogen (H_2) fuel gas in the anode supply system to achieve high performance and extended operating life. The ejector-based H_2 supply and recirculation system (HSRS) is superior to its mechanical pump-based counterpart, with reduced operation and maintenance costs, low noise, and zero parasitic power consumption. However, the conventional ejector with fixed dimensions of a nozzle can only function within a narrow power range of PEMFC due to its restricted primary inlet pressure and mass flow rate. The ejector theoretical background and analytic models are reviewed to understand its working principles better. The ejector H_2 entrainment capabilities are affected by the key geometric parameters, including nozzle diameter (D_n), mixing chamber diameter (D_m) and its length (L_m), and the distance between the nozzle exit and the mixing chamber (*NXP*), as well as PEMFC system operating conditions such as anode pressure, temperature, and relative humidity. All these factors have been thoroughly investigated and analyzed using computational fluid dynamics (CFD) simulations.

This research presented an optimal design of a nested-nozzle ejector to satisfy the H_2 stoichiometric ratio (SR_{H_2}) for a wide power output range of the PEMFC stack. The nested-nozzle ejector consists of one large nozzle (BN) and one small nozzle (SN) with shared suction, mixing, and diffuser chamber. The BN mode was responsible for the stack high load conditions, while the SN mode performed at low load conditions. A bypass was adopted parallel to the nested-nozzle ejector in HSRS to extend the ejector operating range. The key geometric parameters, including nozzle diameters and the distance between two nozzles, were optimized using CFD simulations to maximize the ejector's H_2 entrainment capability. The results demonstrated that the optimally designed ejector could provide adequate H_2 gas entrainment to satisfy the stack SR_{H_2} from around 9% to 100% output power of a 150 kW PEMFC stack. The nested-nozzle ejector was produced, and a test bench was established to measure the ejector entrainment performance using air. Moreover, the nested-nozzle ejector was compared with the dual-ejector system using two conventional ejectors in terms of the operating range and anode inlet pressure fluctuation.

The results showed that the nested-nozzle ejector could greatly reduce the system pressure fluctuation while fulfilling the requested anode SR_{H_2}.

Moreover, a supervised machine learning (ML) model is developed using a data-driven approach based on CFD simulation results to predict the H_2 entrainment capability of both conventional and nested-nozzle ejectors. The least-squares estimator is applied to obtain the optimal weight $\widehat{w}^*$ of the linear regression ML model. The predicted H_2 entrainment capability showed good consistency with the results from CFD simulations. The trained linear regression ML model can also be used to optimal design the ejector key geometric parameters by solving a formulated linear programming (LP) problem. Compared to traditional CFD simulation methods, this approach can greatly simplify the ejector design and simulation process. Based on the ML model, the entertainment performance of the optimized ejector was validated using CFD simulations on small, middle and large-size PEMFC stacks, showing less than 8 percent mean absolute percentage error.

Dynamic models of main components in HSRS and PEMFC system controller were developed using model-based design method in MATLAB/Simulink. Integrated with the existing PEMFC stack model and air supply system model, a closed-loop PEMFC system simulator was completed to validate the accuracy and transit behaviour of system models. The system performance is validated in a 150kW PEMFC system with a nested-nozzle ejector and a bypass. The simulation results demonstrated that the rule-based control strategies using feedforward together with PI control for air supply system and PI feedback control for HSRS can provide rapid response of system models during dynamic load inputs. The integrated system model can be beneficial to the actual product design and system development.

Table of Contents

List of Tables

List of Figures

List of Abbreviations

BN	Large nozzle
BOP	Balance of plant
BPVC	Back pressure valve and controller
CD	Convergent divergent
CFD	Computational fluid dynamics
CGH2	Compressed gaseous hydrogen
DOE	Department of energy
FCEV	Fuel cell electric vehicle
GHG	Greenhouse gas
HSRS	Hydrogen supply and recirculation system
ICE	Internal combustion engine
LP	Linear programming
MAPE	Mean absolute percentage error
MEA	Membrane electrolyte assembly
MFC	Mass flow rate controller
MFM	Mass flow rate meter
ML	Machine learning
NLPM	Normal liter per minute
PEMFC	Proton Exchange Membrane Fuel Cell
PI	Proportional integral
PT	Pressure and temperature sensor
PV	Proportional valve
PWM	Pulse-width modulation
RH	Relative humidity
RMSE	Root mean squared error
SN	Small nozzle
SR	Stoichiometric ratio

Nomenclature

P	pressure
ρ	density
R	gas constant
T	temperature
A	area
h	enthalpy
P_0	stagnation pressure
T_0	stagnation temperature
ρ_0	stagnation density
M	Mach number
γ	specific heat ratio
u	velocity
P_b	back pressure
P_*	pressure of the choked flow
T_*	temperature of the choked flow
ρ_*	density of the choked flow
u_*	velocity of the choked flow
$\dot{m}_*$	mass flow rate of the choked flow
A_*	nozzle throat area
u_r	velocity of secondary flow at section 2 along vertical direction
u_{p2}	primary flow velocity along vertical direction of section 2
k_{eff}	thermal conductivity
h_c	enthalpy of species
J_c	diffusive flux of species
Y_c	mass fraction
ω_{H_2}	H_2 entrainment ratio
λ_{H_2}	H_2 entrainment capability
SR_{H_2}	anode H_2 stoichiometric ratio
$\dot{m}_p$	mass flow rate of primary flow
$\dot{m}_s$	mass flow rate of secondary flow
y_{H_2}	H_2 mass fraction in anode outlet mixture
N_{cell}	cell number of the fuel cell stack
I	fuel cell stack current

F	Faraday constant
M_{H_2}	H_2 molar weight
D_n	nozzle's throat diameter
P_p	primary inlet pressure
T_p	primary inlet temperature
C_d	nozzle discharge coefficient
M_{N_2}	N_2 molar weight
M_{H_2O}	H_2O molar weight
P_{sat}	water saturation pressure
P_{N_2}	partial pressure of N_2
P_{H_2}	partial pressure of H_2
D_m	mixing chamber diameter
L_m	mixing chamber length
NXP	the distance between nozzle exit and mixing chamber inlet
L_d	diffuser chamber length
α_d	diffuser chamber divergent angle
$A_{s,p}$	secondary flow area at the mixing section
P_s	secondary inlet pressure
ω	entrainment ratio
D_{BN}	large nozzle diameter of nested-nozzle ejector
D_{SN}	small nozzle diameter of nested-nozzle ejector
L_N	distance between large nozzle and small nozzle
V_{s,N_2}	N_2 volumetric ratio in the secondary mixture
V_{s,H_2O}	water vapour volumetric ratio in the secondary mixture
V_{s,H_2}	H_2 volumetric ratio in the secondary mixture
P_d	ejector outlet pressure
$\dot{m}_{pB}$	large nozzle mass flow rate
$\dot{m}_{pS}$	small nozzle mass flow rate
$\dot{m}_{p,max}$	stack maximum theoretical H_2 consumption rate
$\dot{m}_{pv,max}$	maximum H_2 mass flow rate of proportional valve
P_{pB}	primary pressure of the large nozzle
$\dot{m}_{fc,max}$	maximum H_2 mass flow rate of stack
$\omega_{air,test(i)}$	air entrainment ratio from tests
$\omega_{air,CFD(i)}$	air entrainment ratio from CFD simulations
dP_d	anode inlet pressure fluctuation

x_i	feature vector
$\tilde{y}$	predicted ejector H_2 entrainment performance by ML
$\widehat{w}$	wight vector of the linear model
$\widehat{w}^*$	optimal weight vector of the linear model
$\hat{x}$	feature vector of the linear model
m	sample numbers of feature vector of the linear model
$e(\widehat{w})$	least-squared estimator
y_n	single ground truth sample from the training data set
N	sample numbers of the training data set
$\hat{X}_{tr}$	sample set of the training data
y_{tr}	ground truth set of the training data set
$\hat{X}_{te}$	sample set of the testing data
y_{te}	ground truth set of the testing data
$y_{\lambda_{H_2}}$	predicted H_2 entrainment capability using ML
φ_{et}	energy loss coefficient
$P_{st,ini}$	H_2 storage tank initial pressure
V_{st}	H_2 storage tank volume
$m_{st,ini}$	H_2 storage tank initial mass
$T_{st,ini}$	H_2 storage tank initial temperature
m_{st}	H_2 storage tank remaining mass
$\dot{m}_{st,out}$	H_2 storage tank outlet mass flow rate
ρ_{CGH2}	compressed H_2 density
$P_{st,out}$	H_2 storage tank outlet pressure
$\dot{m}_{prv,in}$	pressure reducing valve inlet mass flow rate
$P_{prv,in}$	pressure reducing valve inlet pressure
$T_{prv,in}$	pressure reducing valve inlet temperature
$\dot{m}_{prv,out}$	pressure reducing valve outlet mass flow rate
$P_{prv,out}$	pressure reducing valve outlet pressure
$T_{prv,out}$	pressure reducing valve outlet temperature
$P_{pv,in}$	proportional valve inlet pressure
$P_{pv,out}$	proportional valve outlet pressure
Q_N	proportional valve volumetric flow rate
k_v	flow coefficient
ρ_N	standard gas density
$T_{pv,in}$	proportional valve inlet temperature

$\dot{m}_{pv,out}$	proportional valve outlet mass flow rate
$\dot{m}_{pv,in}$	proportional valve inlet mass flow rate
$T_{pv,out}$	proportional valve outlet temperature
$\emptyset_s$	relative humidity of the secondary mixture
$\dot{m}_{an,out}$	anode outlet mass flow rate
P_{s,H_2O}	water vapour partial pressure in a secondary mixture
P_{s,N_2}	N_2 partial pressure in the secondary mixture
P_{s,H_2}	H_2 partial pressure in a secondary mixture
$\dot{m}_{d,H_2}$	H_2 mass flow rate at the ejector outlet
$\dot{m}_{d,N_2}$	N_2 mass flow rate at the ejector outlet
$\dot{m}_{d,H_2O}$	water vapour mass flow rate at ejector outlet
$\dot{m}_d$	total mass flow rate at ejector outlet
T_d	ejector outlet temperature
v_p	flow velocity at ejector primary inlet
v_s	flow velocity at ejector secondary inlet
v_d	flow velocity at ejector outlet
C_{p,H_2}	H_2 specific heat at constant pressure
C_{p,N_2}	N_2 specific heat at constant pressure
C_{p,H_2O}	water vapour specific heat at constant pressure
$C_{p,Mix}$	mixture specific heat at constant pressure
$\dot{m}_{an,in,H_2}$	total H_2 mass flow rate entering the anode
$\dot{m}_{an,out,H_2}$	H_2 mass flow rate leaving the anode
$\dot{m}_{an,reacted,H_2}$	H_2 mass flow rate consumed by the stack theoretically
$\dot{m}_{by,H_2}$	H_2 mass flow rate supplied by the bypass channel
$\dot{m}_{an,in,VH_2O}$	water vapour mass flow rate entering the anode
$\dot{m}_{an,out,LH_2O}$	liquid water mass flow rate leaving the anode
$\dot{m}_{mem,VH_2O}$	water vapour mass flow rate transferring through the membrane
$\dot{m}_{an,in,N_2}$	N_2 mass flow rate entering the anode
$\dot{m}_{an,out,N_2}$	N_2 mass flow rate leaving the anode
$\dot{m}_{mem,N_2}$	N_2 mass flow rate transferring through the membrane
$\emptyset_{an,in}$	anode inlet relative humidity
$T_{an,in}$	anode inlet temperature
P_{an,H_2}	H_2 partial pressure in the anode flow channel
P_{an,H_2O}	water vapour partial pressure in the anode flow channel
P_{an,N_2}	N_2 partial pressure in the anode flow channel
T_{st}	stack temperature

V_{an}	anode flow channel volume
$P_{an,in}$	anode inlet pressure
$\emptyset_{an}$	anode relative humidity
$P_{an,out}$	anode outlet pressure
$\emptyset_{an,out}$	anode outlet relative humidity
P_{an,out,VH_2O}	anode outlet water vapour pressure
$\dot{m}_{an,out}$	anode outlet mixture mass flow rate

Acknowledgments

I would like to express my sincere gratitude to my supervisor, Dr. Zuomin Dong, for his invaluable guidance and full support during my Master of Applied Science program. His professional knowledge and wide perspectives have encouraged me in all the time of my academic research. I am also extremely thankful to my committee members for their time and effort in reviewing this work.

Besides, I also want to thank all of my colleagues who helped set up the ejector test bench and provided their valuable advice and discussions on the ejector manufacturing.

Finally, I would like to say thank you to my family, without whose support and encouragement this work would have never been done.

Dedication

This dissertation is dedicated to my wife Lily and our children Jean and Daniel.

Chapter 1 Introduction

1.1 Background

The growing human activities led to the global warming issue, which has increased the global average temperature by almost 1℃ [1] during the last twenty years compared to the pre-industrial level. Greenhouse gas (GHG) emission reduction has become the priority to keep the global average temperature rise below 2℃ in this century [2]. The carbon dioxide (CO_2) accounts for around 65% among the GHG emissions emitted by human activites [3]. Road travel, which results from passenger cars, buses and trucks, contributes about 74.5% of global CO_2 emissions in transport area, while aviation and shipping account for 11.6% and 10.6% [4], respectively. Totally, transportations adopted fossil fuels such as gasoline and diesel contribute to 27% of GHG emissions in the USA [5] and 14% of global GHG emissions [3]. Various emission reduction technologies, such as turbocharged engines, gasoline direct injection, stop/start, engine cut-off, advanced transmissions and hybrid electric propulsion systems, have been adopted in conventional transportation to improve the fuel economy and reduce the emissions from internal combustion engines (ICE) since last two decades. To further satisfy the net-zero GHG emissions requirement by 2050 [6], advanced automotive propulsion systems driven by clean energy, such as electricity, biofuel and hydrogen (H_2) produced by renewable energy from wind, water and solar energy [7], are on the rise recently, with zero or low CO_2 and harmful pollutants.

The hydrogen Proton Exchange Membrane Fuel Cell (PEMFC) technology presents a promising solution to ease the environmental and energy crisis with higher efficiency and zero pump-to-wheel emissions. The fuel cell operating principle was discovered by William Grove in 1839 [8]. In the 1960s, the first PEMFC was developed by General Electric and used on NASA's human-crewed space vehicles. Due to its rapid start-up, relatively low operation temperature, and high-power density and efficiency, PEMFC has been largely applied in the automotive industry, especially on buses, trucks, forklifts, etc.

Fuel cell electric vehicles (FCEV), compared to their Li-ion battery-powered counterparts, can provide a longer driving range with faster refilling (only a few minutes). Moreover, with the rapid development in past decades, the economic life of PEMFC on

automotive vehicles is currently improved to over 5500 hours [9] compared to its early versions with less than 500 hours. And the cost of PEMFC decreased significantly from hundreds of USA dollars/kW to $46.16/kW in 2018 and is targeted at $30/kW in 2025 set by the U.S. department of energy (DOE) [10].

A single PEM fuel cell includes the following components: the membrane electrolyte assembly (MEA), gas diffusion layers, and bipolar plates. By converting the chemical energy from H_2 and O_2 directly into electricity and generates water and waste heat, the PEMFC has a higher efficiency (60 to 70%) than an ICE (30 to 40%). The membrane only allows H_2 ions pass through from the anode electrode to the cathode electrode. At the same time, electrons conduct from one bipolar plate to another, forming an external circuit to supply electricity to external loads and fuel cell system accessories. The simplified structure of a single PEM fuel cell is shown in Figure 1.

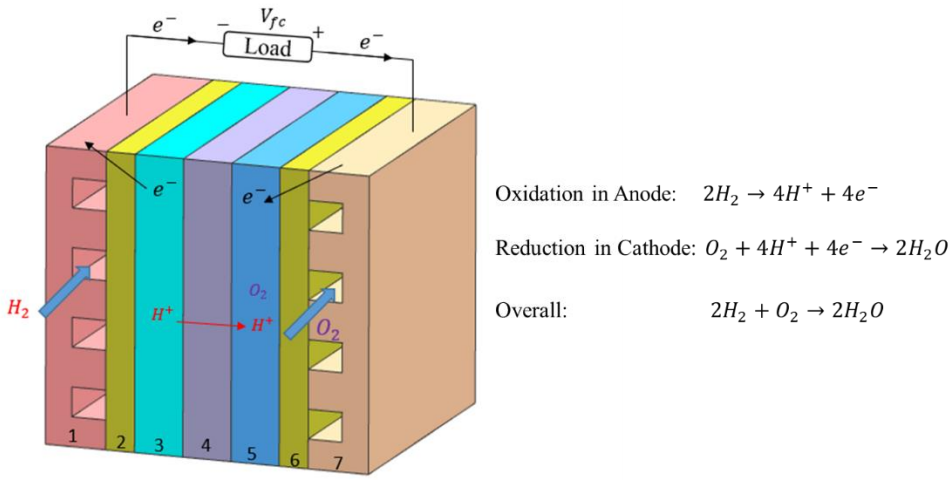

1&7: Bipolar plates 2&6: Gas diffusion layers 3&4&5: MEA
3: Anode electrode 4: Membrane and electrolyte 5: Cathode electrode

Figure 1: Schematic of a single PEMFC

The oxidation reaction occurs on the anode electrode and turns the pure H_2 reactant into positive H_2 protons and electrons, while the reduction reaction happens on the cathode electrode by consuming O_2 , electrons and H_2 iron, and produces water. The electrochemical reactions are described in Figure 1.

The PEMFC system consists of a fuel cell stack and the balance of plant (BOP), which provides vital support for the fuel cell operation. Since single PEMFC outputs no more than 1V, many single fuel cells are connected in series to form a stack to supply FCEV's

high voltage and power. The cell number of a stack depends on the required maximum output power of the PEMFC propulsion system. The BOP usually includes three subsystems:

a) the H_2 fuel supply and recirculation system (HSRS) provides H_2 gas with required pressure, mass flow rate and stoichiometric ratio (SR) to the anode inlet, and recycles the unconsumed H_2 from the anode outlet;
b) the O_2 or oxidant air supply system supplies pressurized and sufficient clean O_2 or air to the cathode using an air compressor. Also, a water separator and humidifier are needed to remove the produced water and hydrate the fresh air, respectively;
c) the water and heat management system provides sufficient hydration to the membrane and maintains a suitable operating temperature for the fuel cells.

Normally, the PEMFC stack requires excessive, more than the theoretically needed H_2 fuel gas in HSRS to avoid fuel starvation, output sufficient power, and improve the system efficiency. Considering the overall fuel economy, the unreacted H_2 through the anode flow channels should be recycled back to the stack to participate in the chemical reaction again through the recirculation devices in HSRS. The recycled H_2 is beneficial to maintain the ideal temperature, humidity, and quality of the fuel required by the stack.

Several studies have been carried out on H_2 recirculation devices, such as mechanical pumps, electrochemical pumps, and ejectors. The mechanical pump is traditionally used to recirculate the unused H_2 and has been applied in the world's first mass-produced fuel cell vehicle Toyota Mirai [11]. The pump consumes additional parasitic power from the PEMFC system, resulting in lower system efficiency and reduced net power output. Besides, the pump can cause noise and vibration, and its lubricant is a potential source of fuel cell membrane poisoning. The electrochemical pump [12] is a special single fuel cell in which the inlet and outlet are connected to the PEMFC anode outlet and inlet, respectively. The unconsumed H_2 is absorbed from the low-pressure electrode inlet to the high-pressure electrode outlet through a proton exchange membrane and then transferred to the PEMFC fuel anode. The electrochemical pump provides a wider operating range compared to the traditional mechanical pump but have drawbacks such as expensive manufacturing and maintenance cost, and increased system complexity.

Ejectors have been widely adopted in the industry, such as air conditioning, refrigeration, and aerospace systems, to replace mechanical pumps since their introduction in the early 1900s [13]. A typical ejector adopts a venturi nozzle to create a high-speed stream with low pressure to absorb the unused stream and reinject it to the main stream [14]. Recently, the gas ejector has been adopted in Hyundai Nexo and Honda Clarity [15] PEMFC vehicles, due to its superior advantages of no vibration, no noise, zero power consumption, small volume, and easy maintenance and installation. H_2 ejectors used in the PEMFC system take advantage of the considerable H_2 pressure potential energy between the high-pressure storage tank and the stack to create a pressure drop through a nozzle to pump the unused H_2 mixture. However, a significant issue of H_2 ejector with fixed geometries is that the ejector has a pressure potential energy limit due to the HSRS's accessories' specifications and stack anode operation conditions. As a result, the ejector H_2 entrainment ratio falls rapidly when the primary H_2 flow rate deviates from design points, thus resulting in a narrow operating power range.

To overcome the limited operational range issue of H_2 ejector, two main solutions have been adopted in the previous research, including improved HSRS architectures and redesigned ejector structures. The improved HSRS, such as adopting two or more parallel conventional ejectors [16, 17] and a combination of one ejector and one pump [18], can effectively recirculate the unused H_2 over a broader power range of the PEMFC stack. However, it increases the HSRS design and control complexity and may cause H_2 gas pressure fluctuation [19] in the anode flow channel due to multiple gas pathways. Another approach is to apply an ejector with a newly designed nozzle structure. The variable flow ejectors proposed in [20, 21] use a needle inside the nozzle to change its size, which can provide a considerable range of primary mass flow rate and improve overall H_2 entrainment performance. To accurately control the needle position, diaphragms [21] and one electronically controlled motor [20] are applied. The multi-nozzle ejector with a maximum of five primary nozzles was investigated by Meakhail et al. [22] and Xue et al. [23]. Han et al. [24] also presented a multi-nozzle ejector consisting of one central nozzle and two symmetrical nozzles. Moreover, Du et al. [25] introduced a coaxial two-nozzle ejector similar to the dual-nozzle ejector presented by Zhu et al. [26]. The above solutions have been demonstrated to broaden the operating power range of the PEMFC system

effectively. However, using multiple and extremely small nozzles in one ejector can present significant challenges for manufacturing and real-life applications.

The design and analysis of H_2 ejector relies on an accurate model to simulate the working flow states inside the ejector, usually described using the mass, momentum, and energy conservation equations. The most effective method is to solve these governing equations numerically using 3D computational fluid dynamics (CFD) simulation software such as ANSYS Fluent. It can provide detailed flow fields inside the ejector, including the velocity, pressure, temperature, density, species mass fraction, and mass flow rate. However, acquiring the ejector performance using CFD simulation is demanding and time-consuming.

The simplified 1D and 2D ejector models were also proposed in previous studies. The first 1D numerical model of air ejector was developed by Keenan and Neumann [27] in 1942 based on ideal gas law without considering heat and friction losses. This model was further updated by Keenan et al. [28] to introduce the 1D constant-pressure mixing theory. The constant-pressure theory assumes that the primary flow pressure is identical to the secondary flow pressure at the ejector nozzle exit, and these two flows are mixed at a uniform and constant pressure before entering the constant-area mixing chamber. Based on these analytical approaches, other ejector design methods have been carried out. Defrate et al. [29] improved the 1D constant-pressure mixing model by considering the ideal gas law with molar weight and different specific heat ratio for the primary and secondary flows. Emanuel [30] introduced a simple analytical model in terms of enthalpy to optimize the ejector steady-state performance. A further updated 1D ejector model using R141b was presented by Huang et al. [31] that the constant-pressure mixing process happens in the constant-area mixing chamber and the secondary flow is choked. Liao [32] developed a generalized model to present the relationship between the constant-pressure and constant-area 1-D models and considered the phase transition of ejector internal flow between gas and liquid. All the 1D models discussed above assume that the velocity of both primary and secondary flow is uniform at each cross section inside the ejector chamber. The simplicity in 1D model resulted in the simulation error compared to the 3D simulation method.

To describe the non-uniform velocity distribution of secondary flow near the ejector inner wall, Zhu et al. [33] presented a shock circle model by giving the 2D exponential velocity equation of the secondary flow to calculate the mean velocity and mass flow rate of the secondary flow with consideration on the energy loss of the primary and secondary flow from the inlets to the constant-area mixing chamber. A new theoretical model for gas ejector with a convergent nozzle was later developed by Zhu et al. [34] and induced a 2D concave exponential curve of flow velocity near the ejector inner wall. The 2D ejector model improved the accuracy of flow velocity along the vertical direction, however, it also increased the calculation complexity compared to 1D models. More detailed comparisons of ejector modelling methods are presented in Chapter 2.

Modelling of HSRS plays a vital role in the PEMFC system design. Research on the HSRS system model has been scarce in the literature compared to its counterpart of the cathode air supply system. It is necessary to evaluate the ejector's performance in the integrated HSRS system model considering other components' pressure and flow limitations. Moreover, the control strategy of H_2 injector and ejector should be established based on the HSRS system model to ensure the stability of pressure and mass flow of H_2 supply.

1.2 Motivation

The ejector-based HSRS in PEMFC system has presented great advantages in promoting system efficiency, reducing cost and volume, as well as easing the system vibration and noise. However, the limited working range of conventional ejector with fixed geometric dimensions needs to be improved to satisfy the wide power operation range of PEMFC in FCEVs. In addition, modelling, and control of HSRS using ejectors must be investigated to validate its performance and prove its effectiveness.

The current research on the ejector and HSRS face the following challenges:

- An innovative design that can extend the effective H_2 entrainment capability and support the wide power output range of a PEMFC system;
- Lack of a reliable ejector model that can accurately predict its entrainment performance with less computation time and resources;

- Manufacturability considerations of ejector design to produce ejectors that can be made with the desired functionality;
- Systematic evaluation of the ejector's H_2 supply and recycle performance of a HSRS.

Ejectors face harsh operation environments in real PEMFC system applications. Thus, the practical manufacturing problems must be considered, such as the product material, the minimum achievable manufactured nozzle aperture, and the nozzle's wall thickness, which greatly influences deciding the ejector's geometries and hydrogen entrainment capability.

The multi-nozzle ejectors proposed in previous studies [20-24] were produced using plastic material, instead of aluminum or stainless steel, with extremely thin wall thickness. However, this fragile manufacturing cannot survive in the practical application and can easily break overtime due to the rapid temperature change (from -200 to 350 K) around the nozzle area. Moreover, the design process of multi-nozzles without considering wall thickness in manufacturing process could result in inappropriate mixing chamber geometries which could dramatically affect the ejector H_2 entrainment ratio. Besides, more nozzles mean complex HSRS system's structure and may require more hydrogen supply devices and flow channels. Hence, these previous studies could encounter disadvantages in manufacturing, increase control difficulties in application, as well as induce potential system pressure disturbances, which are unsuitable for the practical application due to the cost and size requirement of PEMFC system.

The design and analysis of the ejector rely on an accurate model. Current 1D and 2D models have simplified the ejector flow processes and adopted several equation coefficients to denote the flow energy losses. These coefficients must be obtained from the CFD simulation or experiments and can result in a relatively large error between the model and test results. Moreover, the ejector H_2 entrainment performance is sensitive to its geometric parameters and PEMFC system operation conditions, on which any minor changes would result in large deviations in its performance. A machine-learning model can be built using a data-driven approach to solve this problem without considering the complex flow phenomena inside the ejector by taking advantage of a large amount of data from ejector CFD simulations.

This research is thus motivated to solve the two main issues mentioned above: (a) to enlarge the limited operating range restricted by the conventional gas ejector and, (b) to reduce the relatively large error caused by 1D empirical formula or semi-empirical formula models. To achieve these goals, a large PEMFC stack with maximum 150 kW output power is adopted to demonstrate the optimal design, modelling, and analysis processes. First, the key ejector geometric parameters and PEMFC operation conditions that can greatly affect its performance are identified and thoroughly analyzed. Second, a new ejector structure involving multiple nozzles is optimally designed, considering its manufacturing restrictions and accessibilities. The CFD simulation results are compared with experimental data to validate the design process. Third, a new modelling method using data-driven and machine learning algorithms is proposed to provide accurate simulation of ejector performance for single and multiple ejector applications based on acquired large amount of CFD simulation data. Finally, the components' models and control strategy of HSRS are developed to evaluate the overall system performance.

1.3 Thesis Organization

The structure of this thesis is organized as below:

Chapter 2 reviews the BOP of the PEMFC system for automotive applications. The architecture and operations of HSRS with different H_2 recirculation devices are introduced. The ejector theoretical background, existing structures and analytical models are also presented.

Chapter 3 presents the CFD simulations of single nozzle ejector using ANSYS Fluent. The key geometric parameters and PEMFC operation conditions that greatly influence the ejector entrainment performance are analyzed and determined.

Chapter 4 presents a novel design of ejector structure with nested nozzles to satisfy the H_2 stoichiometric ratio required by the PEMFC stack. The geometries of the nested-nozzle ejector are optimized through CFD simulations, and a test bench is built to validate the H_2 entrainment performance of nested-nozzle ejector. Besides, the nested-nozzle ejector is compared with the conventional, two parallelly-arranged ejectors in terms of PEMFC system power working range and anode inlet pressure fluctuation.

Chapter 5 establishes a machine learning model based on a data-driven approach to predict the ejector H_2 entrainment performance. Besides, the convex (CVX) optimization tool builds and solves a linear programming problem for optimizing ejector geometric parameters. The predicted ejector performance adopting optimized geometric parameters and machine learning model is compared with CFD simulation to evaluate the accuracy of the optimization method.

Chapter 6 focuses on the modelling of HSRS using a model-based design method in MATLAB Simulink, including the H_2 storage tank model, pressure regulator model, proportional valve model, H_2 ejector model and fuel cell stack's anode mass flow model. The HSRS model is then integrated with the existing PEMFC stack model and the air supply system model. Besides, the control strategy of HSRS is developed to test the dynamic response performance of the system model.

Chapter 7 summarizes the current work, draws conclusions, and presents the outlooks for the future developments.

Chapter 2 Related work of PEMFC Hydrogen Supply and Recirculation System

Hydrogen supply and recirculation system (HSRS) plays a vital role in supporting PEMFC system operation by providing requested and stable H_2 mass flow and pressure to the anode side. Using gas ejectors in HSRS instead of mechanical pumps presents great advantages in promoting system net output power, reducing system volume and mass, reducing noise and vibration problems, and so on. The demonstration of a PEMFC system, including the main components in the HSRS, the air supply system, and the water and heat management system, are presented in Figure 2. This research focuses on the design, modelling, and control of anode HSRS using H_2 ejectors, as shown in the dotted squares in Figure 2. Thus, related work and current studies on the HSRS are specifically summarized in this chapter.

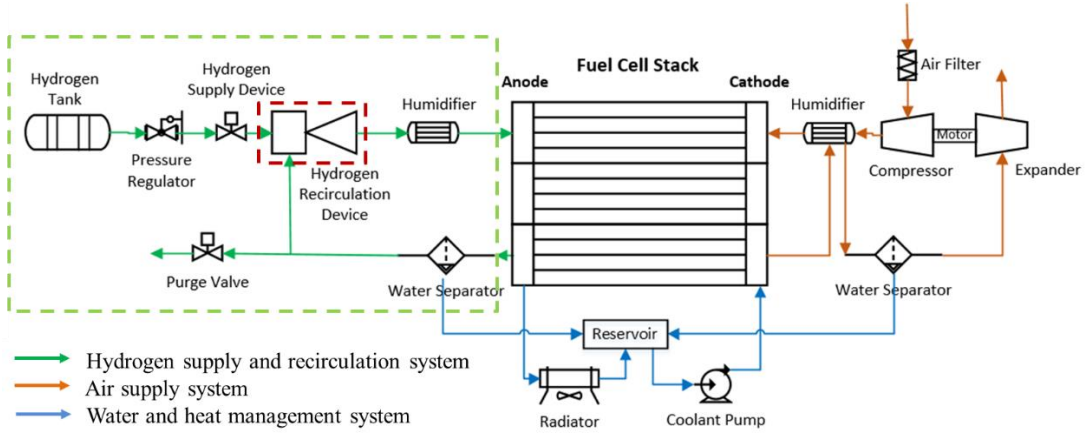

Figure 2: Schematic of a PEMFC system

A typical ejector has two inlets (for the primary and secondary flow) and one outlet (for the discharged combined flow). In addition, it includes a nozzle, a suction chamber, a constant-pressure, and constant-area mixing chamber, and a diffuser chamber. Figure 3 shows the cross-sectional view of a conventional gas ejector structure.

The primary flow of the ejector provides pure H_2 gases with high pressure through the storage tank and pressure regulator. The ejector's secondary flow consists of mixtures of unused H_2, water vapour, and N_2 from the PEMFC stack anode outlet. The high-pressure, primary flow is accelerated to the critical state when passing through the narrow nozzle throat area. It keeps increasing to a high Mach condition and creates a low-pressure area in

the suction chamber and mixing chamber. The pressure is much lower than the secondary inlet pressure, which can entrain the unconsumed H_2 gas mixture from the anode outlet into the suction chamber. The primary and secondary flow combine sufficiently in the mixing chamber and go through the diffuser chamber to recover the pressure of combined flow before entering the anode inlet of the fuel cell stack.

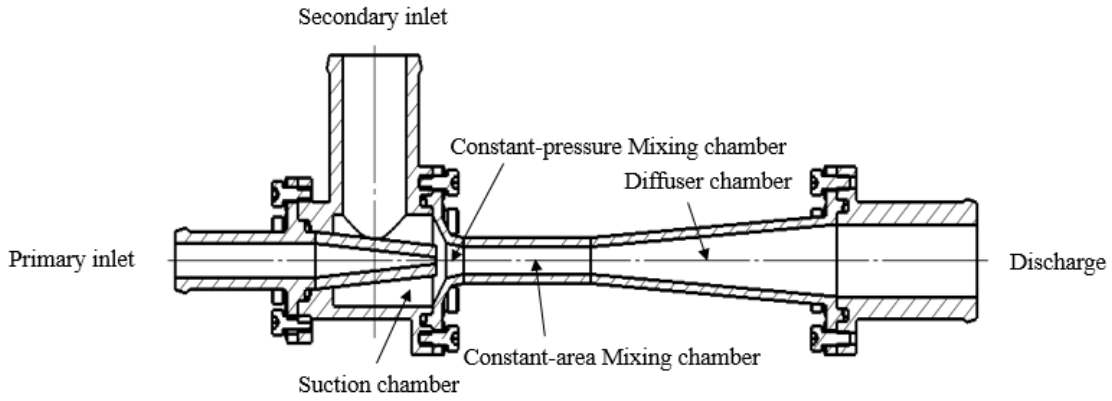

Figure 3: Cross-sectional view of a conventional single nozzle ejector

The ejector entrainment capability, denoted by the ratio of the absorbed secondary mass flow rate to the primary mass flow rate, can be greatly affected by the ejector structure and its application environment in the PEMFC system. The working fluids of both primary and secondary flows undergo drastic changes of gas pressure, velocity, and temperature through the entrainment process. To better design an ejector with high performance for PEMFC system, the ejector theoretical background, structure, operation modes, and modelling methods need to be thoroughly understood.

2.1 Research on Hydrogen Ejector Design and Modelling

Ejectors have been widely applied in industry to pump fluids from low to high pressure without consuming parasitic power. The ejector working fluids can be incompressible fluids (liquids) or compressible fluids (gases). The gas ejector is an effective substitute for the mechanical pump as the H_2 recirculation device in HSRS. During the ejector design and modelling process, the working gas inside the H_2 ejector is assumed as an ideal single-phase and isentropic flow. Besides, the internal surface of the ejector wall is assumed adiabatic hence there is no heat exchange between the ejector and the environment.

2.1.1 Ejector Theoretical Background

The theoretical background of gas ejector is the foundation to understand its working principle. The governing equations of mass, momentum, and energy as well as the ideal gas law applied in 1-D numerical models are introduced to describe the internal working fluid conditions, including the pressure, temperature, velocity, and density and so on.

The ejector nozzle is the most important part that can affect the ejector performance and other geometric dimensions. The flow pressure distribution inside a convergent-divergent nozzle is presented to illustrate the choking phenomena happened in the nozzle throat. According to operation conditions in a real PEMFC system, three operation modes of an ejector may be achieved, of which the working flows can reach the subsonic, sonic and supersonic status inside the ejector. Note that the definitions of parameters in the following equations can be found in the nomenclature table.

Ideal gas law and governing equations

The perfect gas law applied for steady 1-D compressible flow at any cross section in a finite control volume, shown in Figure 4, can be expressed as below.

$$P = \rho RT \tag{2.1}$$

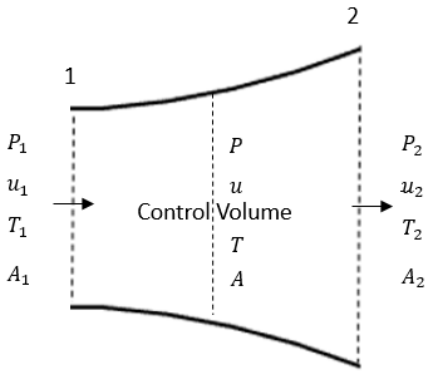

Figure 4: Finite control volume for one-dimensional compressible flow

The governing equations, including mass conservation, momentum conservation and energy conservation for steady compressible flow, are expressed as follows [35]:

$$\rho_1 u_1 A_1 = \rho_2 u_2 A_2 \tag{2.2}$$

$$P_1 A_1 + \rho_1 {u_1}^2 A_1 + \int_{A_1}^{A_2} P \, dA = P_2 A_2 + \rho_2 {u_2}^2 A_2 \tag{2.3}$$

$$h_1 + \frac{{u_1}^2}{2} = h_2 + \frac{{u_2}^2}{2} \tag{2.4}$$

where ρ, u, A, P, and h are gas density, velocity, section area, gas pressure and enthalpy, respectively. The subscript indicates the section area 1 and 2 in the controlled volume.

Isentropic flow

For an isentropic ideal gas, the stagnant pressure, temperature and density [35] are given as follows:

$$\frac{dP}{P} = \gamma \frac{d\rho}{\rho} \tag{2.5}$$

$$\frac{P_0}{P} = \left(1 + \frac{\gamma - 1}{2} M^2\right)^{r/(r-1)} \tag{2.6}$$

$$\frac{T_0}{T} = 1 + \frac{\gamma - 1}{2} M^2 \tag{2.7}$$

$$\frac{\rho_0}{\rho} = \left(1 + \frac{\gamma - 1}{2} M^2\right)^{1/(r-1)} \tag{2.8}$$

where P_0, T_0, and ρ_0 represent the stagnation properties of the isentropic flow. M is a dimensionless velocity parameter for compressible flow, which describes the ratio of current flow velocity u to local sonic velocity. Usually, $M \geq 0.3$ is for compressible flow.

$$M = \frac{u}{\sqrt{\gamma RT}} \tag{2.9}$$

The relationship between flow area A and velocity u is given below:

$$\frac{dA}{A} = (M^2 - 1)\frac{du}{u} \tag{2.10}$$

The isentropic flow properties in the convergent and divergent ducts can be analyzed using above equations. For subsonic flow ($0.3 \leq M < 1$), the flow velocity increases while flow pressure and density decreases as area A reduces in the convergent duct [35]. On the contrary, when area A increases in the divergent duct, the flow velocity drops, and the flow pressure and density go up. For supersonic flow ($M > 1$), an increase or decrease of area A leads to an opposite change in flow properties compared to those of subsonic flow. The variations on flow properties in different scenarios are summarized in Figure 5.

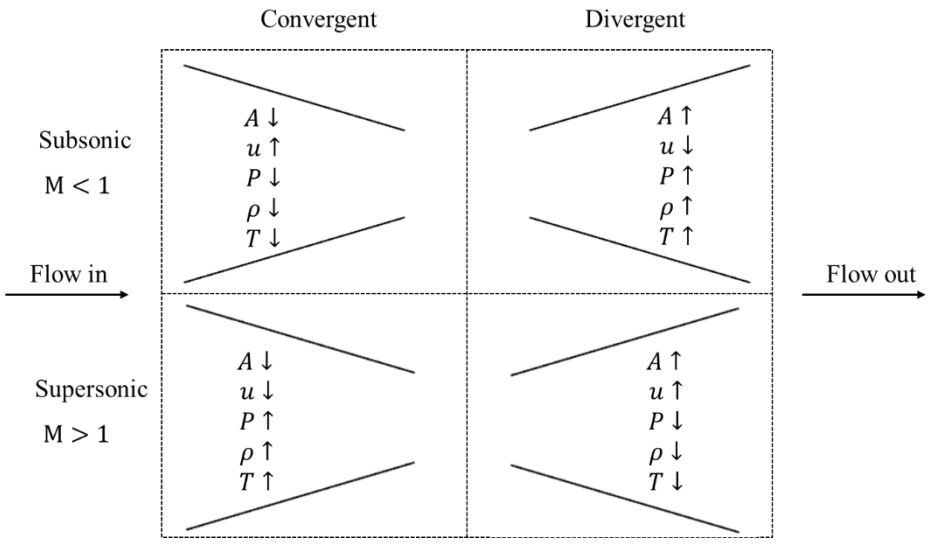

Figure 5: Isentropic compressible flow properties in convergent and divergent ducts

Convergent-divergent (CD) nozzle working principles

A CD nozzle is applied to illustrate the flow-choking phenomena in the nozzle throat. The working conditions of a CD nozzle are determined by inlet pressure P_0 and back pressure P_b. Generally, the maximum mass flow rate of a CD nozzle is restricted by the nozzle throat, which is the narrowest part along its flow direction. At a given inlet pressure P_0, the mass flow rate and velocity at the throat are increased when the back pressure P_b decreases until it reaches critical status. The static pressure distribution of isentropic compressible flow inside the nozzle along the length direction is presented in Figure 6 [35]. The flow is regarded as choked when the mass flow rate at the nozzle throat reaches its maximal value and remains unchangeable no matter how to reduce the back pressure P_b with constant inlet pressure P_0.

- When $P_0 \cong P \cong P_b$, negligible amount of flow goes through the nozzle since there is no enough driving force resulted from the pressure potential energy between the inlet pressure and outlet pressure. The flow on curve *I* is subsonic and can be regarded as incompressible ($M \leq 0.3$).
- As the back pressure P_b decreases, the flow rate gradually increases and the flow on curve *II* remains subsonic through the whole nozzle.
- If the back pressure P_b is low enough, the compressible flow on curve *III* reaches a critical condition at the nozzle throat with maximal velocity ($M = 1$), minimal

pressure P_* and maximal mass flow rate $\dot{m}_*$. The flow is regarded as choked. The flow velocity decreases from sonic at the nozzle throat to subsonic while the pressure recovers through the divergent section.

- When the back pressure P_b continues decreasing, the flow is still choked at the nozzle throat with a maximum mass flow rate $\dot{m}_*$ and local sonic velocity. However, the flow turns to be supersonic in the divergent nozzle area, as shown on curve *IV*.

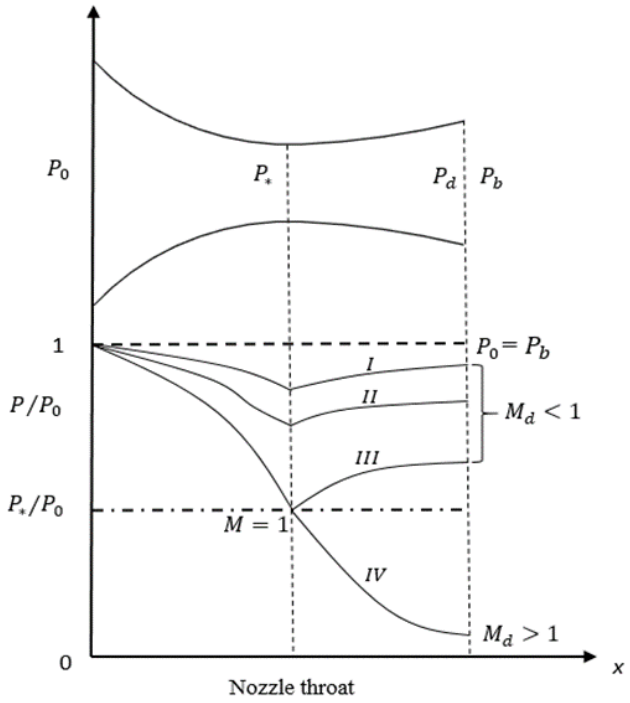

Figure 6: Pressure and velocity variation of isentropic flow in a CD nozzle

For choked flow ($M = 1$), the static properties of working flow at the nozzle throat P_*, T_*, ρ_*, u_* and $\dot{m}_*$ are presented as bellows.

$$\frac{P_0}{P_*} = \left(\frac{\gamma + 1}{2}\right)^{r/(r-1)} \tag{2.11}$$

$$\frac{T_0}{T_*} = \frac{\gamma + 1}{2} \tag{2.12}$$

$$\frac{\rho_0}{\rho_*} = \left(\frac{\gamma + 1}{2}\right)^{1/(r-1)} \tag{2.13}$$

$$u_* = \sqrt{\gamma R T_*} \tag{2.14}$$

$$\dot{m}_* = CA_* P_0 \sqrt{\frac{\gamma}{RT_0}\left(\frac{2}{\gamma+1}\right)^{(r+1)/(r-1)}} \quad (2.15)$$

2.1.2 Structure and Operation Modes of Ejector

Ejector Structure

The gas ejector can be classified into different categories based on the shape, position, number, and diameter variability of the ejector nozzle, which are summarized as follows:

- **Based on the structure of the ejector nozzle**

Convergent nozzle ejector: The working fluid of this ejector can be both incompressible liquid and compressible gas. The subsonic fluid at ejector primary inlet can accelerates at most to sonic as a chocked flow at the nozzle exit.

Convergent-divergent nozzle ejector: Both compressible and incompressible fluid can be used in the ejector with a convergent-divergent nozzle. The working flow at the nozzle exit can be subsonic, sonic, and supersonic. However, it causes considerable thermodynamic complexity in the mixing and diffuser chambers when the flow at the nozzle exit reaches supersonic [32].

The ejector applied in HSRS should consider its operation environment and boundary conditions. Due to the low temperature of primary hydrogen flow inside the nozzle and the high temperature of the secondary inlet mixture around the nozzle, the liquid water resulting from the water vapour condensation may turn into ice in the convergent-divergent nozzle throat, which narrows the nozzle throat area and thus reduces the ejector H_2 entrainment performance. Consequently, the convergent nozzle instead of the convergent-divergent nozzle is applied for the H_2 ejector in HSRS of the PEMFC system.

- **Based on the position of the ejector nozzle**

Constant-area mixing ejector [28, 31]: The nozzle outlet is located within the constant-area mixing chamber where the entrained flow from the secondary inlet is combined with the primary flow.

Constant-pressure mixing ejector: The nozzle outlet is located in front of the constant-area mixing chamber. This ejector has been widely used due to its better entrainment performance compared to the constant-area mixing ejector. According to the constant-

pressure mixing theory developed by Keenan et al. [28], the primary and secondary flows are mixed in the constant-pressure mixing chamber with a constant and uniform pressure and the ejector can operate against a high back pressure [36].

- **Based on the number of the ejector nozzle**

Single nozzle ejector: The ejector consists of only one nozzle. Therefore, it can only provide effective entrainment capability in a limited working range.

Multi-nozzle ejector: The multi-nozzle ejector is beneficial to achieve a wider fuel cell power operating range. Xue et al. [23] presented a ejector with four small symmetrical convergent nozzles, through which the accumulated primary mass flow rate is equal to that of a conventional single nozzle ejector. The ejector operating with two symmetrical nozzles has the best entrainment performance. Han et al. [24] designed a ejector with one central nozzle for low output power range and two symmetrical nozzles for high output power range. Du et al. [25] introduced a coaxial-nozzle ejector of which one nozzle with small diameter is located inside another nozzle with big diameter and both nozzles' outlets are in the same vertical plane. All these multi-nozzle ejectors have complex structures and thus increase the difficulties in manufacturing and operations.

- **Based on the diameter variability of the ejector nozzle**

Fixed nozzle diameter ejector: It has been widely applied in the industry due to its simpler structure and easy control. The ejector can provide an effective entrainment ratio in its designed range. However, the performance decreases rapidly when the operation conditions fall into the off-design area.

Douglas et al. [20] designed a variable flow ejector by adding a needle connected to a stepper motor before the nozzle. The needle protrudes through the nozzle along the central axis to adjust the primary inlet flow rate by changing the nozzle opening size. Sugawara et al. [21] presented a similar variable flow-rate ejector with the nozzle inserted by a needle. The difference between these two ejectors is the needle is driven by two diaphragms instead of a stepper motor. These electronic controlled ejectors have a wider operating rage, however, with more complex manufacturing process and control strategy.

Operation modes of a gas ejector

A gas ejector for a PEMFC system usually adopts a convergent nozzle instead of a CD nozzle to prevent water vapour condensation in the nozzle throat. Due to the ejector structure with two inlets and one outlet, the operation modes can be divided into three regions depending on the back pressure P_d [31] as shown in Figure 7.

- Double-choking mode (critical mode): When P_d is less than the critical pressure P_1, the primary H_2 flow and secondary mixture flow are choked at the convergent nozzle exit, and in the constant-area mixing chamber, respectively. In this mode, the ejector has maximal and constant H_2 entrainment ratio ω_{H_2}.
- Single-choking mode (subcritical mode): When P_d is between critical pressure P_1 and P_2, only primary H_2 flow is chocked. The ω_{H_2} decreases as P_d increases.
- Backflow mode: When P_d is higher than P_2, no flow choking phenomena happens for both primary and secondary flow inside the ejector, which means there is no flow entrained into the ejector from the secondary inlet. Thus, the ejector falls into a failure mode.

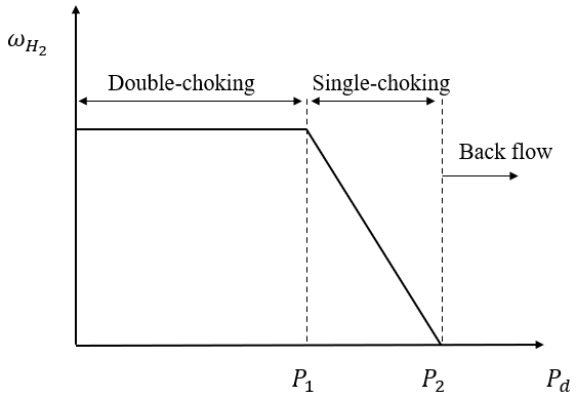

Figure 7: Ejector operation modes at fixed primary inlet pressure and variable discharge pressure

2.1.3 Ejector Analytic Models

Ejector analytic models mainly include 1D empirical models and 3D numerical models based on CFD simulations. As mentioned in Chapter 1, 1D empirical models are mostly derived from the constant-pressure mixing theory introduced by Kennan et al. [28]. The modified constant-pressure mixing model with critical operation modes presented by Huang et al. [31] and shock circle model with an exponential expression for velocity distribution of secondary flow proposed by Zhu et al. [33] have been widely applied in

ejector design. In these models, the conservation equations of mass, momentum and energy with isentropic flow properties are adopted to analyze the flow fields and ejector entrainment performance. The working flow inside the ejector is regarded as an ideal gas, and there is no heat exchange between the ejector and environment. Besides, several assumptions on the pressure and velocity of working flow and flow properties are also applied to simplify the model derivation. Figure 8 shows a schematic view of the mixing process of the primary and secondary flow.

For the aforementioned three 1D models, (i) the constant pressure mixing model, (ii) the constant pressure mixing model with critical modes, and (iii) the shock circle model, the common assumptions of these three models include:

- The operational flows at ejector inlets and outlet are assumed at stagnation conditions; hence their kinetic energies are neglected.
- The pressure of secondary flow distributes uniformly in the suction chamber and equals secondary inlet pressure.
- The pressure of primary and secondary flow is uniformly distributed along the vertical direction inside the ejector.
- The pressure of the combined flow is uniform and constant in the mixing process.

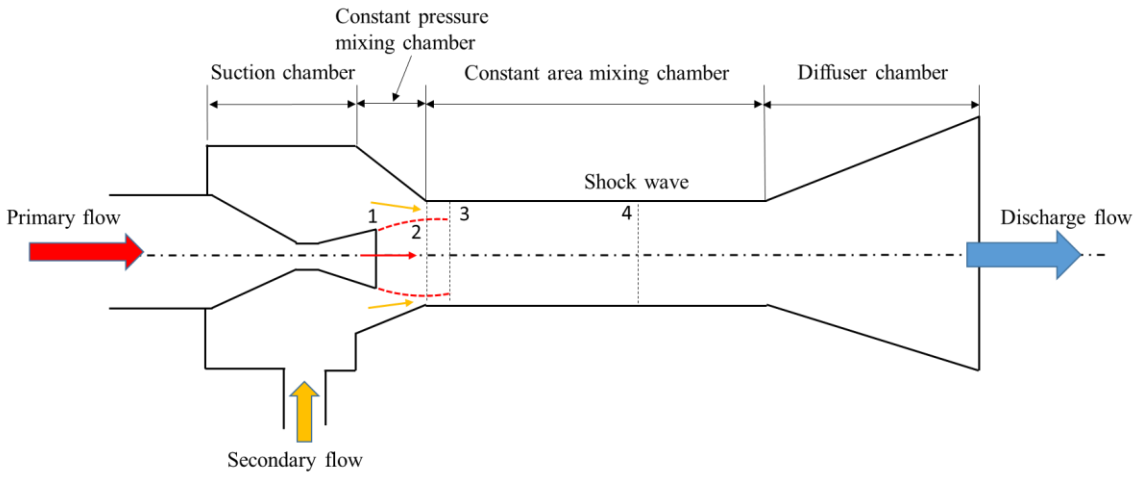

Figure 8: Schematic diagram of ejector flow operating conditions

The different assumptions are summarized as follows:

- **Choking modes**

The constant pressure mixing model only considered primary flow is choked at nozzle throat, while other two models considered the secondary flow is also choked at certain

pressure boundary conditions of ejector inlets and outlet. In the shock circle model, a series of shocks happen in the suction chamber and mixing chamber due to insufficient expansion of primary flow, which accelerate the secondary flow to a choking condition [33].

- **The mixing process of primary and secondary flow**

For the constant pressure mixing model, the mixing process of two flows happens in the constant pressure mixing chamber, which specifically begins at nozzle exit (section 1) and ends at the inlet of constant area mixing chamber (section 2) as shown in Figure 8. Besides, the mixing loss is not considered.

For the constant pressure mixing model with critical modes, the mixing process occurs inside the constant area mixing chamber from section 3 to section 4 (shock wave section). The mixing and frictional losses are considered by applying several coefficients in the governing equations which should be determined through experiments.

For the shock circle model, the mixing process starts at the inlet of constant area mixing chamber (section 2) and ends before entering the diffuser chamber. The energy loss equation is induced to consider the energy loss of primary flow and secondary flow from the inlets to section 2.

- **Flow properties**

The specific heat at constant volume is not affected by the flow temperature in constant pressure mixing model, while it varies according to flow temperatures in the shock circle model.

The secondary flow velocity near the ejector inner walls is zero due to the viscous properties of compressible flow. Hence, the flow velocity is actually non-uniformly distributed inside the ejector. Compared to the uniformly distributed flow velocity of other two models, the shock circle model proposed a 2D exponential expression for the secondary velocity distribution near the ejector inner walls, which can be seen in Figure 9. The x-axis indicates the vertical distance from the centre of section 2 to any point r. The y-axis indicates the flow velocity variations along the vertical direction at any point r.

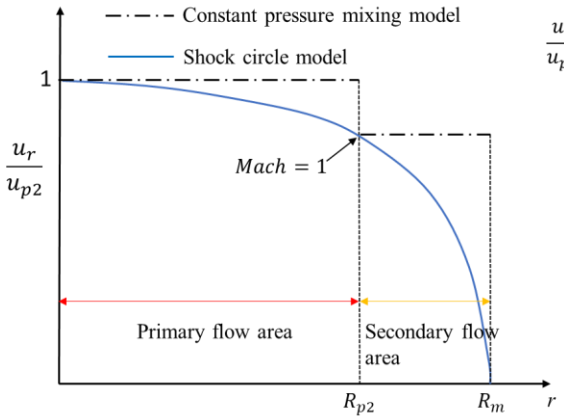

$$\frac{u_r}{u_{p2}} = (1 - \frac{r}{R_m})^{\ln(\sqrt{T_{s2}/T_{p2}}/M_{p2})/\ln(1-R_{p2}/R_m)}$$

u_r: velocity of flow at section 2 along vertical direction;
u_{p2}: priamry flow velocity along vertical direction of section 2;
R_m: constant area mixing chamber radius;
R_{p2}: radius of the primary flow area (the area between two red dashed line at section 2 shown in Figure 8);
T_{s2}: secondary flow temperature at section 2;
T_{p2}: primary flow temperature at section 2;
M_{p2}: primary flow Mach number at section 2;

Figure 9: Velocity distribution of primary and secondary flows along a vertical direction in section 2

The assumptions and simplifications made by the above 1D analytical models have restricted their applications and reduced the accuracies on the ejector entrainment performance. In recent years, the numerical modelling methods based on CFD simulations of ejector working flow have been widely adopted [37-39] using advanced commercial software. The flow computational domain can be divided into a large number of tiny cells through meshing technique, and each cell's properties are calculated by certain turbulence models. Hence, the pressure, velocity, and temperature field of internal working flow can be provided in detail with more accurate results. The detailed CFD numerical modelling method are introduced in Chapter 3.

2.2 HSRS Design and Operation

The purpose of HSRS is to supply required H_2 mass flow and pressure to the fuel cell stack according to PEMFC system operation conditions. Meanwhile, the pressure difference between the stack anode and cathode should be controlled in a certain range to prevent damaging the fuel cell membrane. Usually, HSRS includes the following auxiliary components: the H_2 storage tank, pressure regulator, cut-off valve, H_2 supply devices, H_2 recirculation devices, a water separator, a purge valve, temperature sensors, pressure sensors and so on.

2.2.1 HSRS Operation

The compressed H_2 from the high-pressurized storage tank in FCEVs can provide pressure of up to 700 bara. The pressure regulator reduces the high pressure to a relatively low pressure, usually no more than 16 bara, for system safety considerations. The H_2 supply devices, such as a proportional valve or injector, adjust the H_2 mass flow rate required by the stack according to different stack operation conditions. Compared to the H_2 injector, the proportional valve can operate at a higher inlet pressure and sustain a wide range of inlet/outlet pressure differences, thus, providing a higher H_2 mass flow rate is more suitable for the PEMFC stack with high power output.

A H_2 recirculation device, usually a pump or ejector, is required between the H_2 supply device and the stack anode inlet to recirculate unconsumed H_2 gas mixture from the stack anode outlet. The H_2 ejector takes advantage of the high-pressure potential energy between the pressure regulator (maximum 16 bara) and the anode inlet (1.5 to 2.7 bara, depending on the operation conditions) to perform the circulation task without consuming parasitic power. The excessive H_2 pumped to the stack anode can discharge the accumulated liquid water and impurities in the anode flow channel, which is beneficial to maintain the ideal temperature, humidity, and quality of the H_2 fuel required by the stack. Hence, the mixture leaving the anode carries water vapour, liquid water, unconsumed H_2, and N_2 crossed over the membrane from the cathode.

The water separator is applied to remove the liquid water from the mixture and transport the liquid water to humidify the H_2 and air reactant when needed. After long operations, water flooding and many gaseous impurities decrease cell voltage and, thus, result in a lower PEMFC system efficiency. A purge process is applied to purify the H_2 reactant gas in the anode flow channel and the impurities are discharged from HSRS through the purge valve to address the issue.

2.2.2 Architectures of HSRS

The design of HSRS using ejectors and/or mechanical pumps varies according to its applications and operation requirements in different PEMFC stacks. Therefore, the PEMFC stack specification plays an important role in choosing and designing the other auxiliary components of HSRS. According to the recirculation methods, the HSRS

structure can be categorized into four major groups: single recirculation pump, single ejector, a combination of one recirculation pump and ejector, and two parallel ejectors.

(1) HSRS Using One Single Recirculation Pump

The key characteristic of this HSRS structure is that there is only one H_2 recirculation pump to recycle the unconsumed H_2 from the stack anode outlet. Although it has a simple structure and is easy to control, the mechanical pump needs to satisfy a wide operating range of H_2 mass flow rate, which can be a challenge for large PEMFC stacks. Figure 10 shows the HSRS structure of the Toyota Mirai. Since the maximum H_2 mass flow provided by one injector is low, three H_2 injectors are used to supply the required H_2 directly to the PEMFC stack. The mechanical pump benefits the fast and dynamic response of PEMFC system power change. However, the pump consumes electric power and brings issues such as vibration, noise, and potential poisoning to the fuel cell membrane if oil-based lubrication is used.

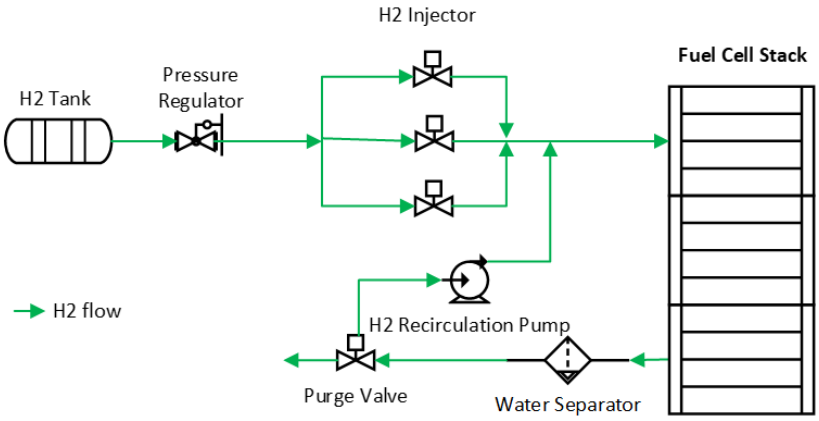

Figure 10: HSRS with single H_2 recirculation pump

(2) HSRS Using One Single Hydrogen Ejector

A gas ejector can be used to substitute the pump as H_2 recirculation device. Unlike the pump, the primary H_2 flow provided by supply devices also goes into the ejector to mix with the unused H_2 before entering the fuel cell stack. The ejector is a pure mechanical component without electric units. Thus, there is no power consumption, vibration, or noise issues. The ejector performance depends on the geometric size design and PEMFC operation conditions. Only a limited operation range can be effectively provided for the

ejector with fixed dimensions. Thus, a minor deviation from design conditions could lead to a decrease or even a failure of the performance. Sometimes, the bypass can be adopted parallel to the ejector to enlarge the anode mass flow range and for purge purposes, as shown in Figure 11.

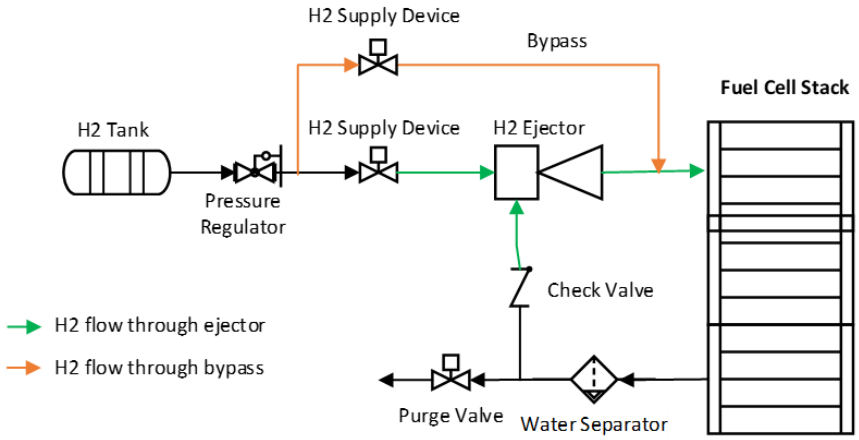

Figure 11: HSRS with a single H_2 ejector and one bypass

(3) HSRS Using One Recirculation Pump and One Ejector

The HSRS adopting a combination of one mechanical pump and one ejector is a promising solution to provide an extended wide range of operation for the PEMFC system. Since the pump costs higher than the ejector and is more accessible by providing a low mass flow rate, the pump takes responsibility for the low load operating conditions. In contrast, the ejector operates at high power conditions. Usually, a three-way valve or diverter is applied to separate the pump and ejector's flow channels. Figure 12 shows the HSRS structure using a pump and an ejector. The primary H_2 flow channel can also act as a bypass to support purse purposes when there is accumulated water and impurities in anode flow channels. This structure is more flexible and effective for a wide range of PEMFC operations. However, it also increases the system complexity, cost, and control difficulty.

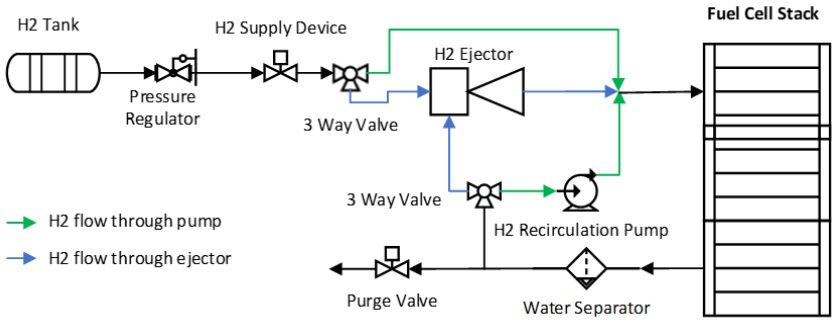

Figure 12: HSRS with a combination of H_2 pump and ejector

(4) HSRS Using Multiple Ejectors

Using two or more paralleled H_2 ejectors in HSRS can effectively enlarge the working range of the PEMFC system, providing that each ejector is optimally designed and controlled for a specific operational range. The HSRS using dual ejectors and a bypass is shown in Figure 13. The two ejectors can work individually or simultaneously based on the various geometric size design and control strategies. Ejector A takes charge of the low load conditions, while ejector B or both ejectors working together can be responsible for high load conditions. When ejectors work independently, they can share one H_2 supply device. Alternatively, each ejector can have an independent H_2 supply device since generally two ejectors have different geometric parameters to cover a different amount of H_2 mass flow. This HSRS structure is superior to the HSRS using a combination of a pump and an ejector in terms of the system cost and control complexity. However, the multi-ejector HSRS may cause pressure fluctuation at the anode inlet when shifting the gas pathway among different ejectors, which may damage the membrane and induce mechanical deterioration in the performance.

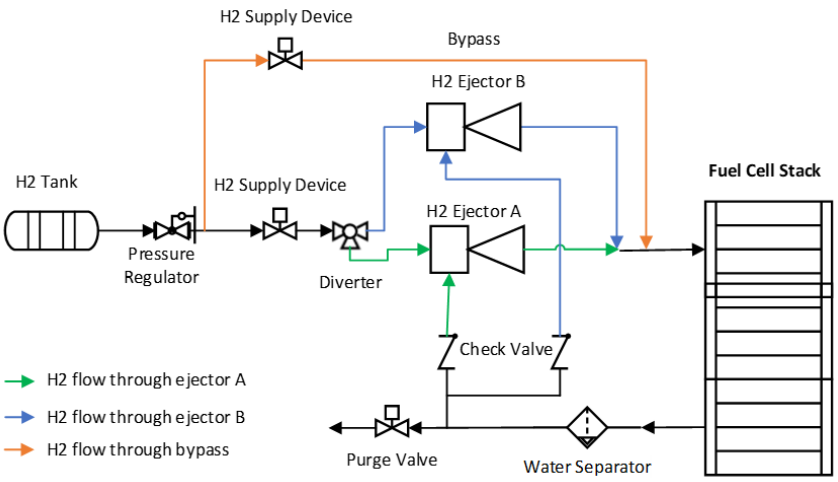

Figure 13: HSRS with dual H_2 ejectors and a bypass

2.3 Summary

In this chapter, the ejector theoretical background including the ideal gas law, governing equations of the compressible gas and isentropic flow properties on a convergent-divergent nozzle are introduced. Besides, three operation modes of a gas ejector using a convergent nozzle including double-choking, single-choking and back flow modes are presented.

As a substitution component for a mechanical pump in HSRS, the ejector structure and modelling methods are summarized and compared to achieve the best design solution. Moreover, various HSRS architectures adopting different combinations of ejector and pump are compared.

Chapter 3 CFD Simulation and Performance Analysis of an Ejector

The H_2 entrainment capability of an ejector-based HSRS depends on the ejector's geometric parameters and the PEMFC system's operating conditions. The optimal design of the H_2 gas ejector relies heavily on the flow properties of the gas, including pressure, temperature and velocity inside the ejector. The best approach to acquire the flow fields is to carry out 3D numerical simulations using computational fluid dynamic (CFD) simulations.

This research adopts a large PEMFC stack with a maximum of 150 kW to demonstrate the ejector design process. In this chapter, the numerical modelling and CFD simulation method is introduced to investigate the influences of key ejector geometric parameters. Besides, the variations of ejector entrainment performance under different PEMFC system operation conditions are analyzed.

3.1 Numerical Modelling and CFD Simulation

CFD simulations are conducted using ANSYS Fluent during the design optimization of the ejector. The 3D axisymmetric ejector fluid domain is generated in Simens NX12 and imported into ANSYS Fluent environment for domain meshing and simulations. Several assumptions are made before simulations. First, the ejector's working fluids, including the primary stream of pure H_2 gas and the secondary stream of surplus H_2 from the stack with a small amount of by-passed nitrogen (N_2) and water vapour are considered single-phase gas and assumed to be the ideal compressible gas in a steady-state turbulent condition. Secondly, the internal surface of the ejector wall is viewed as adiabatic. Hence there is no heat exchange between the ejector and the environment. Thirdly, the gravity of the working fluids is neglected. Finally, the secondary mixture flow from the anode outlet is assumed to consist of H_2, water vapour and N_2.

Generally, three models, including the standard k-ε model, the RNG k-ε model, and the SST k-ω model, have been adopted during the previous studies [17, 40, 41]. Compared to the other two models, the SST k-ω model has shown better accuracy with the experimental results on a wide operation demonstrated by several researchers [37, 42], thus, adopted to here to acquire the pressure, veloctiy, temperature, and sepcies mass fraction field of the internal flow in the ejector.

3.1.1 PEMFC Anode Specifications

The operation conditions of the PEMFC stack, including pressure, temperature, mass flow rate, relative humidity, and species of the H_2 flow at anode inlet and outlet play a vital role in the ejector design and geometric optimization. This research adopts a large PEMFC stack to present the ejector optimization process. The PEMFC stack operation current is 35 to 600 A, corresponding to a total stack voltage ranging from 328 to 248 V, providing around 13 kW of idle power and 150 kW of maximum power. The theoretical reacted H_2 mass flow rate $\dot{m}_p$ and H_2 stoichiometric ratio SR_{H_2} are plotted in Figure 14. Generally, the stack requires high SR_{H_2} at low power range to maintain enough flow pressure and remove the liquid water in anode flow channels. For this PEMFC stack, the SR_{H_2} is between 1.5 and 2.5. The anode inlet pressure $P_{an,in}$ is between 1.5 bara and 2.6 bara, and the stack anode pressure drop is less than 10 kPa with slight variations on different power outputs. The anode outlet mixture temperature $T_{an,out}$ is between 330 K and 353 K with 100% relative humidity.

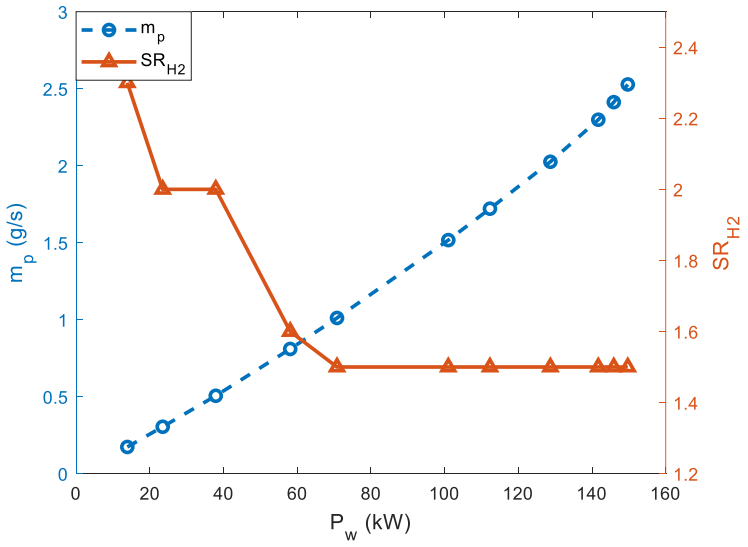

(a)

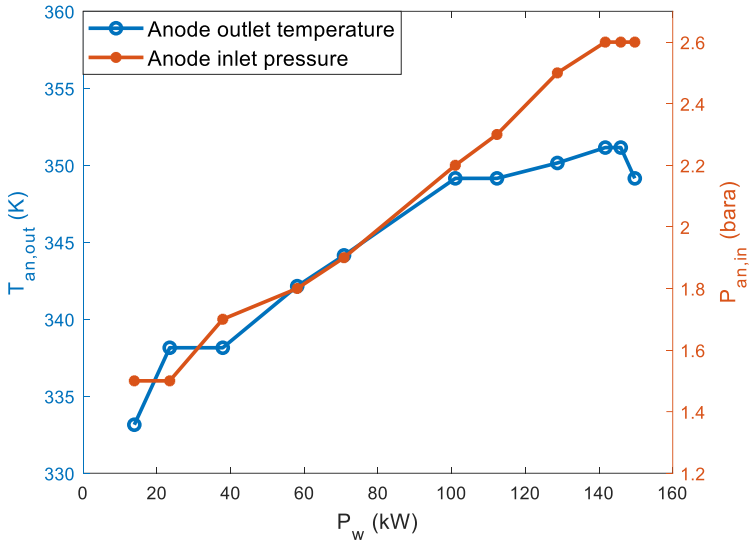

(b)

Figure 14: 150 kW PEMFC stack operation conditions: (a) the primary mass flow rate $\dot{m}_p$ and H_2 stoichiometric ratio SR_{H_2} and, (b) the anode inlet pressure $P_{an,in}$ and outlet temperature $T_{an,out}$

3.1.2 Governing Equations

The mass, momentum, energy and species transport conservation equations of the working flow inside the ejector are given as follows, respectively [24, 38]:

Mass conservation:

$$\nabla(\rho\vec{u}) = 0 \tag{3.1}$$

Momentum conservation:

$$\nabla(\rho u_i\vec{u}) = -\frac{\partial P}{\partial x_i} + \left(\frac{\partial \tau_{ii}}{\partial x_i} + \frac{\partial \tau_{ji}}{\partial x_j} + \frac{\partial \tau_{ki}}{\partial x_k}\right) + \rho f_i \tag{3.2}$$

Energy conservation:

$$\nabla[\vec{u}(\rho E + P)] = \nabla\left[k_{eff}\nabla T - \sum_c h_c J_c + (\tau\vec{u})\right] \tag{3.3}$$

Species transport equation:

$$\nabla(\rho\vec{u}Y_c) = -\nabla\vec{J_c} \tag{3.4}$$

where $\vec{u}$ is the velocity vector, ρ is the hydrogen density, P is the pressure; i, j, and k are the x, y, and z directions, respectively, τ is the stress tensor, E is the total energy, f is the

mass force and k_{eff} is the thermal conductivity, h_c is the enthalpy of species, J_c is the diffusive flux of species, and Y_c is the mass fraction.

The H_2 entrainment ratio ω_{H_2} is adopted to evaluate the ejector performance. Note that ω_{H_2} here only considers the pure H_2 mass fraction among the entrained secondary mixture from the anode outlet, which also consists of water vapour and N_2. λ_{H_2} is introduced to count the total amount of H_2 supplied by the ejector. If λ_{H_2} is larger than the required anode H_2 stoichiometric ratio SR_{H_2} at each operating point, the ejector can be recognized as qualified.

$$\omega_{H_2} = \frac{\dot{m}_s}{\dot{m}_p} y_{H_2} \tag{3.5}$$

$$\lambda_{H_2} = \omega_{H_2} + 1 \geq SR_{H_2} \tag{3.6}$$

where $\dot{m}_p$ and $\dot{m}_s$ are the mass flow rate of primary and secondary flow, respectively (kg/s), and y_{H_2} is the H_2 mass fraction in the entrained secondary flow.

The stack anode's theoretical react H_2 mass flow rate $\dot{m}_p$ is calculated as:

$$\dot{m}_p = \frac{N_{cell} I}{2F} M_{H_2} \tag{3.7}$$

where N_{cell} is the cell number of the fuel cell stack, I is the fuel cell stack current (A), F is the Faraday constant 96,485 (C/mol), and M_{H_2} is the H_2 molar weight (kg/mol).

For the ejector with a convergent nozzle, the relationship between the maximum mass flow rate and the nozzle's throat diameter D_n at choking mode can be determined using the following equation:

$$\dot{m}_p = C_d \frac{\pi D_n^2 P_p}{4\sqrt{T_P}} \sqrt{\frac{\gamma}{R}\left(\frac{2}{\gamma+1}\right)^{\frac{\gamma+1}{\gamma-1}}} \tag{3.8}$$

where P_p and T_p are primary inlet pressure (bara) and temperature (K), respectively. C_d is the nozzle discharge coefficient (0.95-0.98).

The secondary mixture consists of H_2, N_2, and water vapour. The water saturation pressure is determined as equation 3.9. Thus the H_2 entrainment ratio ω_{H_2} can be expressed as equation 3.10.

$$P_{sat}(T) = (-2846.4 + 411.24T - 10.554T^2 + 0.166T^3)/100000 \tag{3.9}$$

$$\omega_{H_2} = \frac{M_{H_2}(P_{an,out} - \phi_{an,out}P_{sat} - P_{N_2})}{M_{H_2}(P_{an,out} - \phi_{an,out}P_{sat} - P_{N_2}) + \phi_{an,out}M_{H_2O}P_{sat} + M_{N_2}P_{N_2}} \quad (3.10)$$

where P_{sat} is saturated water pressure (bara), P_{N_2}, P_{H_2} are partial pressure of N_2 and H_2 in the secondary mixture respectively (bara), $P_{an,out}$ is the anode outlet pressure (bara), T here is the anode outlet mixture temperature (℃). M_{H_2}, M_{H_2O}, M_{N_2} are the H_2, water vapour and N_2 molar weight (kg/mol) respectively. $\phi_{an,out}$ is the relative humidity of the secondary stream mixture.

3.1.3 Boundary conditions

Boundary conditions of the CFD simulations are set based on the PEMFC stack realistic specifications shown in Figure 14. The primary H_2 temperature T_p is assumed constant at 293.15 K, and the primary inlet is set as a mass flow rate inlet. The ejector's secondary inlet is set as pressure $P_{an,out}$, species mass fraction of the mixture and temperature $T_{an,out}$. The ejector outlet is set as a pressure outlet with pressure $P_{an,in}$. The boundary condition varies according to the different operating conditions of the fuel cell stack.

3.2 Influence of Ejector Geometric Parameters

The H_2 entrainment performance of an ejector can vary largely depending on its geometric parameters. The most crucial ejector geometries include the nozzle throat diameter (D_n), constant area mixing chamber diameter (D_m) and length (L_m), and the nozzle exit position (NXP) relative to the constant pressure mixing chamber, which is carefully investigated in this chapter using CFD simulations. Other parameters, such as the diffuser chamber length L_d and its divergent angle α_d, relatively have a slight influence on the ejector performance [14].

The simulation results of the ejector's pressure, velocity, temperature, and H_2 gas mass fraction in the symmetric plane at the PEMFC operation condition (140 kW) are presented in Figure 15. It can be seen that the primary H_2 flow is accelerated to sonic flow at the convergent nozzle exit and keeps accelerating to a supersonic flow in the suction chamber and mixing chamber (Figure 15(b)). The high Mach flow creates a low-pressure area much lower than the secondary inlet pressure (Figure 15(a)). Hence, the secondary mixture is

absorbed into the suction chamber and combined with the primary flow in the mixing chamber. Then the combined flow goes through the diffuser chamber to recover its pressure.

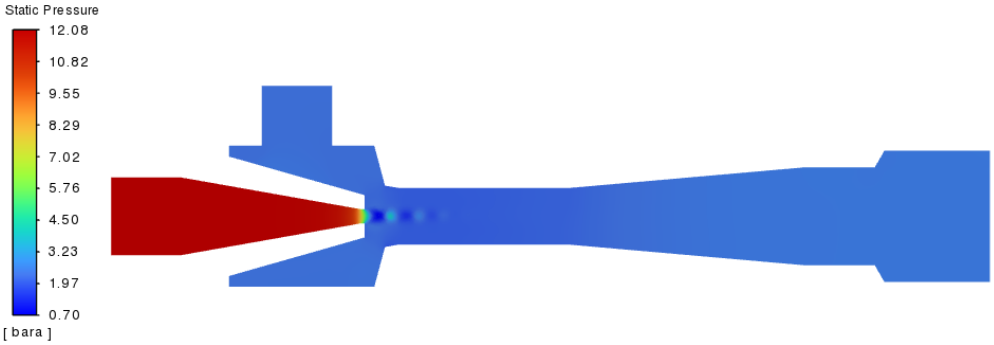

(a)

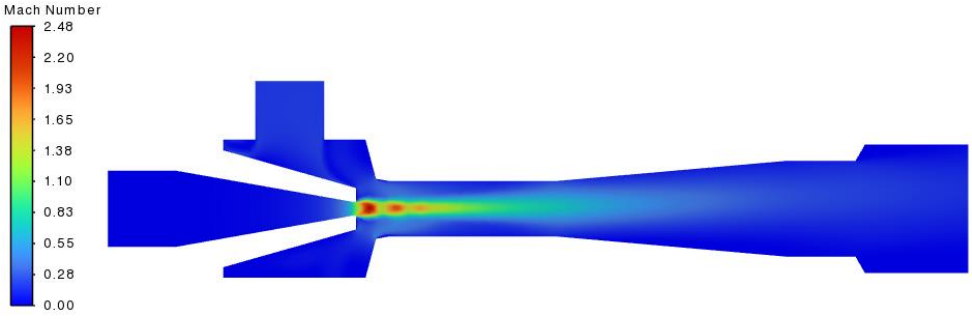

(b)

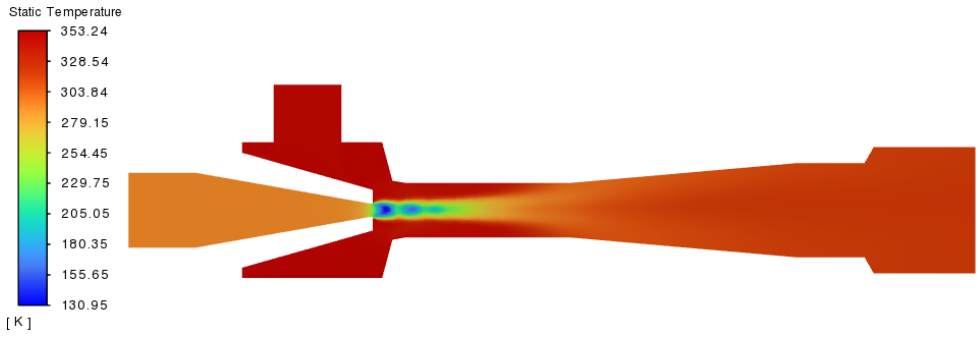

(c)

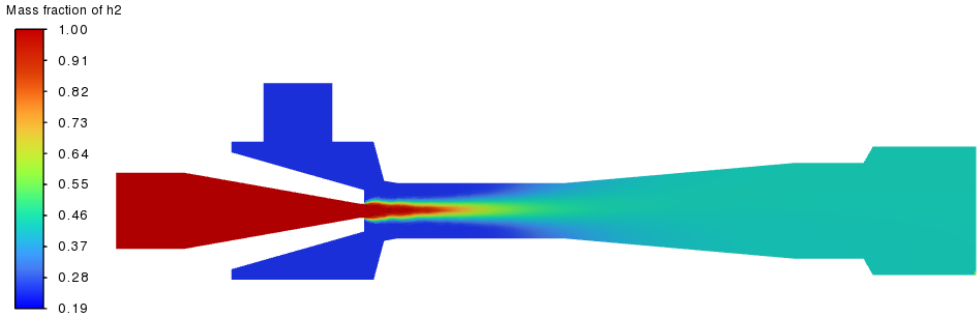

(d)

Figure 15: CFD simulation results: (a) pressure; (b) velocity; (c) temperature; (d) H2 mass fraction

3.2.1 Effect of Nozzle Throat Diameter D_n

The ejector nozzle diameter, D_n, is the most critical parameter determining the ejector's primary inlet pressure, affecting the velocity and pressure field of direct flow at the nozzle throat and in the suction chamber. The effects of D_n value on the ejector's entrainment performance has been shown in Figure 16. With fixed $D_m = 8\ mm, L_m = 40\ mm\ and\ NXP = 3\ mm$, the λ_{H_2} increases as D_n decreases from 2.5 mm to 1.0 mm. The smaller the throat diameter D_n is, the wider the ejector effective operating range can be achieved.

A comprehensive comparison of the effects of D_n on the ejector pressure variations are presented in Figure 17. At a given mass flow rate, a smaller D_n results in a higher primary inlet pressure P_p, which in turn, generates a higher pressure at the nozzle throat P_n and a larger pressure difference dP between the nozzle throat and the suction chamber. A higher dP creates an area from the suction chamber to the mixing chamber inlet where the primary flow pressure is much lower than the secondary inlet pressure P_s, and thus acquires a better entrainment performance λ_{H_2}. For example, when $\dot{m}_p$ is 0.71 g/s, dP is increased dramatically from almost zero to 6.2 bara if D_n is decreased from 2.5 to 1.0 mm. which increases the λ_{H_2} dramatically from 1.6 to 2.2, as shown in Figure 17.

The ejector nozzle throat diameter D_n is restricted by the maximum primary inlet pressure provided by the pressure-reducing valve, which is usually around 16 bara due to system safety considerations. In this case, the D_n value below 2.0 mm is not acceptable, as shown in Figure 17(a).

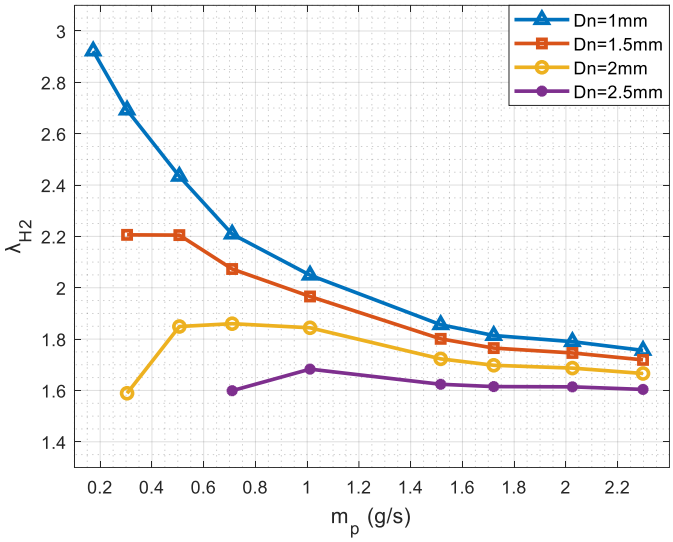

Figure 16: Effects of D_n on ejector performance

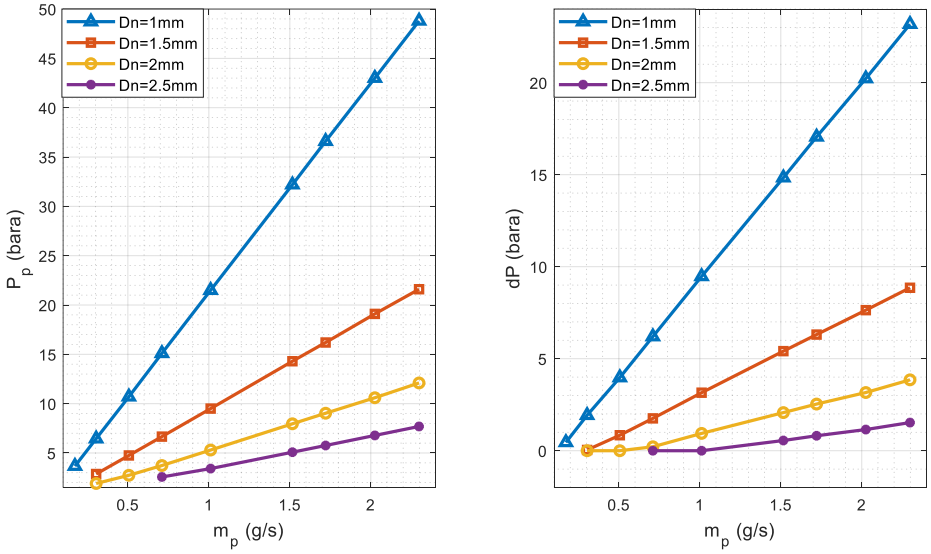

(a) (b)

Figure 17: Effects of D_n on (a) primary inlet pressure; (b) pressure difference between the nozzle throat and the suction chamber

3.2.2 Effect of Mixing Chamber Diameter D_m

The ejector entrainment capability is significantly susceptible to the ratio of constant-area mixing chamber diameter to the nozzle throat diameter D_m/D_n. The effects of different D_m/D_n on the ejector performance λ_{H_2} at fixed $D_n = 2.0\ mm, L_m = 40\ mm$ and $NXP = 3\ mm$ are presented in Figure 18. A general trend can be observed is that the

λ_{H_2} is increased as D_m/D_n increases from 3 to 5, especially at a high primary mass flow rate (i.e., high fuel cell system operating power). However, λ_{H_2} starts to decrease and is less than that at a low primary mass flow rate for $D_m/D_n = 3$ if D_m/D_n keeps increasing to 6 and above.

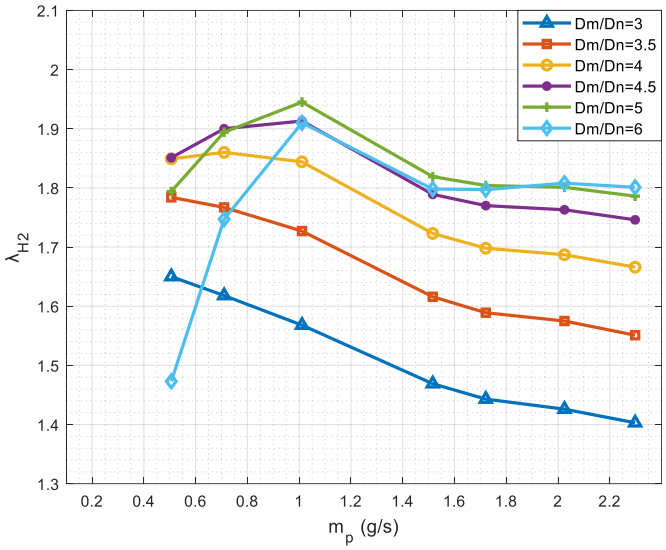

Figure 18: Effects of D_m/D_n on the ejector performance

The reason can be explained using the velocity field of H_2 flow in the ejector from the CFD simulations. As presented in Figure 19, a higher D_m/D_n ratio means larger space in the mixing chamber. For $D_m/D_n = 6$, the high velocity field only exists in a small area at the suction chamber and the forepart of the mixing chamber due to the fast diffusion and inadequate mixing of primary and secondary flow. When D_m/D_n is 3, a higher velocity exists in the entire mixing chamber, where the flow pressure can be smaller than that at $D_m/D_n = 4.5$. Since the high velocity flow from the nozzle throat diverges at the suction chamber and forms a fan area $A_{s,p}$ with only primary hydrogen flow (shown in the right corner of Figure 19), it can block the entrainment space of the second mixture flow and result in a lower λ_{H_2}. Consequently, a relatively high D_m/D_n benefits the λ_{H_2} at large primary mass flow rate conditions while a low D_m/D_n is conducive to the ejector performance at small primary mass flow rate conditions.

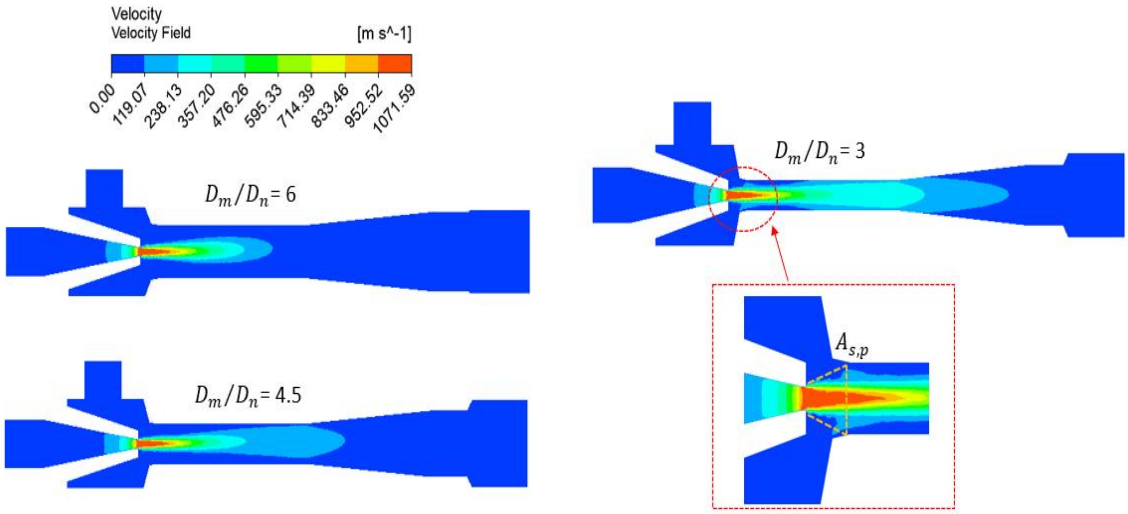

Figure 19: Velocity field of H_2 flow in the ejector at $D_m/D_n = 6, 4.5\ and\ 3$

3.2.3 Effect of Mixing Chamber Length L_m

The primary and secondary flow are combined in the mixing chamber with a constant section area before entering the diffuser chamber. The mixing chamber length, L_m, directly decides the mixing process of the two flows. It is desirable to have a long enough mixing chamber to achieve adequate and uniform mixing of the primary and secondary flows. However, the flow friction losses can also be increased along the length.

The ratio of L_m/D_m is usually adopted to investigate the effects of chamber length on entrainment performance. When other parameters are fixed, e.g. given fixed $D_n = 2\ mm, D_m = 8\ mm, NXP = 3\ mm$, the variations of ejector performance λ_{H_2} with different L_m/D_m ratios are demonstrated in Figure 20 to Figure 22.

As shown in Figure 20, the ejector performance λ_{H_2} rises from $L_m/D_m = 2$ to $L_m/D_m = 3$ in a wide range of operation because of the adequate mixing. This can also be explained by the density field of two ejectors shown in Figure 21, where it can be noticed both ejectors are similar except that the lower ejector ($L_m/D_m = 3$) is longer than the upper ejector ($L_m/D_m = 2$). The two flows are mixed adequately and reach the uniform density in the mixing chamber if $L_m/D_m = 3$, whereas the uniformly mixture only appears in the diffuser chamber for the shorter ejector $L_m/D_m = 2$. However, when L_m/D_m gradually

increases from 3 to 6, the ejector performance falls accordingly due to the increased flow friction in the longer mixing chamber. The results are specifically compared in Figure 20.

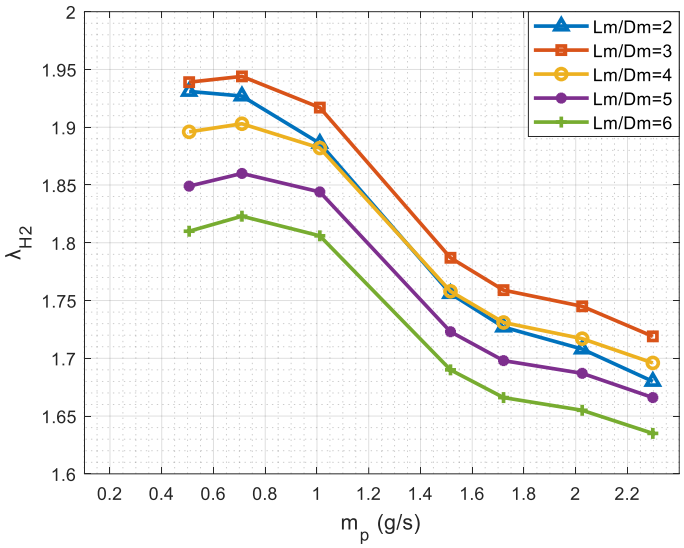

Figure 20: Effects of L_m/D_m on ejector performance

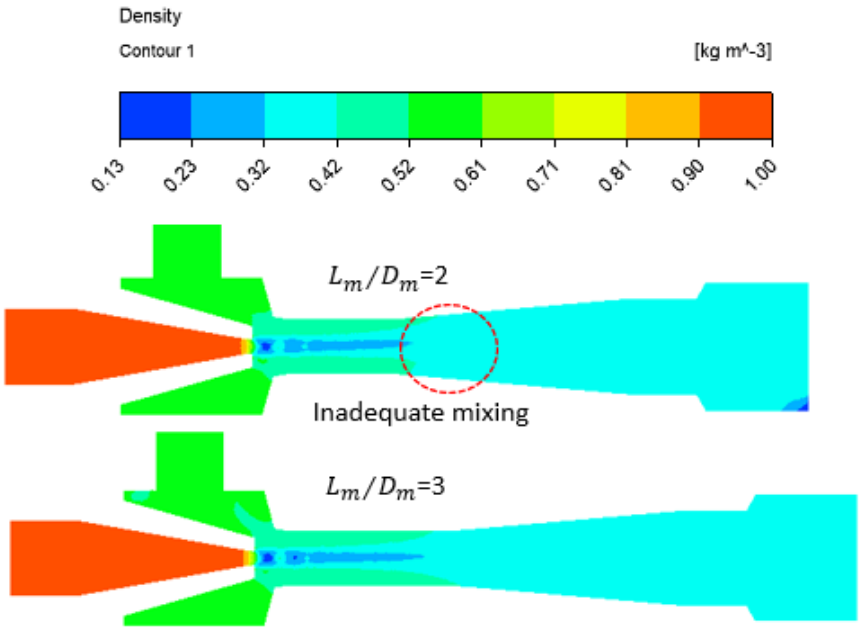

Figure 21: Density field of H_2 flow in the ejector with different L_m/D_m

To better explore the differences, the pressure field of H_2 flow in the mixing chamber along ejector length direction are compared for $L_m/D_m = 2$, 3, and 6 in Figure 22. The three vertical dot lines indicate the different lengths of the mixing chamber from the same

entrance point of the constant area mixing section to different endpoints. When $L_m/D_m = 3$, the flow pressure of the centerline on a symmetric plane is the lowest, thus, presenting the most effective entrainment capability. Conversely, the pressure is increased when $L_m/D_m = 2$ due to inadequate mixing, and when $L_m/D_m = 6$ due to the increased friction losses. The increased flow pressure in the mixing chamber can result in a poor λ_{H_2}.

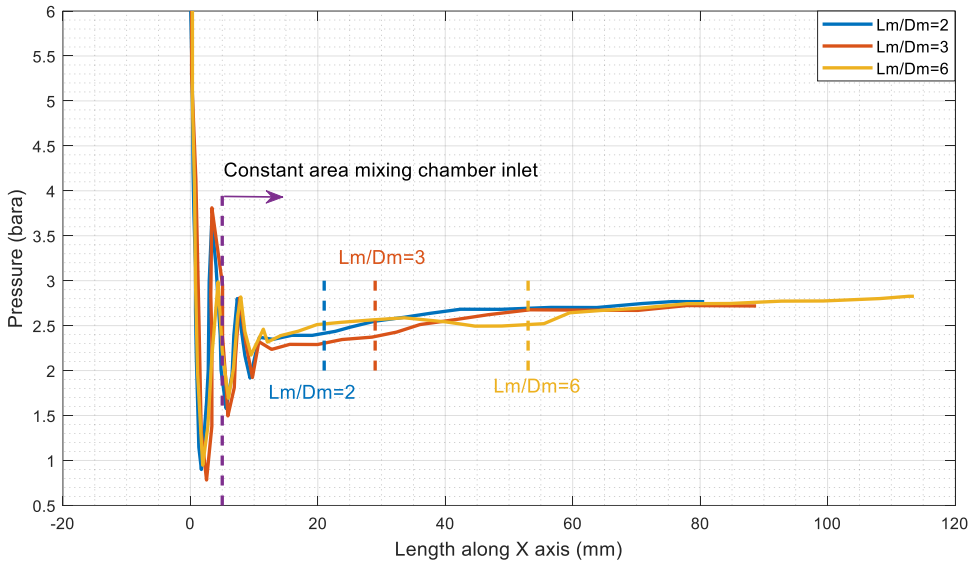

Figure 22: Pressure field of H_2 flow along the centerline of the ejector in length direction

3.2.4 Effect of Distance between Nozzle and Mixing Chamber NXP

The distance between the nozzle throat and constant pressure mixing chamber inlet NXP determines whether the pressure potential energy of the primary flow can be effectively utilized to pump the secondary mixture flow. The ejector entrainment performance λ_{H_2} of NXP varied from 0 to 10 mm are presented in Figure 23. The ejector performance has negligible differences for NXP below 6 mm. However, λ_{H_2} decreases dramatically in the whole operating range when NXP is above 6 mm.

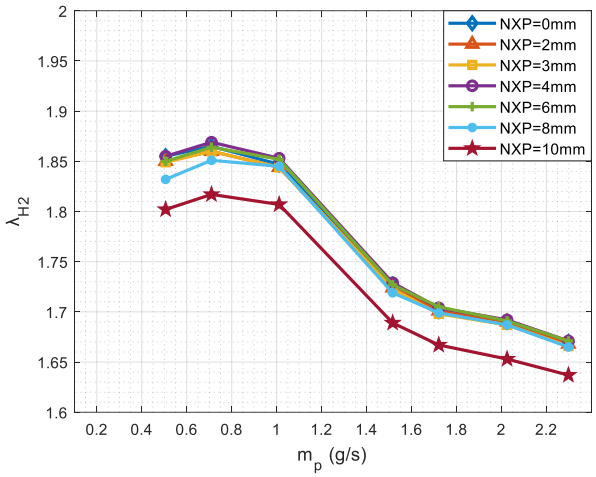

Figure 23: Effects of NXP on ejector performance

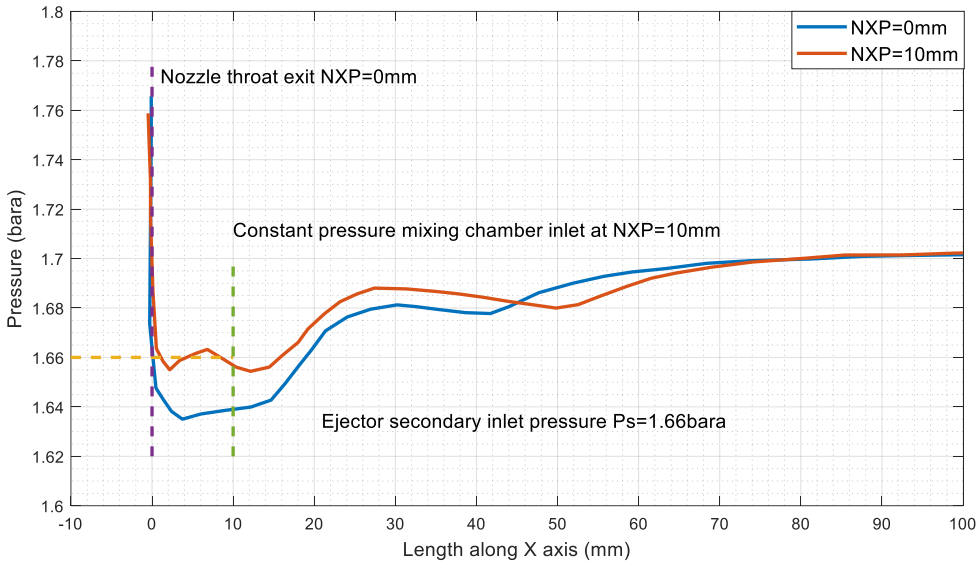

Figure 24: Pressure field of H_2 flow at different NXP in the centerline of ejector symmetric plane along the length direction

A larger NXP indicates a longer distance from the nozzle exit to the mixing chamber, which may induce a higher pressure field of H_2 flow in the ejector suction chamber and damage its entrainment capability. For example, the pressure of the ejector with $NXP = 10\ mm$ is much higher than that of $NXP = 0\ mm$, as shown in Figure 24, which shows consistency of their entrainment results in Figure 23. The primary H_2 flow with high velocity at nozzle throat exit is mainly concentrated at the suction chamber. Therefore, ejectors with larger NXP can result in large eddies of secondary flow when joining with the primary hydrogen flow. Besides, the primary flow may suffer from significant energy

losses and reduced flow velocity for ejectors with large NXP before entering into the mixing chamber, thus, reduces the λ_{H_2}.

3.2.5 Optimal Design Result of Ejector

The ejector geometric parameters can be optimized to obtain the most appropriate dimensions based on the understanding and analyses of the aforementioned key factors through CFD simulations. Here, the traditional trail-and-error method is adopted to find the optimal results of key dimensions to maximize its H_2 entrainment capability for the wide operation range of 150 kW PEMFC stack. The four key ejector dimensions are listed in Table 1. As shown in Figure 25, the ejector can provide effective H_2 gas entrainment performance and satisfy the SH_{H_2} during the mass flow range from 0.71 to 2.5 g/s, or from 49 to 150 kW operating range.

One single ejector in the HSRS cannot satisfy the full operation range of the 150 kW PEMFC stack. Therefore, it requires a novel structure and more complicated design and control of HSRS to fully cover the entire operating range of 150 kW PEMFC stack.

Table 1: Optimized ejector key geometric parameters

D_n(mm)	NXP (mm)	D_m(mm)	L_m(mm)
2	3	8	30

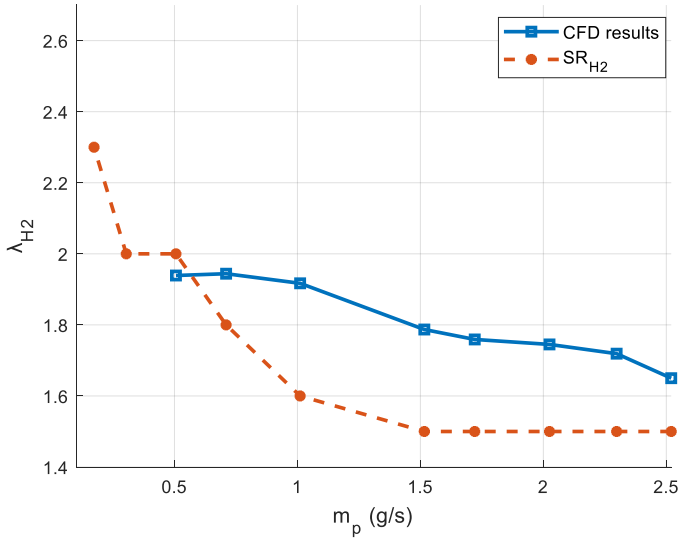

Figure 25: λ_{H_2} of ejector with optimized sizes based on CFD simulation

3.3 Influence of HSRS Operating Conditions

The HSRS operating conditions are important factors that can affect the ejector performance, including the anode inlet and outlet pressure, the pressure drops, the relative humidity, temperature, and the species mass fraction of the secondary mixture at anode outlet.

3.3.1 Effect of Anode Pressure Drop

The anode pressure drop defines the pressure boundaries from the ejector outlet to its secondary inlet, caused by the gas flow resistances through stack anode flow channels and auxiliary components. The pressure drop consists of the anode side pressure drop and the pressure resistance caused by flow pipes and the other components, such as the water separator and humidifier. Generally, the pipes' pressure drop is negligible, and the pressure drop of the water separator is below 5 kPa. Hence, the anode pressure drop is the most important factor in influencing the ejector H_2 entrainment performance.

A small change in anode pressure could dramatically reduce the ejector performance in the whole operating range, especially during the low primary flow rate, due to the less pressure potential energy between the ejector's primary inlet and secondary inlet. As defined by the aforementioned PEMFC stack anode specifications, the ejector secondary inlet pressure P_s ranges from 1.4 to 2.5 bara, and the anode pressure drop is less than 10 kPa, depending on its operating conditions. The ejector entrainment capability λ_{H_2} operating at defined P_s is plotted in Figure 26. When P_s reduces, i.e., the anode pressure drop increases, the λ_{H_2} drops significantly from around 1.8 to 0 at a primary mass flow rate of 0.5 g/s. Consequently, for those fuel cell stacks with high anode pressure drops, the ejector H_2 entrainment performance is narrowed in a limited fuel cell power operating range.

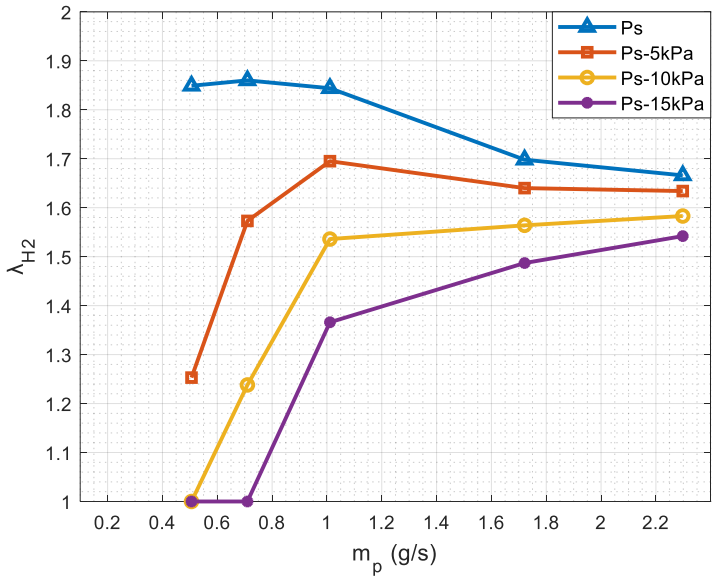

Figure 26: Effects of anode pressure drop on ejector performance

3.3.2 Effect of Secondary Flow Relative Humidity and Temperature

The ejector's secondary flow is a humid mixture consisting of water vapour, H_2, and a small amount of N_2 crossed over through the membrane from the cathode air, with high temperatures from around 353.15 K to 323.15 K. After the fuel cell stack operating for a long time, the mixture at the anode outlet contains liquid water. It can be regarded with 100% relative humidity (RH). However, at the beginning of the fuel cell operating stage, the mixture's relative humidity is lower than 100%.

The relative humidity and temperature of the secondary mixture determine the water vapour mass fraction at given flow pressure. The higher the mixture's relative humidity is, the more water vapour exists inside the mixture. Due to the high molar mass weight of the water vapour, the secondary mixture flow has a higher density at elevated relative humidity and temperature. Hence, the ejector entrainment ratio $\omega = \dot{m}_s/\dot{m}_p$ is increased parallelly in the entire operating range as RH increases from 40% to 100% at a fixed temperature, as shown in Figure 27(a). However, since the actual H_2 mass fraction is less in the mixture with higher RH, the actual λ_{H_2} is decreased as RH increases from 40% to 100%, as shown in Figure 27(b).

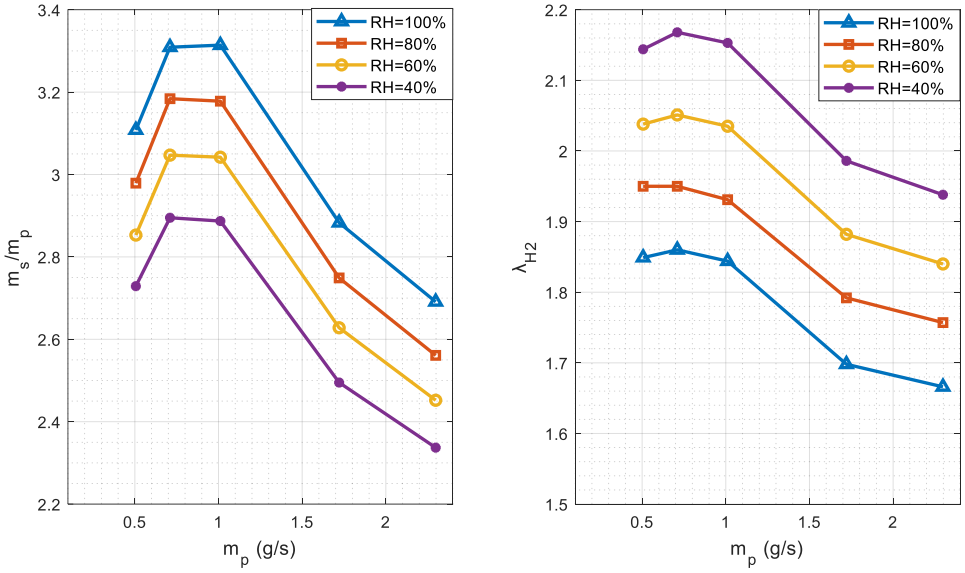

(a) (b)

Figure 27: Effects of relative humidity of anode outlet mixture on ejector performance

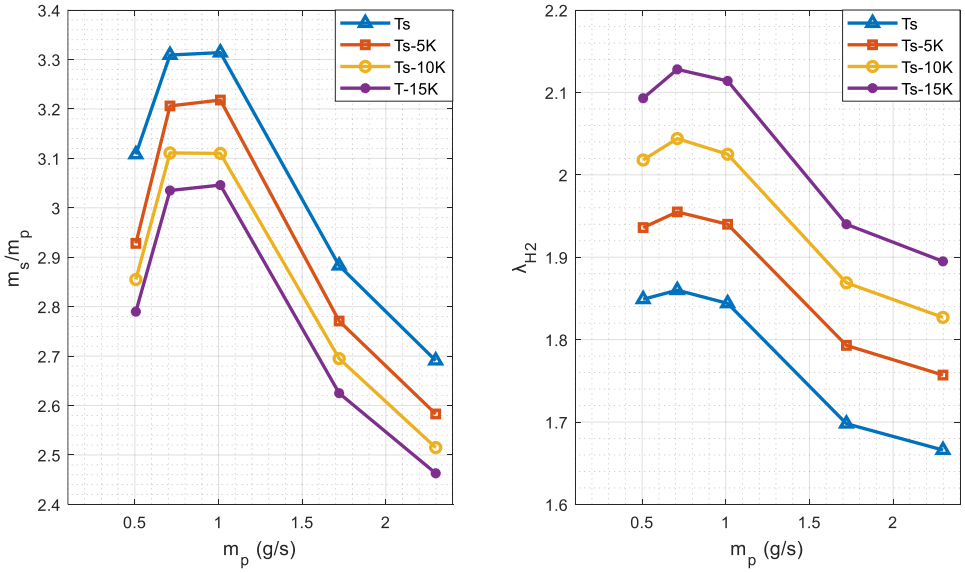

(a) (b)

Figure 28: Effects of anode outlet mixture temperature on ejector performance

Similar trends can be found on the effects of secondary mixture temperature T_s. When other condition is fixed, the mixture with higher temperature has larger water vapour partial pressure, which results in more water vapour mass fraction and less H_2 mass fraction in the mixture. Therefore, the ejector entrainment ratio $\omega = \dot{m}_s/\dot{m}_p$ is decreased if temperature

is reduced as shown in Figure 28(a). However, the actual H_2 entrainment capability is increased at lower temperature as shown in Figure 28(b).

3.3.3 Effect of Nitrogen Volumetric Fraction in the Secondary Flow

The crossover N_2 in the secondary mixture flow from the fuel cell stack cathode side has an important effect on the ejector H_2 entrainment performance. Due to the high molar mass weight of N_2, the entrained secondary mixture can get heavier if the N_2 volumetric fraction V_{s,N_2} is increased. Thus, the ejector entrainment ratio $\omega = \dot{m}_s/\dot{m}_p$ is also increased, as shown in Figure 29(a). Like the previous analysis, the actual H_2 mass fraction is reduced with increased N_2 content. Therefore, the H_2 entrainment capability λ_{H_2} is decreased with increased N_2 volumetric fraction as shown in Figure 29(b). To prevent the stack voltage deterioration, the purge process is carried out when there is too much N_2 inside the anode flow channel.

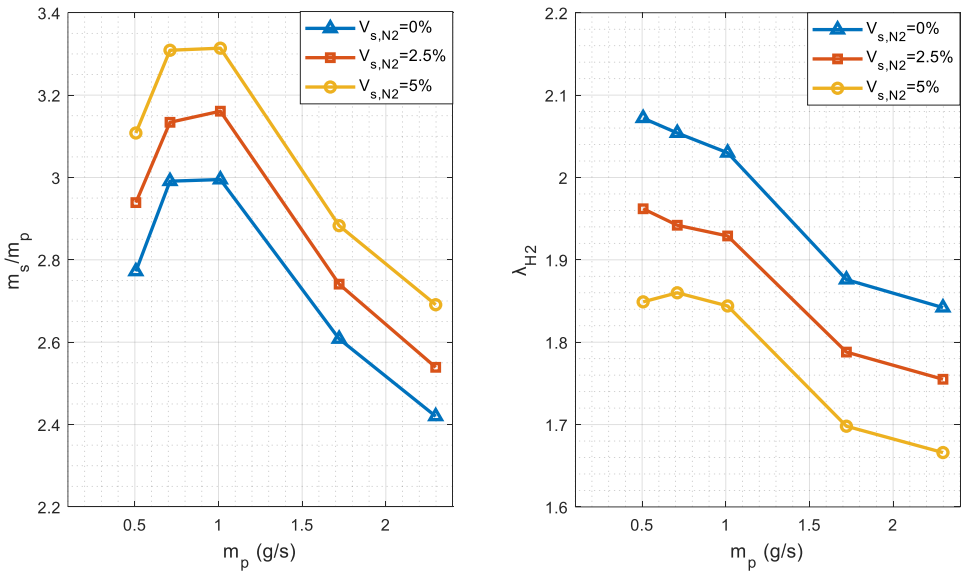

(a) (b)

Figure 29: Effects of nitrogen volume fraction at anode outlet on ejector performance

3.4 Summary

In this chapter, the CFD simulations are carried out using ANSYS Fluent to describe the pressure, velocity, temperature, and species mass fraction filed of internal compressible single-phase flow of hydrogen ejector on a 150 kW PEMFC system. The effects of ejector

key geometric parameters, as well as the HSRS operation conditions, are investigated and compared in detail to demonstrate the variations of ejector performance.

The H_2 ejector with fixed dimensions is optimized to operate effectively in a limited PEMFC system power range and can not cover the low load operation conditions. Therefore, a new structure of ejector is proposed in the next chapter to provide effective entrainment capability for the entire operating of large PEMFC stack.

Chapter 4 Optimal Design and Test of a Nested-nozzle Ejector

As discussed, the conventional gas ejector with a fixed nozzle dimension is only effective in a limited scope. A novel H_2 ejector using two nozzles is designed in this chapter to cover the entire operating power range from the PEMFC stack's maximum to idle power.

The nested-nozzle structure is the most suitable and practical solution to provide wide operating range with compact size. The difficult part is to decide the geometric parameters for different nozzles and other dimensions to achieve the best performance. In this chapter, the optimal design, simulation, and test of a nested-nozzle ejector for the 150 kW PEMFC stack is presented. Moreover, the nested-nozzle ejector is compared with dual-ejector system using two conventional ejectors in terms of the working range and anode inlet pressure fluctuation.

4.1 Optimal Design of Nested-nozzle Ejector

4.1.1 Structure Design of the Nested-nozzle Ejector

The nested-nozzle ejector designed in this research has two nozzles: a large nozzle (BN), and a small nozzle (SN). The small nozzle is nested inside the large nozzle chamber. Both nozzles are located on the same axis along the ejector length direction and share the common suction chamber, mixing chamber, and diffuser chamber. The detailed structure is demonstrated in Figure 30. Each nozzle is involved with one independent primary flow channel and a proportional valve (PV) to control its inlet mass flow rate. Specifically, the BN mode performs from the fuel cell stack maximum to a relatively low mass flow rate load. In contrast, the SN mode is responsible for operating from the minimum required mass flow rate to an operating point that can overlap with the large nozzle to ensure full coverage of the entire stack power range. The position, dimensions, and manufacturing methods of two nozzles located in a compact area are considered during the design process for practical application.

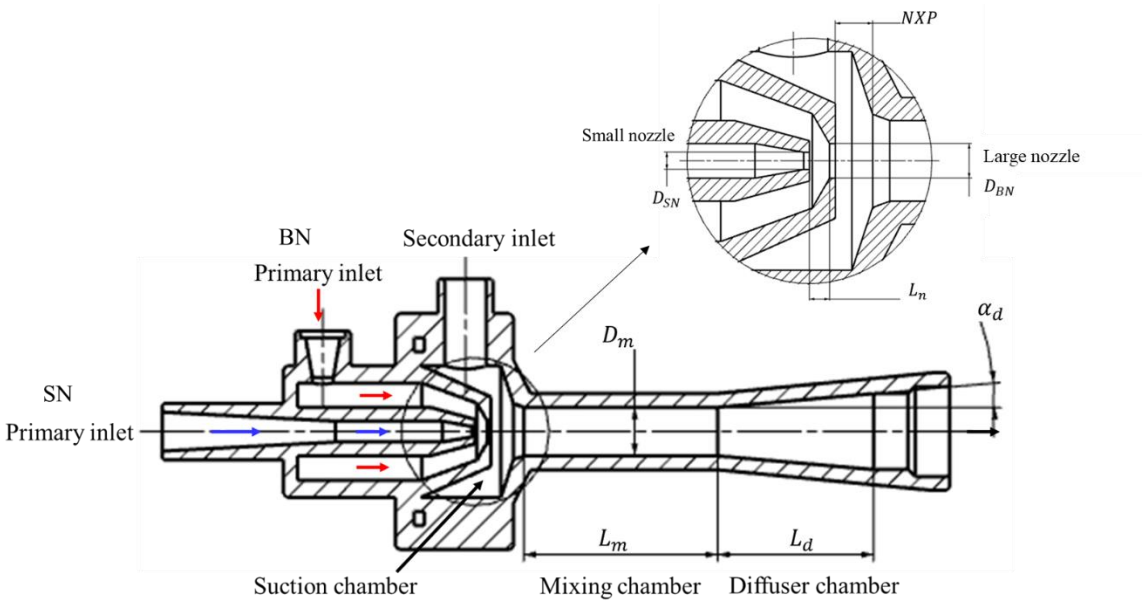

Figure 30: Symmetric graph of a nested-nozzle ejector structure

Ejector geometric parameters are key elements that must be optimized to enhance the entrainment performance. The important geometric parameters of nested-nozzle ejector include two nozzles' diameters (D_{BN}, D_{SN}), the distance between two nozzles (L_N), the mixing chamber diameter (D_m) and length (L_m) as well as the distance between the big nozzle and the mixing chamber (NXP), which can be seen in Figure 30.

The CFD simulations using ANSYS Fluent are applied to evaluate the ejector flow properties. The CFD simulations adopt a pressure-based solver with the SST k-ω model. The governing equations of mass, momentum, and energy of hydrogen flow and assumptions on simulations are the same as in previous chapters. Moreover, the trial-and-error method is applied to optimize geometric parameters to ensure the nested-nozzle ejector satisfies the required SR_{H2}. Figure 31 shows the optimization process of the geometric parameters.

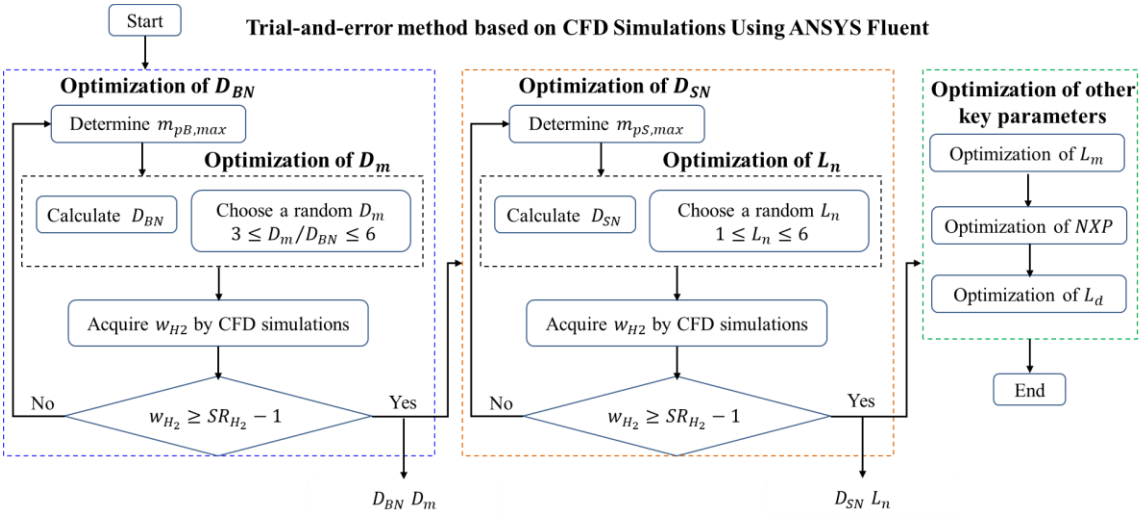

Figure 31: Optimization process of key geometric parameters of the nested-nozzle ejector

Boundary conditions of the CFD simulations are set according to the PEMFC stack specifications and shown in Table 2. The primary inlets of both BN and SN modes are applied with mass flow rate inlets using pure H_2 $\dot{m}_p$ at 293.15 K, while the ejector secondary inlet and outlet are pressure inlet and outlet, respectively. The secondary inlet mixture consists of H_2, water vapour and N_2. The volumetric fraction of N_2 in the mixture V_{s,N_2} is assumed as 5%, and the relative humidity of the secondary mixture is 100 %. The ejector secondary inlet pressure P_s and temperature T_s are identical to those of the anode outlet, neglecting the pressure drop from the anode outlet to the ejector's secondary inlet. The ejector outlet pressure P_d is equal to the anode inlet pressure.

Table 2: CFD simulation boundary conditions of the nested-nozzle ejector

Boundary conditions	BN mode	SN mode
Primary inlet of the large nozzle	$\dot{m}_{pB}$ (kg/s) , 293.15 (K)	N.A.
Primary inlet of the small nozzle	N.A.	$\dot{m}_{pS}$ (kg/s) , 293.15 (K)
Secondary inlet	P_s (bara), T_s (K), V_{s,N_2} (%), V_{s,H_2O} (%)	
Discharge outlet	P_d (bara)	

4.1.2 Optimization of Nested-nozzle Ejector Geometric Parameters

Optimization of D_{BN} and D_{SN}

The most important geometric parameters of nested- nozzle ejectors are the nozzle diameters D_{BN} and D_{SN}, which determines the primary flow velocity and pressure in the suction chamber and can greatly affect the ejector's overall entrainment capability [38]. As

stated before, the ejector nozzle diameter is determined by the maximum theoretical H_2 consumption rate $\dot{m}_{p,max}$. Here, the $\dot{m}_{p,max} = 2.52$ g/s for PEMFC stack operating at maximum of 150 kW, shown as the green dot line in Figure 32. However, the design of nozzle diameter also needs to consider the PVs' performance to ensure the required maximum flow rate can be satisfied.

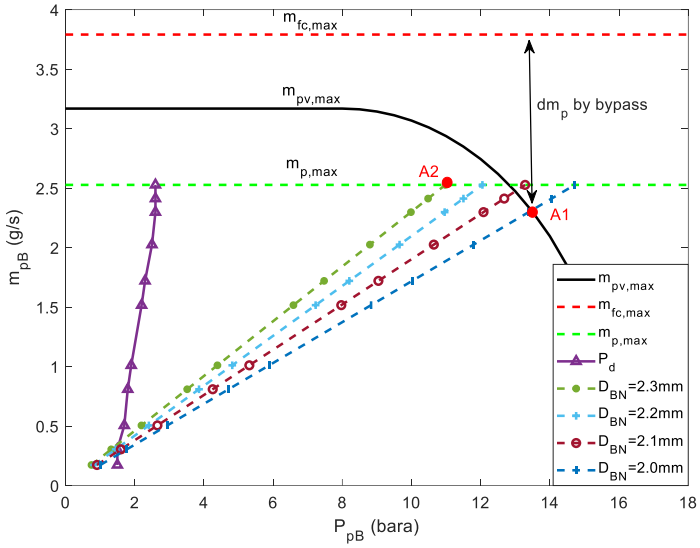

Figure 32: The relationship between the primary flow rate $\dot{m}_{pB}$ and the primary pressure P_{pB} at different diameters D_{BN}

The PV's maximum mass flow rate $\dot{m}_{pv,max}$ is a critical factor in the optimal design of D_{BN}. The $\dot{m}_{pv,max}$ is influenced by the pressure difference between the PV's inlet and outlet (i.e., the ejector's primary inlet P_{pB}) with a fixed orifice area, which drops when the ejector primary inlet pressure rises from a certain point, shown in Figure 32. Currently, the suitable PV available on the market for high-power PEMFC stacks, to the author's best knowledge, can only provide $\dot{m}_{pv,max}$ of 3.17 g/s at 100% duty cycle and high-pressure difference. Considering the stoichiometric ratio SR_{H_2} 1.5 at 150 kW, the maximum H_2 mass flow rate required by the fuel cell stack $\dot{m}_{fc,max}$ can reach up to 3.78 g/s, which is a big challenge for the PV. Therefore, D_{BN} should be at least larger than 2.2 mm to supply the excess hydrogen requirement.

However, a smaller D_{BN} is desirable and beneficial to enlarge the fuel cell operating power range. According to the flow choking phenomenon at the nozzle exit, the large nozzle's P_{pB} increases when the D_{BN} decreases at a fixed mass flow rate m_{pB}, hence,

providing larger pressure potential energy between the P_{pB} and P_d. As shown in Figure 32, the operating point A1 when $D_{BN} = 2.0$ mm, compared to the operating point A2 at $D_{BN} =$ 2.3 mm, has more potential energy and, thus, better entrainment capability. The $\dot{m}_{pv,max}$ cannot provide the $\dot{m}_{p,max}$ with 2.52 g/s when D_{BN} is below 2.2 mm, much less to the $\dot{m}_{fc,max}$. Two or more paralleled PVs may satisfy both $\dot{m}_{p,max}$ and $\dot{m}_{fc,max}$ at D_{BN} below 2.2 mm. However, it increases the system costs and complexities during the design, manufacturing, and control development. Consequently, a lower point on the line of $\dot{m}_{pv,max}$, if properly decided to get a smaller D_{BN}, can enlarge the ejector effective working range, provided that a bypass is applied in the HSRS.

The bypass with a small proportional valve PV3 can remedy the deficiencies dm_p between $\dot{m}_{pv,max}$ and $\dot{m}_{fc,max}$. With the help of a bypass, D_{BN} can be designed with 2.0 mm and still fulfill the requested SR_{H_2} at maximum 150 kW. The CFD simulation results of H_2 entrainment performance ω_{H_2} of BN mode with and without bypass are shown in Figure 33(a). When D_{BN} is 2.2 mm, the BN mode can provide an effective ω_{H_2} during the $\dot{m}_{pB}$ range from 2.52 g/s to 0.71 g/s. When D_{BN} is 2.0 mm, the lower limit of effective ω_{H_2} is extended to $\dot{m}_{pB}$ 0.51 g/s, meanwhile, the upper limit can still be maintained at $\dot{m}_{p,max}$ 2.52 g/s with the assistance of bypass. In detail, the boundary conditions of CFD simulation at point A3 are set to be identical to those at the maximum fuel cell power of 150 kW, except $\dot{m}_{pB}$ is limited to 2.30 g/s due to $\dot{m}_{pv,max}$. The A3 point at D_{BN} 2.0 mm succeeds to entrain enough unused hydrogen ω_{H_2} 0.69 to satisfy the SR_{H_2} 1.5 at fuel cell maximum power 150 kW. The bypass supplements the remaining dm_p 1.48 g/s. Besides, single choking mode (SCM) ends at $\dot{m}_{pB}$ 0.51 g/s for D_{BN} 2.0 mm instead of $\dot{m}_{pB}$ 0.71 g/s for D_{BN} 2.2 mm, which extends the lower limit of the ejector's effective working range from 49 kW to 38 kW. Consequently, the BN mode with properly managed $\dot{m}_{pB}$ and optimally designed D_{BN} can satisfy the maximum required $\dot{m}_{fc,max}$ and extend the lower limit of the ejector effective working range.

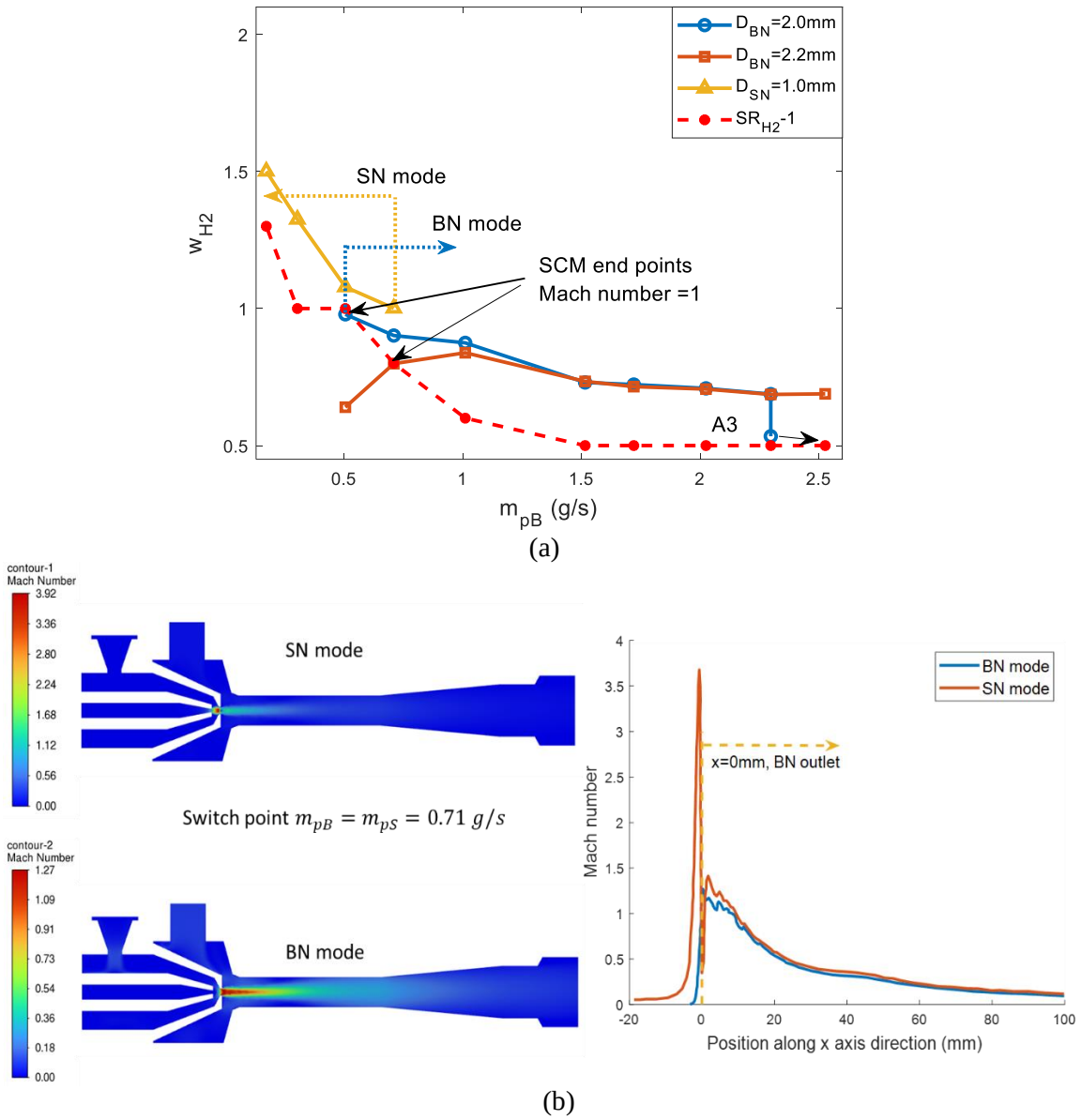

Figure 33: (a) The ω_{H_2} of BN mode and SN mode; (b) the velocity field of internal flow and Mach number at the center line of the nozzle of BN and SN mode at $\dot{m}_p$ 0.71g/s.

The SN diameter D_{SN} is determined by the lower limit of the primary mass flow rate of BN. An operation overlap (shown in Figure 33(a)) between the BN and SN mode is reserved to achieve a smooth transaction between the two modes. Moreover, the PEMFC stack output power will reduce due to the PEMFC performance degradation after a long run. To maintain a certain output power, the primary mass flow rate $\dot{m}_{pS}$ must be increased. The appropriate overlap can ensure a robust design with a safer margin and more flexible control. Figure 33(b) shows the velocity field of internal H_2 flow in BN mode and SN

mode. The combined flow in the suction and mixing chamber accelerates to a higher Mach speed using SN mode than BN mode at switching operation condition $\dot{m}_p$ of 0.71g/s, providing more pressure potential energy to acquire a larger ω_{H_2}. Hence, the upper limit of $\dot{m}_{pS}$ is designed at 49 kW (0.71g/s) instead of 38 kW (0.51g/s), and the corresponding D_{SN} is 1.0 mm. Based the CFD simulations, the SN mode covers the fuel cell operation range of minimum 0.17 g/s to maximum 0.71 g/s.

In conclusion, the D_{BN} is optimally designed to be 2.0 mm, considering the limitations of PVs and the performance of a bypass in the HSRS. Using strategical control of BN and a bypass, the operation range of BN mode is designated from a maximum of 150 kW (2.52 g/s) to the lower boundary of 38 kW (0.51 g/s). Moreover, the D_{SN} is optimally designed to be 1.0 mm, covering from a minimum of 13.9 kW (0.17 g/s) to a maximum of 49 kW (0.71 g/s). A slight overlap from 38 to 49 kW between the two modes is considered. Together, the nested-nozzle ejector satisfies the SR_{H_2}, over the entire range of PEMFC operation from the maximum power of 150 kW to the idle power of 13.9 kW.

Optimization of L_n

The distance L_n between BN and SN determines the primary flow velocity and pressure in the suction and mixing chambers when using the SN mode. Figure 34(a) shows the CFD simulation results of H_2 entrainment ratio ω_{H_2} for both BN and SN with respect to L_n ranging from 2 to 5 mm. For the BN mode, ω_{H_2} is not sensitive to L_n above 3 mm during the whole operation range. L_n under 3 mm could narrow the flow channel and limit the $\dot{m}_{pB}$, therefore, reduce the ω_{H_2}. To maintain the abundant hydrogen supply, L_n should be kept at least 2 mm in this case. As for the SN mode, the L_n has an opposite effect on ω_{H_2} compared with BN mode. A smaller L_n can tremendously increase the ω_{H_2} at low primary mass flow rate conditions. When L_n is above 4 mm, the ω_{H_2} decreases quickly as $\dot{m}_{pS}$ reduces from 0.51 g/s to 0.17 g/s. With a smaller L_n, more kinetic energy from the primary flow can enter the suction and mixing chamber to create a large high-speed and low-pressure flow area, indicated by the red cycle of Figure 34(b). The static pressure of the combined H_2 mixture in the mixing chamber with L_n =2 mm is lower than that with L_n =5 mm, shown in Figure 34(c), thus, generates higher pressure differences between the

secondary inlet and mixing chamber. This increased pressure potential energy significantly improves the ω_{H_2} especially when the SN operates at the extreme low $\dot{m}_{pS}$ 0.17 g/s. Consequently, the optimal L_n for both BN and SN mode is decided to be 2 mm.

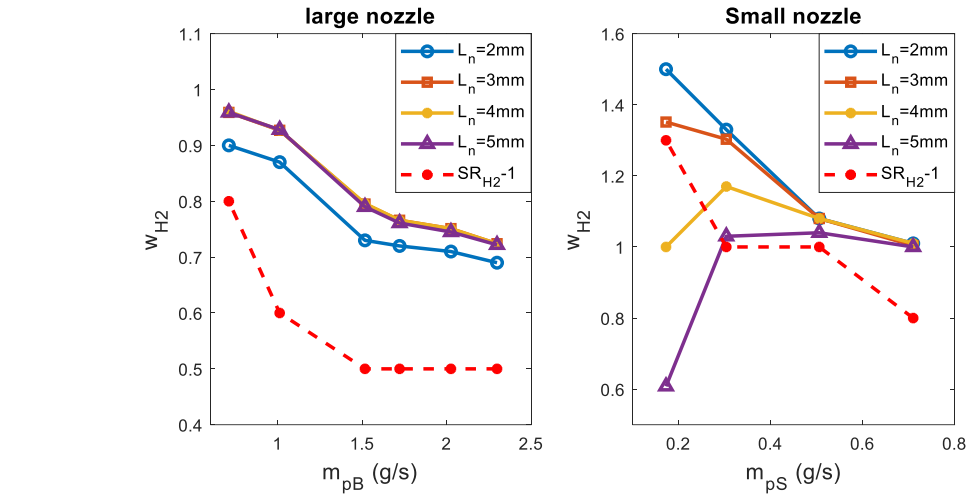

(a)

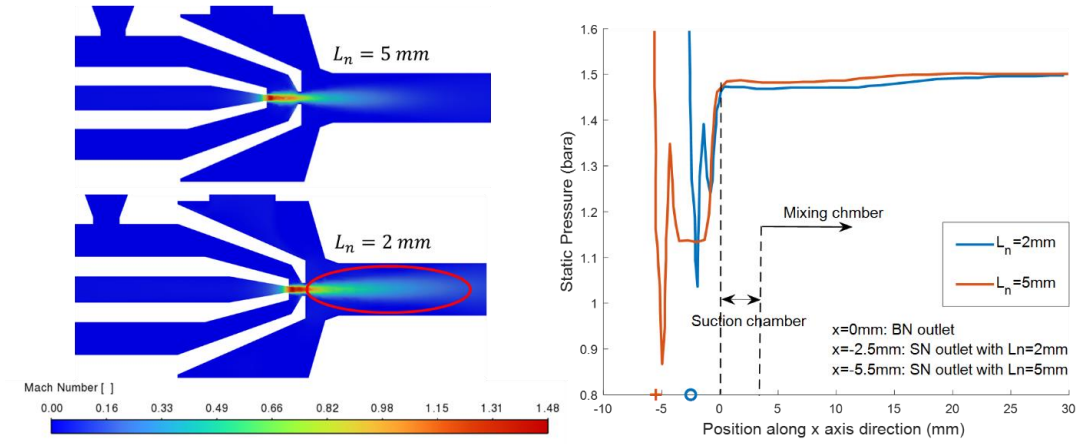

(b) (c)

Figure 34: (a) Effects of L_n on the H_2 entrainment performance for BN and SN mode; (b) and (c) are the velocity field and static pressure distribution of the ejector internal hydrogen flow using SN mode with different L_n at $\dot{m}_{pS}$ 0.17 g/s.

Optimization Results

The other parameters, such as the mixing chamber diameter D_m and length L_m, the distance between the big nozzle and the mixing chamber NXP, and the length L_d of the diffuser chamber also affect the ω_{H_2}. Each parameter has a lower and upper boundary and is closely related to the nozzle diameters [17, 43, 44]. The trial-and-error method based on

CFD simulations is applied to determine these key parameters. The optimized nested-nozzle ejector geometries are specified in Table 3.

Table 3: Key geometries of the nested-nozzle ejector

Parameter	Valve
Large nozzle diameter D_{BN}	2 mm
Small nozzle diameter D_{SN}	1 mm
Minimum nozzle wall thickness	1 mm
Nozzle distance L_n	2 mm
Distance NXP	3 mm
Mixing chamber D_m	8 mm
Mixing chamber length L_m	30 mm
Diffuser length L_d	33.6 mm
Diffuser convergent angle α_d	5°

4.1.3 HSRS Design Using Nested-nozzle Ejector and Bypass

The simplified HSRS structure using one nested-nozzle ejector and one bypass is shown in Figure 35. After reduced to the targeted pressure (in this case, 16 bara) through a pressure regulator, the compressed pure H_2 flow from the storage tank is delivered to the ejector primary inlets through H_2 proportional valves (PV). PV1 and PV2 are determined to adjust the pressure and mass flow rate for the large and small nozzles, respectively. PV3 can operate independently as a bypass channel or pair with PV1 and PV2 in different operation modes.

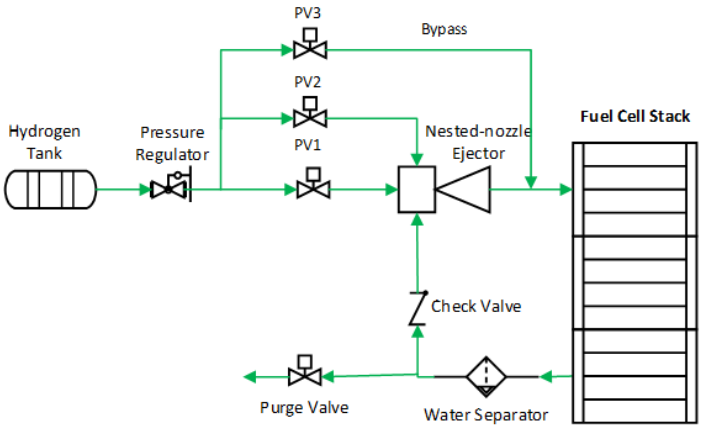

Figure 35: Schematic of HSRS using a nested-nozzle ejector and a bypass

The bypass in the HSRS system can also be used together with a purge valve to purify the H_2 when there is accumulated water and N_2 in anode flow channels. In this research, the bypass has two functions, to quickly respond ejector's dynamic power changes and to

extend the nested-nozzle ejector working range. The H_2 gas humidifier is eliminated in the HSRS system by taking advantage of the secondary inlet mixture (with 100% relative humidity) to humidify the dry primary H_2.

4.2 Manufacturing and Test

The nested-nozzle production and manufacturing must carefully consider the product material and manufacturing method for real-life application in PEMFC systems. In this research, two different methods are compared: wire-cutting machining and 3D metal printing technology. The roughness of general 3D printing using metal material may generate an uneven and unsmooth internal nozzle surface, which may narrow the nozzle orifice. Hence, the wire-cutting machining technology using stainless steel is applied to manufacture the nested-nozzle ejector since it can precisely control the manufacturing error within 0.01 mm with improved surface roughness and lower cost.

(a)

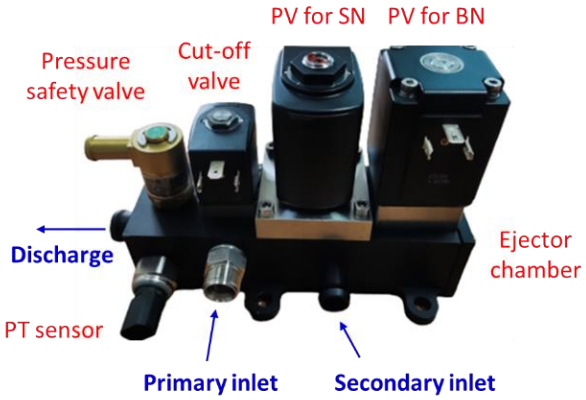

(b)

Figure 36: (a) The stainless steel nested-nozzle ejector produced using the wire cutting method; (b) the integrated nested-nozzle ejector assembly

The ejector sample product is shown in Figure 36(a), where the left part consists of nested BN and SN with two primary inlets, and the right part consists of the suction chamber,

mixing chamber and diffuser chamber. In addition, the nested-nozzle ejector assembly is developed to further reduce the size and weight of the HSRS, shown in Figure 36(b), including the nested-nozzle ejector, one pressure and temperature sensor, two hydrogen PVs, one pressure safety valve, and one cut-off valve.

The test bench shown in Figure 37(a) is designed to validate the nested-nozzle ejector entrainment performance under different PEMFC stack operation conditions. Ambient air is used instead of H_2 gas during the test for safety and economic considerations. An air pump with a maximum of 11 bara supplies the primary and secondary inlet flows. A mass flow rate controller (MFC) is applied before the proportional valves to adjust the required primary flow's mass flow rate. Two back pressure valves and their controllers (BPVC) are installed to adjust the required pressures at the ejector secondary inlet and outlet according to the stack working conditions. Three integrated pressure and temperature sensors (PT) and mass flow rate meters (MFM) are used to monitor the pressure, temperature, and mass flow rate at the ejector's inlets and outlet, respectively. This test bench is only applicable for testing the nested-nozzle ejector entrainment capability. The pressure fluctuation at the ejector outlet when switching between the BN and SN modes is also a primary concern in an application. Hence, another test bench is built to investigate the pressure fluctuation as shown in Figure 37(b). A gas tank and a water separator are added to the system to simulate the real scenario of the PEMFC application. The tank connected with the ejector outlet is a simulator of the PEMFC stack, where the theoretically reacted hydrogen consumed by the stack in each operating point is released using an MFC. The rest of the gas from the tank needs to pass through the water separator to account for its pressure drop in actual HSRS before returning to the ejector's secondary inlet. Therefore, the pressure fluctuation during the shifting process between BN and SN mode can be investigated in a closed-loop system with accurate results.

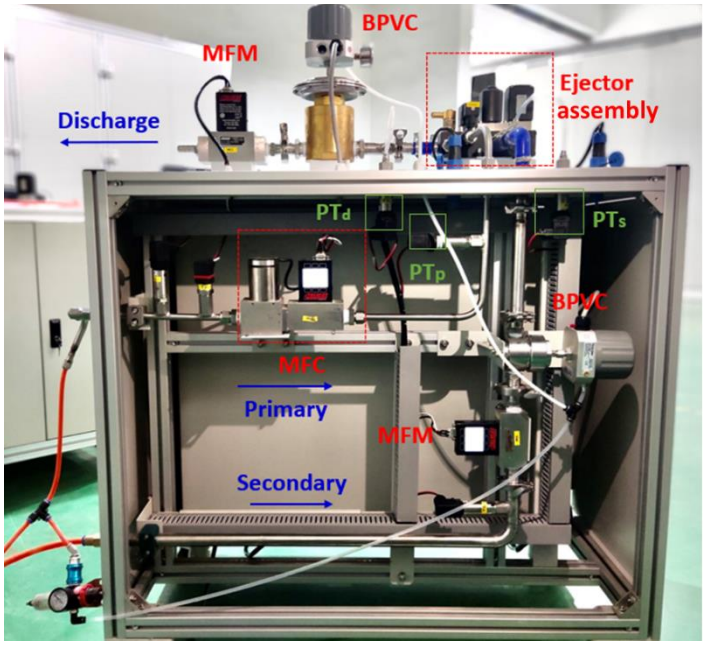

(a)

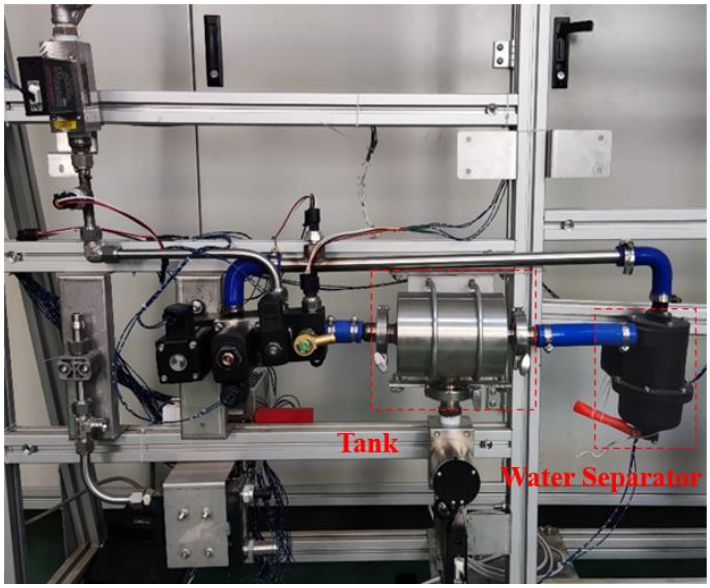

(b)

Figure 37: Photograph of the test bench for (a) the nested-nozzle ejector entrainment performance; (b) the pressure inspection during switching between BN and SN mode

4.3 Simulation and Test Result Comparison and Discussion

The CFD simulation results of the optimally designed nested-nozzle ejector are compared with test data from the bench using air as working gas and the same boundary conditions. The comparison validates the design feasibility and manufacturing precision.

First, CFD simulations and test results of primary pressures for BN and SN, $P_{p\mathrm{B}}$ and $P_{p\mathrm{S}}$ with respect to the designed mass flow rate $\dot{m}_{p\mathrm{B}}$ and $\dot{m}_{p\mathrm{S}}$, are almost identical, as shown in Figure 38(a). The actual D_{BN} and D_{SN} can be calculated using measured $P_{p\mathrm{B}}$ and $P_{p\mathrm{S}}$. The results demonstrated that D_{BN} is around 99% of its targeted valve 2.0 mm while D_{SN} is approximate 101.5% of 1.0 mm, indicating high accuracy of manufacturing precision using wire-cutting machining technology. Hence, the influence of machining error on the ejector entrainment capability can be omitted.

Second, comparisons of the ejector air entrainment ratio between CFD and test results are shown in Figure 38(b). For BN mode, simulated results agree well with test results in a high primary mass flow rate. For SN mode, the relative error between CFD and test results is within 14% in a low primary mass flow rate. The mean absolute percentage error (MAPE) is adopted to evaluate the differences. The MAPE is 5.51% for BN mode and 10.28% for SN mode which shows a good consistency between the CFD and test results.

$$MAPE = \frac{1}{n}\sum_{i=1}^{n}\left|\frac{\omega_{air,test(i)} - \omega_{air,CFD(i)}}{\omega_{air,test(i)}}\right| \times 100\% \tag{4.1}$$

where n is the number of test points.

Since the gas properties of H_2 and air are quite different, the ejector entrainment performance may be different when changing from air to H_2. To get the real ejector H_2 entrainment ratio, using hydrogen gas in the test bench or installing the nested-nozzle ejector on a real PEMFC system is the only solution. In this research, it is assumed that the tested results using H_2 has the identical MAPE of results using air. The corrected ejector H_2 entrainment ratio using MAPE of air entrainment ratio is calculated to represent the real performance using H_2. Figure 39 shows that the corrected ω_{H_2} of both BN and SN modes still satisfies the stack required SR_{H_2} during the whole PEMFC system operating power.

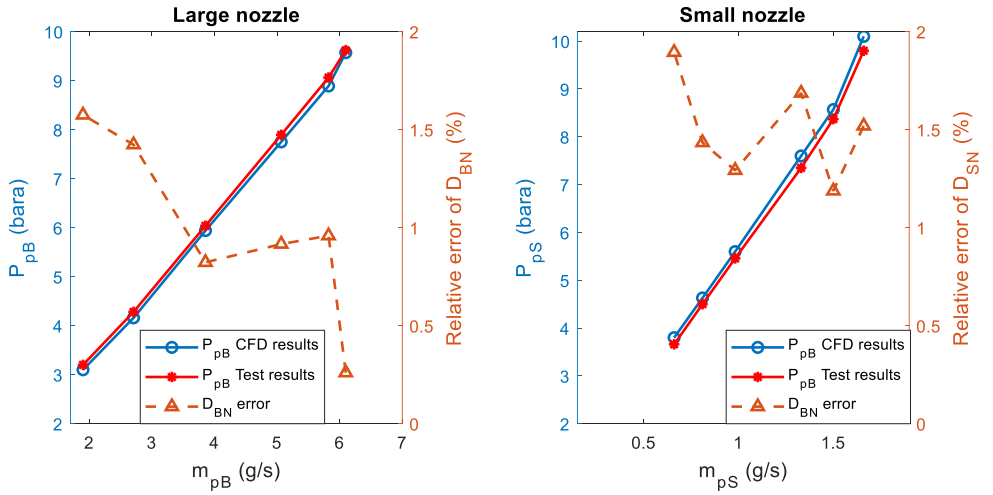

(a)

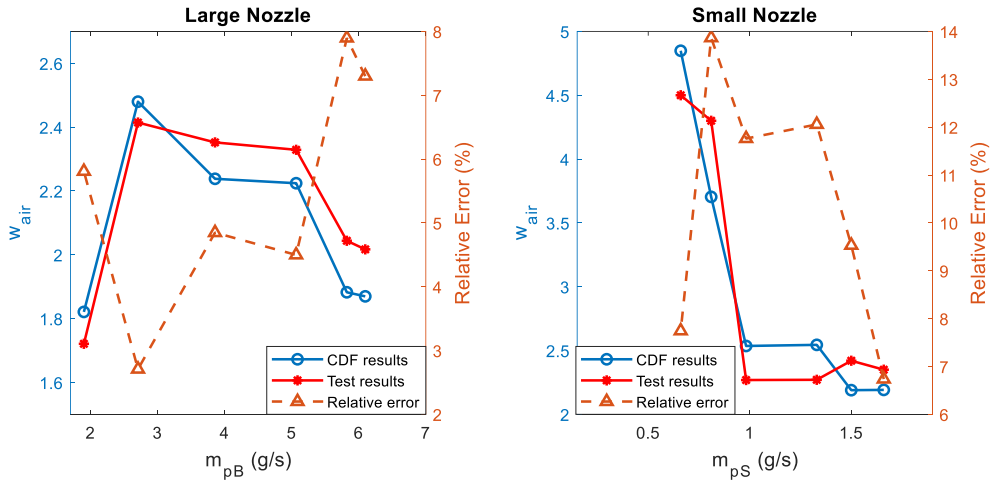

(b)

Figure 38: Results comparisons between test and CFD simulation results: (a) the primary, secondary mass flowrates, and diameters' deviation for BN and SN, respectively; (b) the air entrainment ratio and relative error for BN and SN from CFD simulations and tests, respectively.

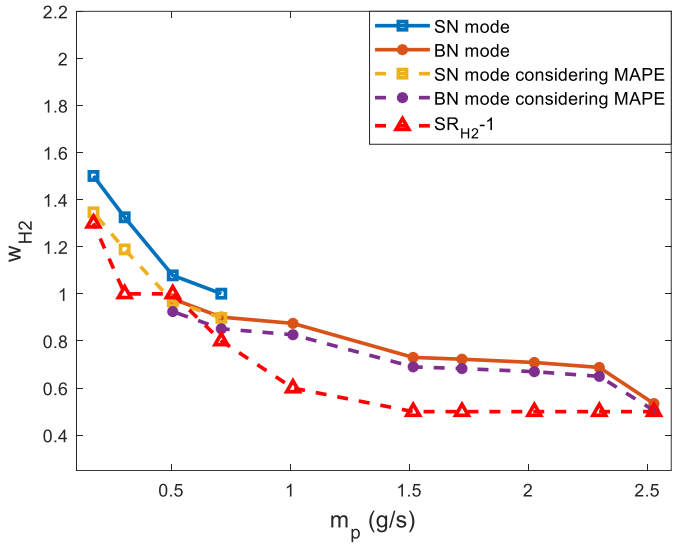

Figure 39: Hydrogen entrainment ratio of nested-nozzle ejector considering the MAPE

4.4 Comparison Between the Nested-nozzle Ejector and Dual-ejector System

4.4.1 Comparison of Ejector Hydrogen Entrainment Performance

Using two-paralleled ejector in HSRS can achieve similar effects as nested-nozzle ejector. The effective working range are compared between the nested-nozzle ejector and the dual-ejector. The HSRS using dual-ejector is cumbersome with more auxiliary parts shown in Figure 40. It includes a large ejector A which takes responsibility of the stack high power loads and a small ejector B which works at stack low power conditions. Each ejector has a PV to regulate the primary mass flow. Besides, a three-way valve switches the gas recirculation channels between the ejector A and B according to control strategies.

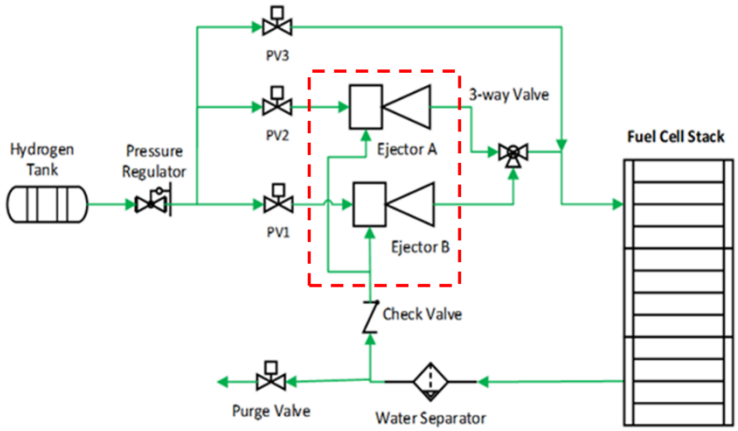

Figure 40: Schematic of HSRS using dual-ejector

The geometric parameters of both ejectors A and B in the dual-ejector system are optimally designed using the method mentioned earlier through CFD simulations. Their specific geometries are demonstrated in Table 4. The geometries of ejector A are identical to the BN of the nested-nozzle ejector, including the nozzle diameter, mixing chamber and diffuser chamber. Hence, there is no difference on the ω_{H_2} between the BN mode from the nested ejector and ejector A in the dual-ejector system. The nozzle diameter of ejector B is 1.0 mm, which is the same as D_{SN}, however, other geometries are optimized through the CFD simulations, including the mixing chamber diameter D_m of 6 mm and length L_m of 24 mm. As shown in Figure 41, both the dual-ejector and nested-nozzle ejector can cover the PEMFC's power operation range from 150 kW to 13.9 kW (2.52 to 0.17 g/s). Moreover, ejector B, with optimized geometry, provides a larger ω_{H_2} than SN mode of nested-nozzle ejector during the low power range from 49 to 13.9 kW (0.71 to 0.17 g/s).

Table 4: Key geometries of the dual-ejector

Parameter	Ejector A	Ejector B
Nozzle diameter D_n (mm)	2	1
Minimum nozzle wall thickness (mm)	1	1
Distance NXP (mm)	3	2
Mixing chamber D_m(mm)	8	6
Mixing chamber length L_m(mm)	30	24
Diffuser length L_d(mm)	33.6	
Diffuser convergent angle α_d (°)	5	

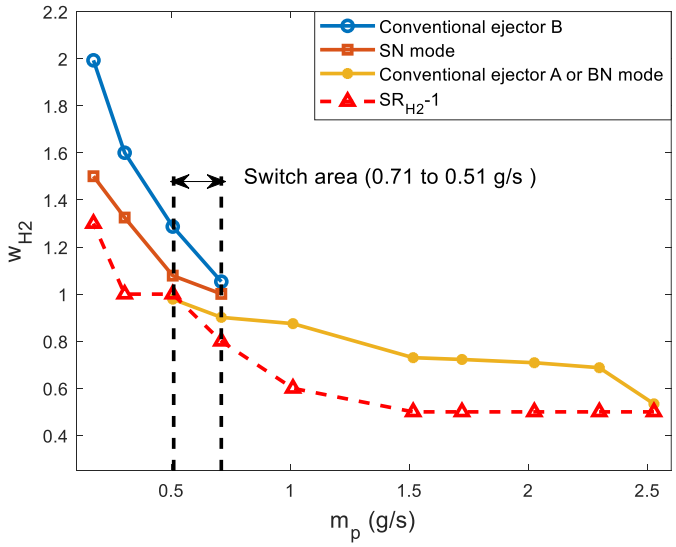

Figure 41: Comparison of the H_2 entrainment performance ω_{H_2} between dual-ejector and nested-nozzle ejector

4.4.2 Comparison of System Pressure Fluctuation

The dual-ejector and nested-nozzle ejector systems involve two different gas paths where each path is equipped with a PV and connected to an ejector or a nozzle. The three-way control valve in the dual-ejector system switches the gas recirculation path between ejector A and ejector B back and forth, depending on the system control strategies. The different sizes and lengths of the flow chambers lead to flow rate variations during the switching process and cause system pressure fluctuation. As required, the stack's anode inlet pressure P_d should be maintained stable, and the pressure differences between the anode and cathode should be adequately controlled. Drastic pressure fluctuation at the anode inlet may cause accumulated damage to the membrane and degrade its performance.

The pressure fluctuation influenced by the transit process of changing flow channels in the dual-ejector and the nested-nozzle system is compared using experimental tests. Figure 42(a) shows the primary inlet pressure P_p changes between about 3.3 and 7.9 bara when switching between ejector A and B. As a result, the ejector discharged gas pressure P_d encounters disturbance due to the varied gas pressure and volume between the two paths. When the gas path is switched, the PV must control its pressure while maintaining the same primary mass flow rate. The anode inlet pressure fluctuation dP_d of dual-ejector system is also plotted in Figure 42(a). With the optimal control of proportional valves' opening and closing time, the dP_d is within 12 kPa when switching from the ejector A to B and 44 kPa oppositely. The pressure difference of 44 kPa exceeds the maximum acceptable pressure fluctuation of 30 kPa [45].

The same experimental conditions are applied to the nested-nozzle ejector to measure its pressure fluctuation when switching between BN and SN mode. The control of proportional valves is plotted in the lower part of Figure 42(b) to demonstrate the duty cycle changes during the transit process. The ejector discharged gas pressure P_d is measured and plotted in the upper part of Figure 42(b) when switching between the two modes. P_d can maintain constantly at targeted valve 1.85 bara, and the pressure fluctuation dP_d is negligible during the transit process.

Consequently, although the dual-ejector provides a larger ω_{H_2} in the lower power load conditions, the P_d fluctuation has a great improvement when using the nested-nozzle

ejector. The main reason is the nested-nozzle ejector is more compact with the two nozzles sharing the common suction chamber, mixing chamber, diffuser chamber and flow channels.

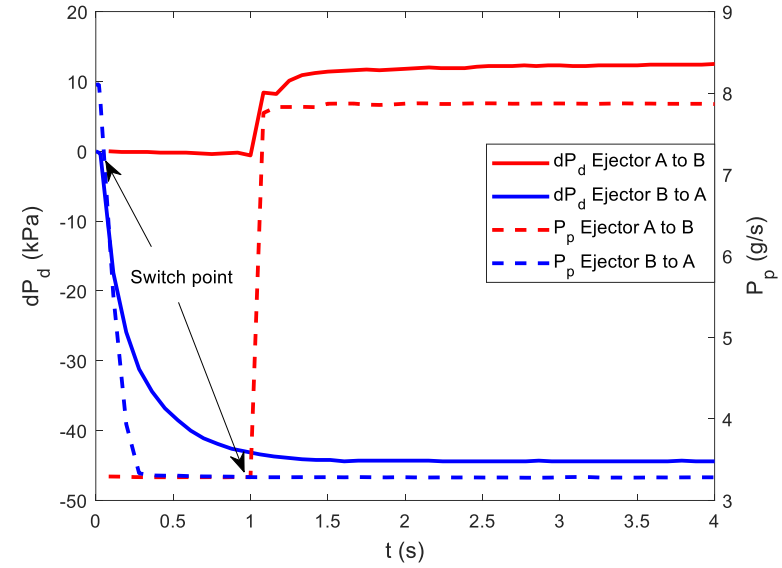

(a)

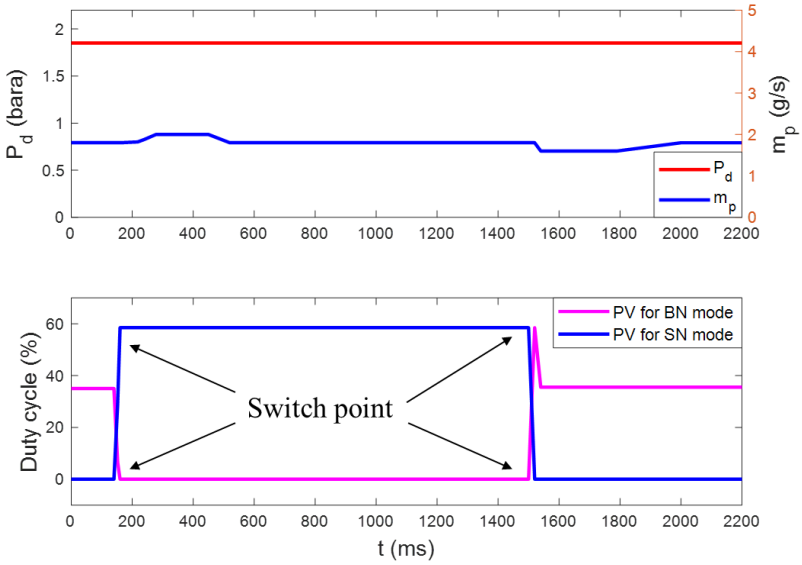

(b)

Figure 42**:** Pressure fluctuation during the transit process: (a) switching between ejector A and ejector B in the dual-ejector system; (b) switching between the BN and SN mode in the nested-nozzle ejector system

4.5 Summary

In this chapter, a nested-nozzle ejector with one BN and one SN is designed, simulated, manufactured, and tested to fully cover a large PEMFC stack output power range from a maximum of 150 kW to idle power of 13.9 kW. The entrainment capability of the nested-nozzle ejector is investigated numerically and experimentally. The BN mode is responsible for PEMFC's high power range of 150 – 38 kW (2.52 – 0.51 g/s), and the SN nested in the big nozzle chamber is used for the PEMFC's low power range of 49 – 13.9 kW (0.71 – 0.17g/s). The power overlap (49 – 39 kW) between SN and BN is designed considering the output power deviation resulting from PEMFC degradation after a long run. A bypass is integrated into the HSRS and collaborated with the nested-nozzle ejector design to optimize the D_{BN}, which increased the BN effective working range from 150 – 49 kW to 150 – 38 kW.

Considering the practical application of the PEMFC propulsion system in automotive vehicles, the ejector is manufactured by wiring cutting with stainless steel to provide high strength and geometric precision. In addition, the integrated nested-nozzle ejector assembly is developed to further reduce the size and weight of the HSRS with the proportional valves, cut-off valve, and pressure and temperature sensor.

The CFD simulation and experiment results have shown good consistency for both BN and SN regarding to the air entrainment ratio with MAPE of 5.51% and 10.28%, respectively. The dual-ejector system is compared with the nested-nozzle ejector in terms of the system power working range and the anode inlet pressure fluctuation. Both the dual-ejector and the nested-nozzle ejector system can satisfy the SR_{H_2} over the PEMFC stack's full power range. However, the tested results on anode inlet pressure during switching between two channels show that the pressure fluctuation using the nested-nozzle ejector can be negligible while the optimal controlled dual-ejector results in a maximum 44 kPa pressure difference.

Chapter 5 Machine Learning Modelling and Optimization of Ejector Design

In this chapter, an ejector performance prediction model using the data-driven machine learning (ML) method is developed to achieve two goals: (1) accurately predict the ejector H_2 entrainment performance, and (2) optimal design of ejector geometric parameters for new PEMFC stack applications. Previously, 1-D ejector analytic models required intensive experiments or simulations to determine the flow energy loss coefficients to calculate ejector flow properties and performance. Besides, building 3D flow geometric structures and analyzing the flow fields through CFD simulations are also demanding and time-consuming processes. The machine learning model is established by taking advantage of massive data from the CFD simulation to shorten the demanding design process and improve design efficiency.

The process of ejector performance prediction and design optimization is illustrated in Figure 43. Raw data is collected from ejector CFD simulation results on different PEMFC stacks. A feature-based approach is used to build the linear regression model of ejector entrainment performance. Here, features are generated and transformed based on domain knowledge from the raw data. The ordinary least-square estimator is adopted to find the optimal weight of the linear model. Based on the developed ML model, ejector geometric parameters can be optimized by solving a formulated linear programming problem. Moreover, the optimally designed ejector performance predicted by the machine learning model is verified by CFD simulation results.

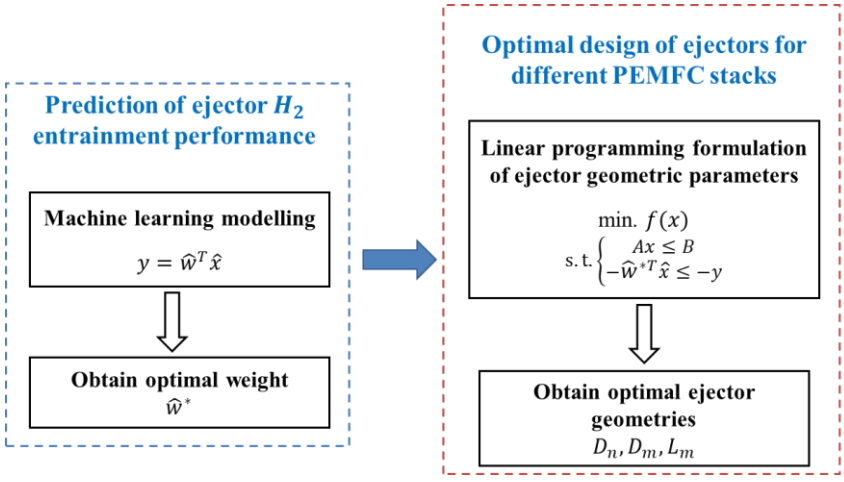

Figure 43: Process of ejector performance predication model design and geometries optimization

5.1 Machine Learning Modelling of Ejector Performance

The linear least-square model is built to present the ejector's H_2 gas entrainment performance. The model development includes the following steps: data preparation, feature engineering, model building and training, and predicted model evaluation.

5.1.1 Data Preparation

CFD simulation data is collected as input to build the ML model based on the previous ejector design projects of 20 different PEMFC stacks. The designed ejectors have their optimized geometric dimensions and unique operating conditions based on the varying stack specifications. The stacks have a wide power range from 6.5 to 200 kW and apply to different scenarios, such as drones, forklifts, passenger cars, buses, and mining trucks. The numbers of the PEMFC stack are listed with various power ranges in Figure 44.

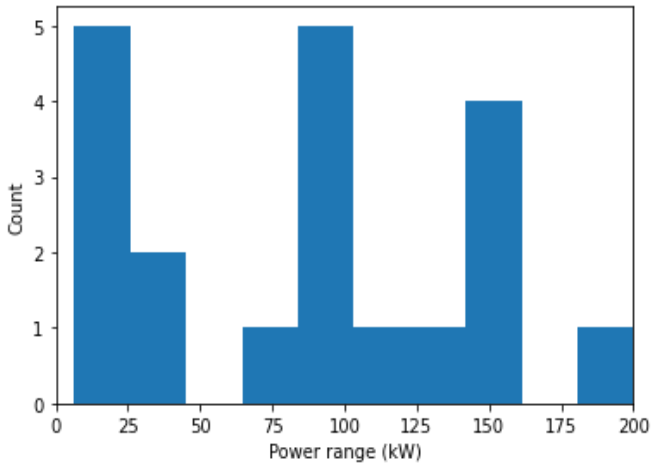

Figure 44: Numbers of PEMFC stack of a different power range

The data set of CFD simulation results is characterized by a column vector x_i, which contains important features, including PEMFC operating conditions and ejector geometric parameters, associated with a scalar ground truth y_i representing the corresponding ejector H_2 entrainment performance λ_{H_2}. In total, fifteen features are collected for each design point, including six geometric parameters: $D_n, D_m, NXP, L_m, L_d, \alpha_d$; and nine operating conditions which define the boundary conditions of the ejector's primary inlet, secondary inlet, and discharge outlet: $\dot{m}_p, P_p, T_p, P_s, T_s, P_d, T_d, \phi_s, V_{s,N_2}$. The ejector H_2 entrainment performance is determined by the above 15 features through CFD simulations. For each PEMFC stack, at least 25 to 40 simulation points are collected during the ejector optimal

design process. Therefore, the raw dataset can be presented in the form $\{(x_i, y_i), i = 1,2,\dots,M\}$ with $x_i \in R^{15\times1}, y_i \in R$, and $M = 692$.

The data cleaning process has been applied to the raw dataset to remove irrelevant or improper data. According to the ejector working principle, when the primary H_2 flow at the nozzle exit is below the speed of sound, there is not enough pressure potential energy to absorb the unused H_2 mixture from the anode outlet to satisfy the required SR_{H_2}. Therefore, the data chosen from CFD simulation results must satisfy the following condition: primary hydrogen flow at the nozzle exit should be choked. Hence, the raw dataset has been cleaned with the form $\{(x_i, y_i), i = 1,2,\dots,M\}$ where $x_i \in R^{15\times1}, y_i \in R$, and $M = 362$.

The above dataset is randomly split into two groups, where 80% of the data is selected for the training dataset, and 20% is regarded as the testing dataset.

5.1.2 Feature Engineering

Feature engineering is necessary to improve ML modelling efficiency and accuracy by extracting key features from the raw data [46]. Based on the thorough analysis and understanding of ejector working principles, the original 15 features are carefully discussed and compared using domain knowledge to identify the most important ones.

- the primary inlet pressure P_p and discharged pressure P_d are the principal factors determining the velocity and pressure of gas flows in the ejector;
- the secondary inlet pressure P_s is also important since a slight change in anode pressure drop between P_d and P_s can result in a large deviation in ejector performance;
- the relative humidity of the secondary inlet mixture ϕ_s is regarded as 100% for most cases, hence, can be neglected;
- the N_2 volumetric ratio in the secondary mixture V_{s,N_2} can affect the ejector H_2 entrainment performance due to its larger molar weight, therefore, must be considered;
- the secondary inlet temperature T_s determines the water vapour mass fraction in the anode outlet mixture, which can greatly affect the H_2 content in the entrained mixture and the overall entrainment performance;
- D_n directly decides P_p at given primary mass flow rate;

- D_m and L_m affects the primary and secondary flows mixing process;
- other geometric parameters: NXP, diffuser chamber length L_d and its divergent angle α_d, as discussed in previous chapters, can be ignored.

Consequently, eight features are selected as inputs to build the ML model, which can be expressed as:

$$x_i=\left[D_n\ D_m\ L_m\ P_p\ P_d\ P_s\ T_s\ \ V_{s,N_2}\right]^T \tag{5.1}$$

5.1.3 ML Model Building

The supervised machine learning model is built using a linear regression model to predict the ejector H_2 entrainment performance λ_{H_2}, which is expressed as:

$$\tilde{y} = \hat{w}^T\hat{x} \tag{5.2}$$

where $\tilde{y} \in R$ is the predicted ejector H_2 entrainment performance, $\hat{w} \in R^{m\times 1}$ is the wight vector of a linear model, and $\hat{x} = \begin{bmatrix} x_i \\ 1 \end{bmatrix} \in R^{m\times 1}$ is the feature vector. In this case, $m = 9$.

The difference between the predicted $\tilde{y}$ and the ground truth y_n is served to evaluate the quality of the model. In the linear model, the average loss over the entire training data set is given by:

$$e(\hat{w}) = \frac{1}{N}\sum_{n=1}^{N}(\hat{w}^T\hat{x} - y_n)^2 \tag{5.3}$$

where y_n is one ground truth sample from the training data set, and N is the total sample numbers of the training data set. In this study, N is equal to 290.

The training dataset $\hat{X}_{tr}$ is used to find the optimal weight $\hat{w}^*$ by minimizing the average loss function $e(\hat{w})$. According to the second-order sufficient conditions of an unconstrained minimum, the optimal weight $\hat{w}^*$ is calculated as:

$$\hat{w}^* = \left(\hat{X}_{tr}\hat{X}_{tr}^T\right)^{-1}\hat{X}_{tr}y_{tr} \tag{5.4}$$

where $\hat{X}_{tr} = \begin{bmatrix} x_1 x_2 \cdots x_N \\ 1\ 1 \cdots 1 \end{bmatrix}_{m\times N}$, and $y_{tr} \in R^{N\times 1}$ is the ground truth from the training dataset.

5.1.4 Model Evaluation

After getting the optimal weight $\hat{w}^*$, two metrics: the root mean squared error (RMSE) and mean absolute percentage error (MAPE) are applied to evaluate the linear regression model performance on both the training and testing data set.

$$RMSE = \left[\frac{1}{n}\sum_{i=1}^{n}(\tilde{y}_i - y_i)^2\right]^{1/2} \tag{5.5}$$

$$MAPE = \frac{1}{n}\sum_{i=1}^{n}\frac{|\tilde{y}_i - y_i|}{y_i} \times 100 \tag{5.6}$$

where y_i is the ground truth, $\tilde{y}_i$ is the predicted ejector H_2 entrainment ratio, and n is the total sample numbers of the training or testing data set. For testing dataset, the test sample is $\hat{X}_{te} = \begin{bmatrix} x_{291}x_{292}\cdots x_{M-N} \\ 1 \quad 1 \quad \cdots \quad 1 \end{bmatrix}_{m\times(M-N)}$, and $y_{te} \in R^{(M-N)\times 1}$ is its ground truth.

The predicted λ_{H_2} is compared with the ground truth from both training and testing datasets, as shown in Figure 45. Again, the results are clustered near the diagonal with sparsely distributed scatter points.

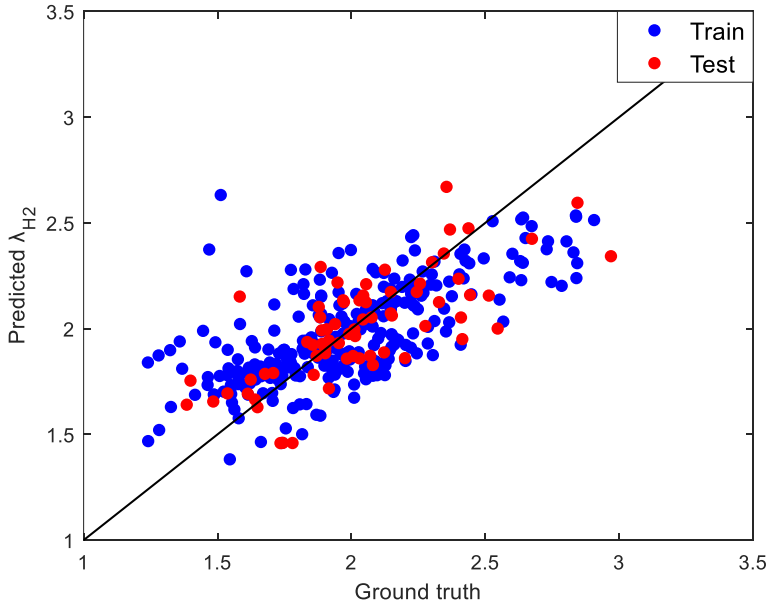

Figure 45: Comparison of ground truth and model predicted λ_{H_2}

The evaluation metrics MAPE and RMSE for both training and testing datasets are listed in Table 5. The smaller the MAPE and RMSE, the better the prediction results. The ML

model results in approximately 9.7% MAPE and 0.2422 RMSE on the training data set and 8.0% MAPE and 0.2167 RMSE on the testing data set, respectively. Since the average percentage error on the entire data set is below 10%, the optimal weight $\hat{w}^*$ can be regarded as qualified.

Table 5: Model metrics for the results in Figure 45

	RMSE	MAPE (%)
Training data	0.2422	9.72 %
Testing data	0.2167	8.08 %

5.1.5 Ejector Performance Prediction Model

The ML ejector performance prediction model can be applied to different types of ejector designs, including the conventional single-nozzle ejector and multi-nozzle ejector. The newly designed nested-nozzle ejector structure differs from the traditional single-nozzle ejector. When using the BN mode, the nested-nozzle ejector performance is identical to the performance of a conventional single-nozzle ejector. However, due to primary flow energy loss inside the large nozzle chamber when using the SN mode, the nested-nozzle ejector performance using the small nozzle is worse than the conventional ejector performance. Hence, the predication model applying an energy loss coefficient φ_{et}, is given by:

$$y_{\lambda_{H_2}} = \varphi_{et}\hat{w}^{*T}\hat{x} \tag{5.7}$$

where φ_{et} is primary flow energy loss coefficient with 1 for the conventional single nozzle ejector and BN mode of nested-nozzle ejector, and 0.75 to 0.85 for SN mode of nested-nozzle ejector which is obtained from CFD simulation results.

The developed ML model can provide accurate ejector entrainment performance prediction for any ejectors at fixed dimensions and defined operating conditions. It has a wide application for future ejector designs since the raw dataset is collected from 6.5 to 200 kW PEMFC stacks which covers most applications in market. For large PEMFC stacks over 200 kW, the stack usually consists of two or more small stacks connected in series; each small stack may have an independent HSRS.

5.2 Optimal Design of Ejector Geometries Using ML Model

The developed ejector performance prediction model can be applied for the optimal design of ejector geometric parameters to satisfy specific SR_{H_2}, under given stack operating conditions. A linear programming (LP) problem is formulated based on a thorough understanding of ejector working principles and the ML model. The obtained optimal ejector geometric results are further validated using CFD simulations.

5.2.1 Ejector Geometric Parameters Optimization

The previous optimal design of ejector geometry is through a trial-and-error method using CFD simulations, which is demanding and time-consuming. With the developed ML model, the two most important geometric parameters D_m and L_m can be obtained by solving the formulated optimization problem.

As mentioned in Chapter 3, a small D_m is beneficial to the λ_{H_2} during low power load conditions. For high power load conditions, a large D_m can provide a high λ_{H_2}. Due to the low SR_{H_2} and high-pressure potential energy during the high-power load, a relatively small D_m can still satisfy the required SR_{H_2} while maintaining a compact ejector design. Overall, a small D_m is more desirable for the ejector design.

The ratio of D_m/D_n and L_m/D_m are limited in a certain range to provide a better entrainment performance, as discussed in Chapter 3. Moreover, the ejector nozzle diameter D_n is determined in advance by the flow choking phenomenon equation considering the proportional valve's pressure and mass flowrate limitations. Hence, the optimization of ejector geometries can be formulated as an LP problem by minimizing the mixing chamber diameter D_m, subjecting to several constraints.

$$minimize\ D_m$$

$subject\ to$:

$$m_p = C_d \frac{\pi D_n^2 P_p}{4\sqrt{T_P}} \sqrt{\frac{\gamma}{R_g}\left(\frac{2}{\gamma+1}\right)^{\frac{\gamma+1}{\gamma-1}}} \tag{5.8}$$

$$3.5 \le \frac{D_m}{D_n} \le 5$$

$$3 \leq \frac{L_m}{D_m} \leq 6$$

$$-\varphi_{et} \widehat{w}^{*T} \hat{x} \leq -y$$

where the first three constraints in the optimization problem indicate the geometric limitations for D_n, D_m, and L_m; and the last constraint adopts the developed performance prediction model to make sure the optimized ejector performance can satisfy required H_2 stoichiometric ratio.

Constrained linear programming is a convex problem; thus, it can be solved using the CVX toolbox. CVX is a MATLAB-based modelling system for constructing and solving convex optimization problems, including linear and quadratic programs [47] and has been widely applied.

5.2.2 Model Validation

The proposed optimal design method using the developed ML model is applied to obtain the ejector geometric parameters for a new PEMFC with maximum 150 kW output power. In this section, two different ejector structures adopting, (1) the nested-nozzle ejector and (2) two conventional ejectors are designed and validated using CFD simulation to evaluate the modelling and optimization process. The stack anode operating conditions are presented in Table 6. As stated in Chapter 3, the ejector nozzle diameter D_n, the primary inlet pressure and P_p, and the primary inlet mass flow rate are governed by flow choking mode. The diameters D_n for BN and SN in the nested-nozzle ejector, as well as for the big ejector and small ejector in the dual-ejector system, are designed following the process discussed in Chapter 4. The nozzle diameter D_n of the BN in nested-nozzle ejector and large ejector of dual-ejector is determined as 2.10 mm, while the nozzle diameter of the small nozzle of nested-nozzle ejector and small ejector is 1.2 mm. The ejector's primary pressure P_p at different PEMFC operating power is calculated according to Equation (3.8). The SN mode in the nested-nozzle ejector operates in the low mass flow rate (or low power) conditions, the same as the small ejector in the dual-ejector system. In contrast, the BN mode operates in the high mass flow rate (or high power) conditions as the large ejector in the dual-ejector system.

Table 6: The 150kW PEMFC stack anode operating conditions

	$\dot{m}_p$ (g/s)	P_p (bara)	$P_{an,in}$ (bara)	$P_{an,out}$ (bara)	$T_{an,out}$ (K)	$\emptyset_{an,out}$ (%)	V_{s,N_2} (%)	SR_{H_2}
SN Mode	0.2952	4.27	1.4	1.385	339.15	100%	2%	2.3
	0.4387	6.4	1.55	1.534	341.15	100%	2%	2
	0.585	8.54	1.75	1.727	343.15	100%	2%	1.9
	0.7313	10.67	2.05	2.028	345.15	100%	2%	1.8
	0.8843	12.81	2.46	2.379	347.15	100%	2%	1.8
BN Mode	0.8843	4.23	2.46	2.379	347.15	100%	2%	1.8
	1.217	5.83	2.67	2.567	350.15	100%	2%	1.8
	1.5482	7.41	2.7	2.573	353.15	100%	2%	1.8
	1.8795	9	2.7	2.556	356.15	100%	2%	1.6
	2.2122	10.59	2.7	2.53	359.15	100%	2%	1.6
	2.5434	12.17	2.7	2.51	362.15	100%	2%	1.6

To perform the optimal design process, the input $\hat{x}$ and ground truth y of the ML model are expressed below for both structures: the conventional two ejectors in the dual-ejector system and the nested-nozzle ejector. For small ejector in the dual-ejector system or the SN mode in the nested-nozzle ejector:

$$\hat{x} = \begin{bmatrix} 1.20 & 1.20 & 1.20 & 1.20 & 1.20 \\ D_m & D_m & D_m & D_m & D_m \\ L_m & L_m & L_m & L_m & L_m \\ 4.27 & 6.4 & 8.54 & 10.67 & 12.81 \\ 1.4 & 1.55 & 1.75 & 2.05 & 2.46 \\ 1.385 & 1.534 & 1.727 & 2.028 & 2.379 \\ 339.15 & 341.15 & 343.15 & 345.15 & 347.15 \\ 0.02 & 0.02 & 0.02 & 0.02 & 0.02 \\ 1 & 1 & 1 & 1 & 1 \end{bmatrix} \tag{5.9}$$

$$y = [2.3 \quad 2 \quad 1.9 \quad 1.8 \quad 1.8]$$

For the large ejector in a dual-ejector system or the BN mode in the nested-nozzle ejector:

$$\hat{x} = \begin{bmatrix} 2.10 & 2.10 & 2.10 & 2.10 & 2.10 & 2.10 \\ D_m & D_m & D_m & D_m & D_m & D_m \\ L_m & L_m & L_m & L_m & L_m & L_m \\ 4.23 & 5.83 & 7.41 & 9 & 10.59 & 12.17 \\ 2.46 & 2.67 & 2.70 & 2.70 & 2.70 & 2.70 \\ 2.379 & 2.567 & 2.573 & 2.556 & 2.53 & 2.51 \\ 347.15 & 350.15 & 353.15 & 356.15 & 359.15 & 362.15 \\ 0.02 & 0.02 & 0.02 & 0.02 & 0.02 & 0.02 \\ 1 & 1 & 1 & 1 & 1 & 1 \end{bmatrix} \tag{5.10}$$

$$y = [1.8 \quad 1.8 \quad 1.8 \quad 1.6 \quad 1.6 \quad 1.6]$$

The optimized ejector geometries for both conventional ejectors and nested-nozzle ejector are obtained by solving the constrained linear programming optimization method using the tool 'CVX' in MATLAB environment. The final results are presented below in Table 7.

Table 7: Optimized ejector geometries using LP optimization method

Structure	**Dual ejector**		**Nested-nozzle ejector**	
	Large ejector	Small ejector	Large nozzle (BN)	Small nozzle (SN)
D_n (mm)	2.1	1.2	2.1	1.2
D_m (mm)	8	5.8	8	8
L_m (mm)	40	35	40	40

The optimally designed ejectors through the ML model and LP process are validated using CFD simulations. The ejector 3D model with optimized geometries is built using Simens NX12, and the CFD simulations are carried out using ANSYS Fluent to get the ejector H_2 entrainment capability. The H_2 entrainment performance λ_{H_2} for the large ejector and the BN mode of the nested-nozzle ejector are the same since they have the same optimized geometric parameters. The λ_{H_2} values obtained using CFD and LP methods of the large ejector or BN mode are presented in Figure 46(a), where the relative error is below 8 %, and MAPE is around 6.7 %. For the small ejector, the relative error is below 7 %, and MAPE is below 5 %, as shown in Figure 46(b). The comparisons of λ_{H_2} for the SN mode of nested-nozzle ejector are shown in Figure 46(c) with a relative error of 7 % and MAPE of 3.46 %. The validation results of the optimized ejector design using the developed ML model and LP method have shown high consistencies with the CFD simulation results. This method can provide accurate ejector geometries optimization and, thus, simplify the ejector design process with reduced computational time and accurate results.

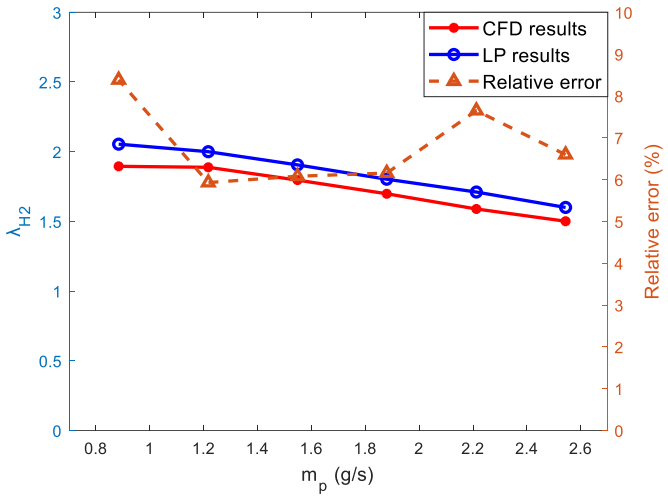

(a)

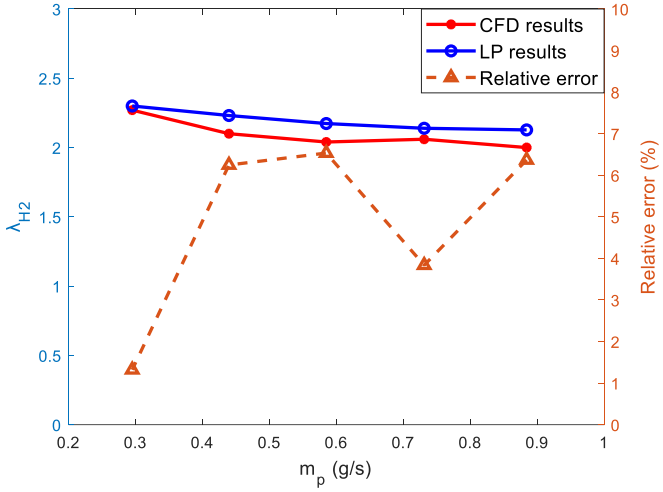

(b)

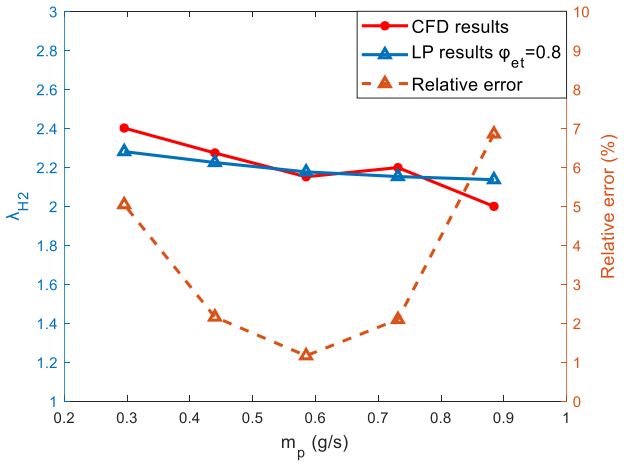

(c)

Figure 46: λ_{H_2} comparison between CFD and LP method results of (a) large ejector or BN mode (b) small ejector, (c) SN mode of nested-nozzle ejector

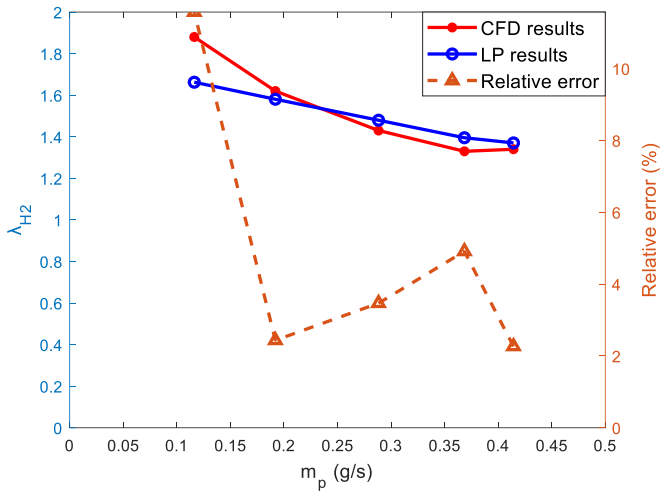

(a)

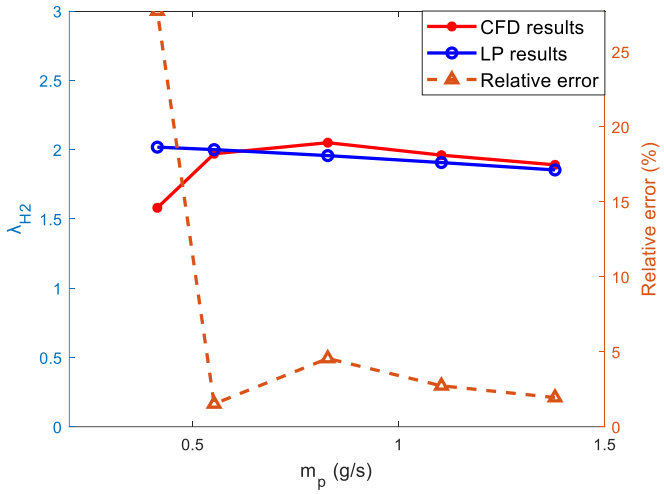

(b)

Figure 47: λ_{H_2} comparison between CFD and LP method results of a single ejector (a) for 24 kW PEMFC stack (b) for 84 kW PEMFC stack

To further validate the robustness of the LP optimization method, two new PEMFC stacks with a maximum output power of 24 kW and 84 kW are adopted. The ejectors for both stacks are optimized using LP and compared to CFD simulation results. The MAPE of ejectors is 4.93 % for 24 kW PEMFC stack and 7.69 % for 84 kW PEMFC stack, respectively, shown in Figure 47. Together with the previously discussed 150 kW stack results, the applied LP method can accurately predict the system performance for small, medium, and large-sized PEMFC stacks. However, the accuracy of LP results largely depends on the accuracy of the ejector performance machine learning model, and the

sample size in the dataset determines the accuracy of the ejector performance model. Due to the small size of samples in the dataset, the ejector performance model can not guarantee accurate performance predictions for each PEMFC stack. Hence, in the future, more data will be collected from CFD simulation or test results to improve the accuracy and robustness of this LP optimization method.

Through this optimization design approach using machine learning model, the ejector design process can be significantly simplified. The conventional design process relying on traditional CFD simulation method requires at least 800 minutes to design an appropriate ejector for each PEMFC stack using parallel processing on ANSYS Fluent software (Intel Core i5-11400 processor, 2.6GHz, 6 cores, 12 logical processors, 32GB RAM), while LP optimization using machine learning model takes about 0.79 s for an ejector design. The computational time of ejector design is greatly reduced.

5.3 Summary

The machine learning model for ejector H_2 entrainment performance prediction is built using a data-driven method from CFD simulation results. The linear regression model can provide accurate prediction results with a relative error below 10 % compared to the CFD results.

Moreover, a linear programming optimization problem is established to find the optimal ejector geometric parameters for conventional ejectors and newly designed nested-nozzle ejectors. The CFD simulations of H_2 entrainment performance with the optimized ejector geometries for a large-size PEMFC stack with 150 kW is compared with the ML results. It demonstrates good consistency with relative error within 8 % and MAPE below 7 %. For mid-size and small-size PEMFC stacks (84 kW and 24 kW, respectively), the MAPE of H_2 entrainment performance between the CFD simulation and LP optimization results is also within 8 %.

Chapter 6 Modelling and Control of HSRS

In this chapter, key components in HSRS are modelled in MATLAB/Simulink environment to investigate the system performance. The control strategy for ejector-based HSRS is also developed. The controllers and HSRS component models are further integrated with the PEMFC stack model and the cathode air supply system model developed in [7] to compose a closed-loop simulation of a PEMFC system. Finally, the control strategies and system performance are demonstrated by applying a 150kW PEMFC system.

6.1 HSRS Auxiliary Components Model

The HSRS auxiliary components model consists of five interacting sub-models: H_2 storage tank, pressure regulator, H_2 proportional valve, H_2 ejector, and stack anode mass balance. Several assumptions are applied in the model. First, all the gases in HSRS, including H_2, water vapour, and N_2, are regarded as single-phase ideal gas. Secondly, the temperature change of hydrogen flow before the hydrogen ejector is assumed at a constant 293.15 K. The stack anode outlet temperature is maintained at 353.15 K. Thirdly, we assume that there is no pressure and temperature drop between the stack anode outlet and ejector secondary inlet. Hence, the ejector secondary inlet conditions, such as the species, temperature, pressure, and relative temperature, are equal to the anode outlet conditions. The mixture's relative humidity is regarded as 100%, and the volumetric ratio of crossover N_2 is maintained at 2%.

6.1.1 Hydrogen Storage Tank Model

The compressed gaseous hydrogen (CGH2) storage tank model calculates the remaining mass and pressure of H_2 during the discharge process. The initial conditions of the hydrogen storage tank, shown in Figure 48, consist of tank pressure $P_{st,ini}$, internal volume V_{st}, H_2 mass $m_{st,ini}$ and temperature $T_{st,ini}$. The states are H_2 mass m_{st} inside the tank and H_2 mass flow $\dot{m}_{st,out}$ discharged.

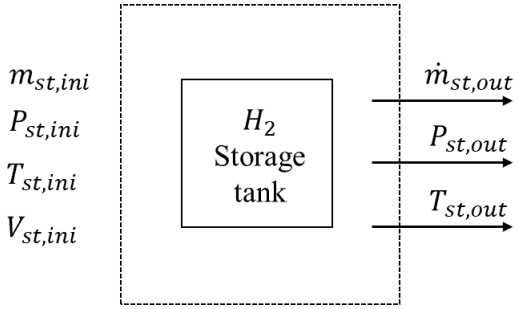

Figure 48: H_2 storage tank block diagram

$$m_{st} = m_{st,ini} - m_{st,out} \tag{6.1}$$

$$\frac{dm_{st}}{dt} = -\dot{m}_{st,out} = \begin{cases} -(\dot{m}_{pv1,out} + \dot{m}_{pv3,out}) & BN\ mode \\ -(\dot{m}_{pv2,out} + \dot{m}_{pv3,out}) & SN\ mode \end{cases} \tag{6.2}$$

where $\dot{m}_{pv1,out}$ is the H_2 mass flow rate consumed by PV1 in BN mode adopting the large nozzle of nested-nozzle ejector or the large ejector of multi-ejectors or single nozzle ejector; $\dot{m}_{pv2,out}$ is the H_2 mass flow rate consumed by PV2 in SN mode of nested-nozzle ejector or small ejector of multi-ejectors; $\dot{m}_{pv3,out}$ is the H_2 mass flow rate consumed by PV3 in Bypass.

The density of CGH2 inside the storage tank ρ_{CGH2} can be calculated as follow:

$$\rho_{CGH2} = \frac{m_{st}}{V_{st}} \tag{6.3}$$

To reflect internal conditions of H_2 storage tank, the density of real H_2 instead of an ideal gas is applied. Figure 49 presents the real gas density of CGH2. When the storage tank's internal pressure is 70 or 35 MPa, the real H_2 density is around 37 or 23 kg/m^3, respectively, which is approximately 64.9% and 79.4% of the corresponding ideal H_2 gas density. To describe the relationship between CGH2 pressure and density, a polynomial function is given below. And the regression coefficients obtained by curve fitting are given in Table 8.

$$P_{st,out} = a_1 {\rho_{CGH2}}^2 + a_2 \rho_{CGH2} + a_3 \tag{6.4}$$

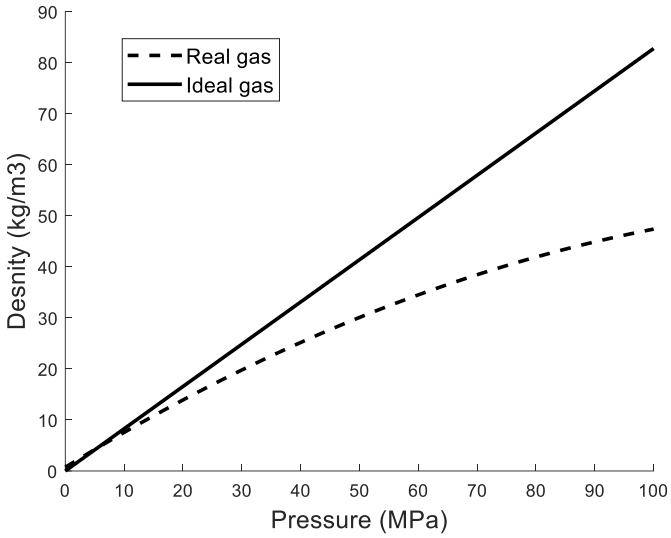

Figure 49: CGH2 density at different pressure

Table 8: CGH2 density regression coefficients

Parameter	Value
a_1	0.02237
a_2	1.029
a_3	-0.1967

6.1.2 Hydrogen Pressure Regulator Model

Due to the HSRS safety consideration and the pressure limitation of the proportional valve downstream, a gas pressure-reducing valve lowers the high pressure of CGH2 in the storage tank from 35 or 70 MPa to the pre-set relatively low pressure, usually no more than 1.6 MPa by adjusting its throttle area. A two-stage high-pressure reducing valve with maximal inlet pressure 35 MPa is adopted in this model. The model applies a static reducing valve map to determine the outlet pressure, as shown in Figure 50.

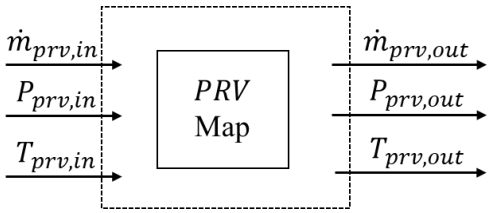

Figure 50: Pressure-reducing valve block diagram

The inputs to the model consist of an inlet H_2 mass flow rate $\dot{m}_{prv,in}$ and inlet pressure $P_{prv,in}$, which is assumed to equal the internal pressure of H_2 storage tank $P_{st,out}$. The

thermodynamic change of the valve is not considered; hence its outlet temperature $T_{prv,out}$ is assumed identical to the inlet temperature $T_{prv,in}$, which is fixed at 293.15 K. The H_2 mass flow rate $\dot{m}_{prv,in}$ is equal to the fuel consumption required by PEMFC system operation conditions. The outlet pressure $P_{prv,out}$ is determined through the pressure-reducing valve map from the inlet mass flow rate and inlet pressure. The characteristic data of the valve is obtained from the valve map in [48] and plotted using black dotted lines in Figure 51. A polynomial function is generated using the curve fitting method to model the characteristics of valve pressure and mass flow rate.

$$z = a_{00} + a_{10}x + a_{01}y + \cdots + a_{14}xy^4 + a_{05}y^5 \tag{6.5}$$

where x, y and z represent normalized H_2 volumetric flow rate by mean 1550 and std 724.8, normalized inlet pressure by mean 155.3 and std 116.6 and outlet pressure $P_{prv,out}$ (bara) respectively. $a_{i,j}$ are the regression coefficients.

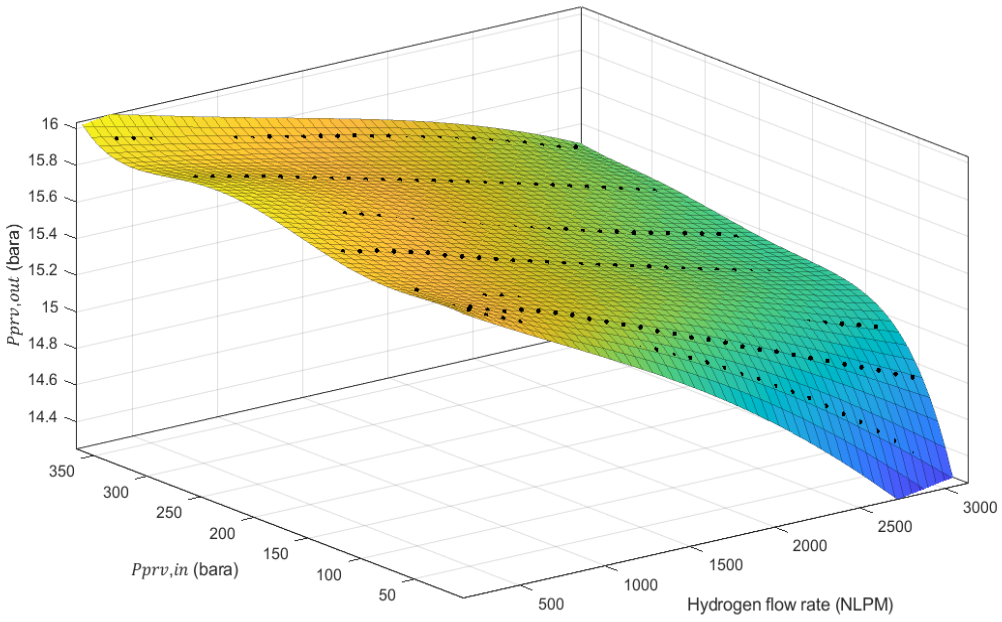

Figure 51: Characteristic map of a pressure-reducing valve

The generated pressure-reducing valve map using the polynomial function is also demonstrated in Figure 51, which shows good consistency with the original data (black dotted lines). The regression coefficients in the above polynomial equation obtained by curve fitting are shown in Table 9.

Table 9: Regression coefficients of pressure-reducing valve map

a_{00}	15.49	a_{11}	-0.03778	a_{23}	0.01119
a_{01}	0.1556	a_{12}	0.02577	a_{30}	0.004031
a_{02}	0.08358	a_{13}	0.08003	a_{31}	0.002005
a_{03}	-0.06811	a_{14}	-0.04127	a_{32}	-0.0066
a_{04}	-0.09203	a_{20}	0.01513	a_{40}	-0.002147
a_{05}	0.05751	a_{21}	-0.009558	a_{41}	0.0009007
a_{10}	-0.2003	a_{22}	-0.02118	a_{50}	0.0009309

6.1.3 Hydrogen Proportional Valve Model

The anode H_2 gas pressure and mass flow rate control rely on accurate gas injection from a high-pressure tank. The mainstream of high-pressure H_2 from the HSRS's injection system usually adopts electronically controlled devices, such as H_2 injectors or proportional valves. They are crucial in ensuring fuel mass and pressure supply to the anode side. Both H_2 injectors and proportional valves rely on the electric current to generate magnetic forces to open and close the valve by lifting the plunger against the spring force and letting the gas flow. Advanced proportional control solenoid valves can precisely change the intensity of the coil current or the magnetic power to influence the valve's opening degree. As a result, the flow rate can be freely controlled in proportion to the control signal. The control signal is usually converted into a pulse-width modulation (PWM) signal to eliminate hysteresis effects to prevent the static friction generated during the plunger's movement. By adjusting the PWM frequency and duty cycle, the variable coil current can control the flow rate precisely in a proportional solenoid valve.

A proportional control solenoid valve is chosen in this study for the H_2 supply system since it can operate at a higher pressure and sustain a wide range of inlet/outlet pressure differences. The proportional valve's orifice design is essential for the continuous and smooth control of the variable flow rate. The most important parameters for selecting a correct solenoid valve are the flow coefficient (the k_v value in m^3/h), the maximum operating pressure range (i.e., the pressure before and after the valve $P_{pv,in}$ and $P_{pv,out}$), and the requested maximum flow rate. This study takes k_v values measured with the water's flow rate at 293.15 K and 1 bar relative pressure at the valve inlet, compared with

0 bar at the valve outlet. For gases, the standard flow rate Q_N is calculated depending on the low and high flow pressure drops through the valve orifice.

The flow characteristics could change if the differential pressure between the inlet and outlet pressure exceeded half the inlet pressure value. Specifically, the calculation of the standard flow rate for subcritical conditions, i.e., $\frac{P_{pv,out}}{P_{pv,in}} > \left(\frac{2}{\gamma+1}\right)^{\frac{\gamma}{\gamma-1}}$, is:

$$Q_N = 514 k_v \sqrt{\frac{P_{pv,out}(P_{pv,in} - P_{pv,out})}{T_{pv,in}\rho_N}} \tag{6.6}$$

For critical flow, where $\frac{P_{pv,out}}{P_{pv,in}} \leq \left(\frac{2}{\gamma+1}\right)^{\frac{\gamma}{\gamma-1}}$, the standard flow rate is determined by:

$$Q_N = 257 k_v P_{pv,in} \sqrt{\frac{1}{T_{pv,in}\rho_N}} \tag{6.7}$$

where Q_N and ρ_N are the standard flow rate and gas density at 0 °C and 1 atm, respectively; k_v is the flow coefficient determined by the proportional valve; $T_{pv,in}$, $P_{pv,in}$ and $P_{pv,out}$ are the inlet temperature, inlet and outlet pressure, respectively.

The characteristic curves of a proportional valve with a constant inlet pressure of 15 bara are plotted in Figure 52. The H_2 volume flow rate (Q in NLPM, or normal liter per minute) of different valve lift at temperature 293.15 K versus the pressure differences ($dP = P_{pv,in} - P_{pv,out}$) are adjustable with different k_v values. The k_v value is controlled by PWM control signal, where the position of the plunger is determined by the coil current.

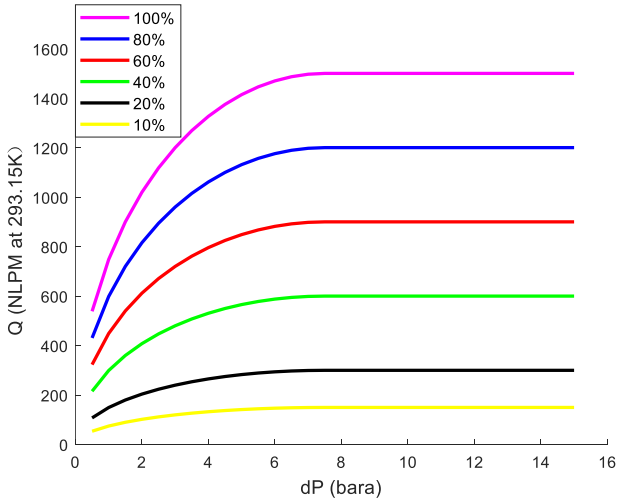

Figure 52: Hydrogen flow rate characteristics of the proportional valve

The PWM-controlled proportional valve offers a flexible range of pressure outlets at different mass flow rates. In this study, the downstream pressure could range from 15.5 to 1 bara by adjusting the duty cycle and k_v value, allowing the optimal control to achieve a variable flow rate in a wide range of operations.

The mass flow of PV can be calculated as follows:

$$\dot{m}_{pv,out} = \frac{Q_N \rho_N}{60 \times 1000} \tag{6.8}$$

In this model, three PVs are applied to satisfy different structures of HSRS, adopting single nozzle ejector, dual ejectors, and nested-nozzle ejectors with or without bypass. The HSRS structure determines which PV is activated to supply the H_2 flow, as summarized in Table 10.

Table 10: PV activation conditions on different HSRS structure designs (● activated)

HSRS structure	**PV1**	**PV2**	**PV3**
Single nozzle ejector	●		
Dual ejector	● (Large ejector)	● (Small ejector)	
Nested-nozzle ejector	● (Large nozzle)	● (Small nozzle)	
Bypass			●

The block diagram of the PV model is shown in Figure 53. This model does not consider the temperature change between the inlet and the outlet. The PV inlet pressure $P_{pv,in}$ is equal to the outlet pressure of the pressure regulator $P_{pr,out}$. PV1 and PV2 outlets are connected to the ejector primary inlets. Hence, their outlet pressure depends on the ejector nozzle diameter and the discharged mass flow rate. The PV3 outlet is directly connected to the stack anode inlet. Hence, the PVs' outlet pressure $P_{pvi,out}$ can be given as:

$$P_{pvi,out} = \begin{cases} 4\dfrac{\dot{m}_{pv,out}}{C\pi {D_n}^2}\sqrt{\dfrac{\gamma}{RT_{pv,out}}\left(\dfrac{2}{\gamma+1}\right)^{(r-1)/(r+1)}} & i = 1 \; and \; 2; \\ P_{an,in} & i = 3; \end{cases} \tag{6.9a}$$

$$\dot{m}_{pv,in} = \dot{m}_{pv1,out} + \dot{m}_{pv2,out} + \dot{m}_{pv3,out} \tag{6.9b}$$

where D_n is the ejector's nozzle diameter.

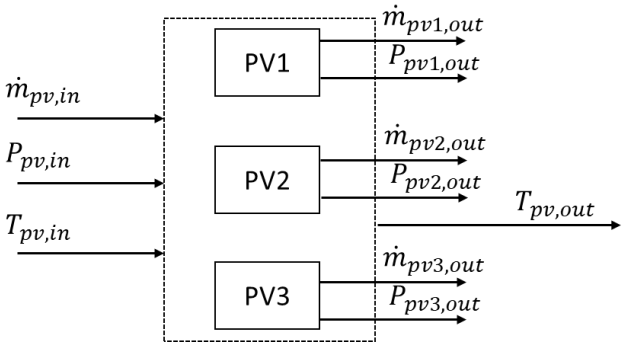

Figure 53: Proportional valve block diagram

6.1.4 Hydrogen Ejector Model

For the dual-ejector or nested-nozzle ejector system considered in this study, there are two flow channels to supply the primary H_2. It is assumed that the primary flow is 100% H_2. The primary inlet temperature is constant at an ambient temperature of 293.15 K. The pressure drop from the water separator and the flow channels between the stack anode outlet and the second inlet is negligible compared to the stack anode pressure drop. Moreover, the secondary inlet flow conditions, namely, pressure, temperature, and humidity, are considered the same as the stack anode outlet flow conditions. The species of the second inlet flow consists of the H_2, N_2, and water vapour at 100% relative humidity, and the mixture flow temperature is assumed to be equal to the stack temperature.

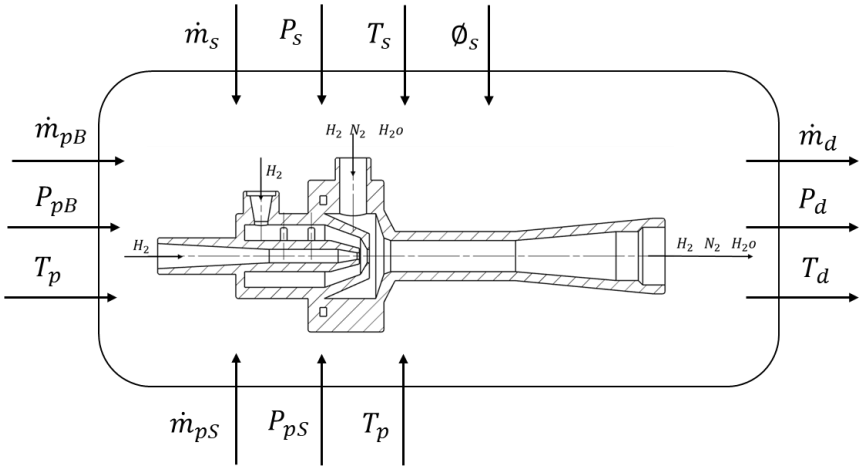

Figure 54: Nested-nozzle ejector mass flow model block diagram

Figure 54 illustrates the mass flow priorities inside the ejector. The inputs of the ejector model consist of primary mass flow $\dot{m}_{pB}$ for BN mode, and $\dot{m}_{pS}$ for SN mode, primary inlet temperature T_p, primary pressure P_{pB} and P_{pS} as well as secondary inlet mass flow

$\dot{m}_s$, pressure P_s, temperature T_s and relative humidity $\emptyset_s$. The ejector outlet pressure P_d is assumed equal to the anode inlet pressure $P_{an,in}$. The model is to determine the ejector's outlet mass flow rate $\dot{m}_d$ and outlet temperature T_d.

The mass continuity is used to balance the mass of three inlets and one outlet, as shown by the following equation.

$$\begin{gathered} \dot{m}_p + \dot{m}_s = \dot{m}_d \\ subject\ to:\ \dot{m}_p = \dot{m}_{pB} \text{ for BN mode} \\ \dot{m}_p = \dot{m}_{pS} \text{ for SN mode} \end{gathered} \tag{6.10}$$

The ejector H_2 entrainment performance $y_{\lambda_{H_2}}$ is calculated using the developed ML model in Chapter 5 according to model inputs. Generally, the optimally designed ejector H_2 entrainment performance is higher than the stack required SR_{H_2}, which means all anode outlet mixtures can be absorbed into the ejector. However, when PEMFC system power changes suddenly from high power to low power, the ejector may work in an off-design area which results in a small $y_{\lambda_{H_2}}$. In these extreme conditions, part of the anode outlet mixture is left inside the channel between the anode outlet and the secondary inlet, which the purge valve should discharge. Hence, the $\dot{m}_s$ is given by:

$$\dot{m}_s = \begin{cases} \dot{m}_{an,out} & y_{\lambda_{H_2}} > SR_{H_2} \\ \dfrac{\left(y_{\lambda_{H_2}} - 1\right)}{y_{H_2}} \dot{m}_p & y_{\lambda_{H_2}} \le SR_{H_2} \end{cases} \tag{6.11}$$

The primary inlet pressure P_{pB} and P_{pS} are determined according to the mass flow rate $\dot{m}_p$ and nozzle diameter D_{iN}:

$$P_{pi} = 4\frac{\dot{m}_p}{C\pi {D_{iN}}^2}\sqrt{\frac{\gamma}{RT_p}\left(\frac{2}{\gamma+1}\right)^{(r-1)/(r+1)}} \tag{6.12}$$

where D_{iN} is the nozzle throat diameter, and i presents the B for BN mode, and S for SN mode, respectively.

The water vapour partial pressure in the second mixture is calculated as:

$$P_{s,H_2O} = \emptyset_s P_{sat}(T_s) \tag{6.13}$$

The N_2 partial pressure is calculated by using the N_2 volumetric ratio in the secondary mixture V_{s,N_2}.

$$P_{s,N_2} = V_{s,N_2} P_s \tag{6.14}$$

The secondary inlet H_2 partial pressure is then calculated as:

$$P_{s,H_2} = P_s - P_{s,H_2o} - P_{s,N_2} \tag{6.15}$$

Then the mass flow of H_2, N_2, water vapour, and total mass flow discharged at the ejector outlet can be calculated as:

$$\dot{m}_{d,H_2} = \dot{m}_p + \dot{m}_s \frac{P_{s,H_2}}{p_s} \tag{6.16a}$$

$$\dot{m}_{d,N_2} = \dot{m}_s \frac{P_{s,N_2}}{P_s} \tag{6.16b}$$

$$\dot{m}_{d,H_2o} = \dot{m}_s \frac{P_{s,H_2o}}{P_s} \tag{6.16c}$$

$$\dot{m}_d = \dot{m}_{d,H_2o} + \dot{m}_{d,N_2} + \dot{m}_{d,H_2} \tag{6.16d}$$

The temperature of the discharged mixture T_d is calculated by the following energy balance equation [33]. In this study, flow energy loss e_{loss} is not considered, and H_2 flow at ejector inlets and outlet are assumed as stagnant, hence, the energy balance equation does not have to consider the flows' kinetic energy.

$$\dot{m}_p \left(C_{pp,H_2} T_p + \frac{{v_p}^2}{2} \right) + \dot{m}_s (C_{ps,Mix} T_s + \frac{{v_s}^2}{2}) = \dot{m}_d (C_{pd,Mix} T_d + \frac{{v_d}^2}{2}) + e_{loss} \tag{6.17}$$

where v_p, v_s, and v_d are the flow velocity at ejector primary inlet, secondary inlet, and outlet, respectively. The specific heat at a constant pressure of primary hydrogen C_{pp,H_2}, secondary mixture $C_{ps,Mix}$, and discharged outlet mixture $C_{pd,Mix}$ can be calculated according to the following equations:

$$C_{p,H_2}(T) = R_{H_2}(3.057 + 2.677e^{-3}T - 5.810e^{-6}T^2 + 5.521e^{-9}T^3 - 1.812e^{-12}T^4) \tag{6.18a}$$

$$C_{p,N_2}(T) = R_{N_2}(3.675 - 1.208e^{-3}T + 2.324\,e^{-6}T^2 - 0.632e^{-9}T^3 - 0.226e^{-12}T^4) \tag{6.18b}$$

$$C_{p,H_2o}(T) = R_{H_2o}(4.070 - 1.108e^{-3}T + 4.152e^{-6}T^2 - 2.964e^{-9}T^3 + 0.807e^{-12}T^4) \tag{6.18c}$$

$$C_{p,Mix}(T) = V_{H_2} C_{p,H_2}(T) + V_{N_2} C_{p,N_2}(T) + V_{H_2o} C_{p,H_2o}(T) \tag{6.18d}$$

where V_{H_2}, V_{N_2}, and V_{H_2o} represent the H_2, N_2, and water vapour volumetric ratio in the mixture, respectively.

6.1.5 Anode Mass Flow Model

The anode mass flow model, representing the states of working flows inside the PEMFC stack anode channel, has been studied by Jay et al. [7] without considering the anode pressure drop. Although the pressure drop resulting from flow resistance in the anode channel is small compared to the anode inlet pressure, it has a significant effect on the ejector H_2 entrainment performance. The anode pressure drop is mainly affected by the H_2 mass flow rate consumed by the fuel cell stack and the stack hydrogen stoichiometric ratio SR_{H_2} [49]. The more H_2 mass enters inside the anode flow channel, the larger the anode pressure drop is. Besides, the stack temperature also greatly influences the anode pressure drop because of the variation of H_2 mixture properties on density and viscosity.

For large PEMFC stacks at maximum output power, such as 150 kW, the anode pressure drop could be 30 kPa at rated power. A lookup table presents the anode pressure drop due to the lack of anode flow channel geometric parameters. Besides, the anode inlet mass is supplied by both the bypass channel and ejector path. The anode inlet temperature can be calculated using the ejector discharge temperature and the bypass pure H_2 flow temperature. The temperature inside the anode channel and at the anode outlet is assumed to be equal to the stack temperature T_{st}, which is acquired from stack experimental results in this model.

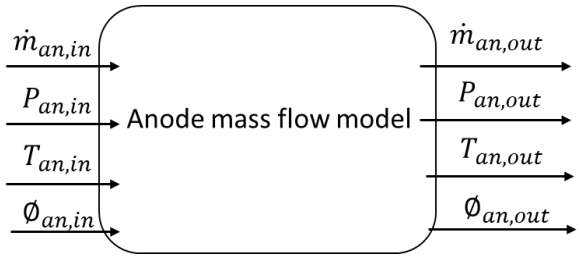

Figure 55: Anode mass flow model block diagram

Figure 55 shows the anode mass flow model. The inputs of the model consist of anode inlet mass flow $\dot{m}_{an,in}$, temperature $T_{an,in}$, pressure $P_{an,in}$, and relative humidity $\emptyset_{an,in}$. The H_2 mass m_{an,H_2},water mass m_{an,H_2O} [7] and N_2 mass m_{an,N_2} inside the anode flow channel using mass balance equations are expressed as:

$$\frac{dm_{an,H_2}}{dt} = \dot{m}_{an,in,H_2} - \dot{m}_{an,out,H_2} - \dot{m}_{an,reacted,H_2} \tag{6.19}$$

$$\dot{m}_{an,in,H_2} = \dot{m}_{d,H_2} + \dot{m}_{by,H_2} \tag{6.20}$$

$$\frac{dm_{an,H_2O}}{dt} = \dot{m}_{an,in,VH_2O} - \dot{m}_{an,out,VH_2O} - \dot{m}_{an,out,LH_2O} - \dot{m}_{mem,VH_2O} \quad (6.21)$$

$$\frac{dm_{an,N_2}}{dt} = \dot{m}_{an,in,N_2} - \dot{m}_{an,out,N_2} + \dot{m}_{mem,N_2} \quad (6.22)$$

where $\dot{m}_{an,in,H_2}$ is the total H_2 mass flow rate entering the anode; $\dot{m}_{an,out,H_2}$ is the H_2 mass flow rate leaving the anode; $\dot{m}_{an,reacted,H_2}$ is the H_2 mass flow rate consumed by the stack theoretically; $\dot{m}_{d,H_2}$ is the H_2 mass flow rate discharged by the ejector; $\dot{m}_{by,H_2}$ is the H_2 mass flow rate supplied by the bypass channel $\dot{m}_{pv3,out}$; $\dot{m}_{an,in,VH_2O}$ is the water vapour mass flow rate entering the anode $\dot{m}_{d,H_2O}$; $\dot{m}_{an,out,VH_2O}$ is the water vapour mass flow rate leaving the anode; $\dot{m}_{an,out,LH_2O}$ is the liquid water mass flow rate at the exit of the anode; $\dot{m}_{mem,VH_2O}$ is the water vapour mass flow rate passing through the membrane; $\dot{m}_{an,in,N_2}$ is the N_2 mass flow rate entering the anode; $\dot{m}_{an,out,N_2}$ is the N_2 mass flow rate leaving the anode; and $\dot{m}_{mem,N_2}$ is the N_2 mass flow rate transferring through the membrane.

The anode inlet relative humidity $\emptyset_{an,in}$ is assumed as 100%. The reason is that during the mixing process of the ejector outlet mixture at high temperature T_d and pure H_2 from bypass at a low temperature of 293.15 K, part of the water vapour condenses into liquid water. The anode inlet temperature $T_{an,in}$ can be calculated by the following energy balance equation without considering the flow of kinetic energy and energy loss during the mixing process.

$$\dot{m}_{by,H_2} C_{pp,H_2} T_p + \dot{m}_d C_{pd,Mix} T_d = (\dot{m}_d + \dot{m}_{by,H_2}) C_{pan,Mix} T_{an,in} \quad (6.23)$$

The H_2 mass, water vapour mass and N_2 mass acquired above are used to calculate the H_2 partial pressure P_{an,H_2}, water vapour partial pressure P_{an,H_2O} and N_2 partial pressure P_{an,N_2} using the ideal gas law. The anode channel temperature is assumed to be the stack reaction temperature T_{st} instead of $T_{an,in}$.

$$P_{an,H_2} = \frac{m_{an,H_2} R_{H_2} T_{st}}{V_{an}} \quad (6.24)$$

$$P_{an,VH_2O} = \frac{m_{an,H_2O} R_{H_2O} T_{st}}{V_{an}} \quad (6.25)$$

$$P_{an,N_2} = \frac{m_{an,H_2O} R_{H_2O} T_{st}}{V_{an}} \quad (6.26)$$

The anode inlet pressure $P_{an,in}$ is assumed to be equal to the internal pressure of the anode channel P_{an} given by:

$$P_{an} = P_{an,H_2} + P_{an,VH_2O} + P_{an,N_2} \tag{6.27}$$

$$P_{an,in} = P_{an} \tag{6.28}$$

The relative humidity of H_2 mixture inside the anode channel $\emptyset_{an}$ can be calculated as:

$$\emptyset_{an} = \frac{P_{an,VH_2O}}{P_{sat}(T_{st})} \tag{6.29}$$

The stack anode pressure drop dP_{an} is acquired from experimental results of a PEMFC stack with 150 kW. A lookup table with the input of anode inlet pressure $P_{an,in}$ is built to get the anode outlet pressure $P_{an,out}$.

$$P_{an,out} = P_{an,in} - dP_{an} \tag{6.30}$$

The anode outlet mixture usually contains liquid water, hence the relative humidity of the anode outlet mixture $\emptyset_{an,out}$ is assumed as 100%. The water vapour partial pressure at the anode outlet P_{an,out,VH_2O} can be expressed as:

$$P_{an,out,VH_2O} = \emptyset_{an,out} P_{sat}(T_{st}) \tag{6.31}$$

The anode outlet mixture goes through the water separator to remove the liquid water before entering the ejector. Hence the anode outlet mixture is assumed to include the H_2, N_2, and water vapour. The anode outlet mixture mass flow is given by:

$$\dot{m}_{an,out} = \dot{m}_{an,out,H_2} + \dot{m}_{an,out,VH_2O} + \dot{m}_{an,out,N_2} \tag{6.32}$$

The volumetric ratio of water vapour, H_2, and N_2 in anode outlet mixture are expressed as:

$$V_{s,H_2O} = \frac{P_{an,out,VH_2O}}{P_{an,out}} \tag{6.33}$$

$$V_{s,H_2} = \frac{\dot{m}_{an,out,H_2} M_{H_2O} P_{an,out,VH_2O}}{\dot{m}_{an,out,VH_2O} M_{H_2} P_{an,out}} \tag{6.34}$$

$$V_{s,N_2} = \frac{\dot{m}_{an,out,N_2} M_{H_2O} P_{an,out,VH_2O}}{\dot{m}_{an,out,VH_2O} M_{N_2} P_{an,out}} \tag{6.35}$$

6.2 Operation Control of Ejector-based HSRS

The PEMFC control is to provide the optimal operation for the anode H_2 fuel gas and cathode oxidant air delivery by regulating the balance of plant (BOP) components. If the

control strategy is designed properly, the fuel pressure and mass flow rate can be maintained stably with fast response. In this research, a PEMFC system controller and HSRS component models are developed. Integrated with the PEMFC stack model and air supply system model presented by [7], a closed-loop simulator of the PEMFC system is completed, as shown in Figure 56. The system model can simulate different HSRS structures by configuring the system constant values, easily switched between the conventional single nozzle ejector, dual-ejector, and nested-nozzle ejector with or without bypass.

The inputs of the PEMFC system controller consist of stack net power and operating conditions of the PEMFC stack, including the calculated anode inlet pressure, cathode inlet pressure, air stoichiometric ratio, and stack accessory power. In addition, the actuation values of proportional valves, including the opening value k_v and state of the valve's opening and close, and the voltage of the air compressor, are outputs of the controller, as well as the calculated state values of system components models such as stack total power, current, voltage, accessories power, and the pressure, temperature, mass flow rate, gas species at anode and cathode.

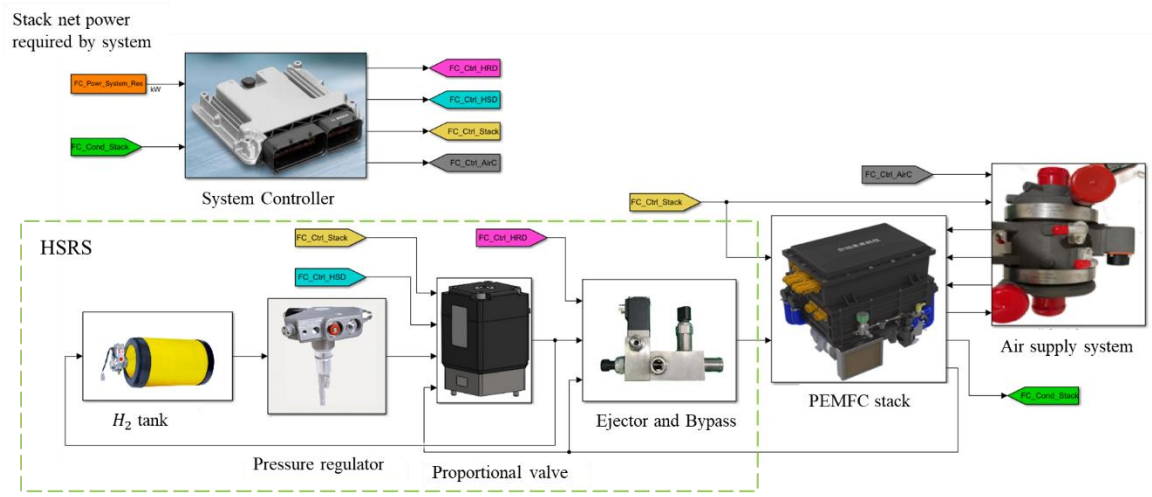

Figure 56: Flow diagram of the closed-loop simulation of a PEMFC system

6.2.1 Control Strategy of HSRS

The PEMFC system controller consists of the HSRS controller and air supply system controller, as shown in Figure 57. To study the HSRS dynamics, it is necessary to build a controller for the air supply system. The air supply system adopts feedforward with the

proportional-integral (PI) control method to regulate the air mass flow to a desired O_2 stoichiometric ratio $SR_{O_2} = 2$. Then the cathode inlet pressure can be determined by the different air mass flowrate in various operating conditions at giving cathode flow channel volume. The HSRS applies the state feedback with PI controller to manipulate the anode inlet pressure according to the cathode inlet pressure. The anode inlet pressure is controlled within a certain difference from the cathode inlet pressure to ensure stable output power and maintain the pressure balance of the membrane. The valve opening value of PVs k_v is calculated by the HSRS controller and transferred to the proportional valve model to adjust the mass flow rate of pure H_2 delivered to the fuel cell stack. Together with the entrained secondary mixture mass flow, the anode inlet pressure is corrected.

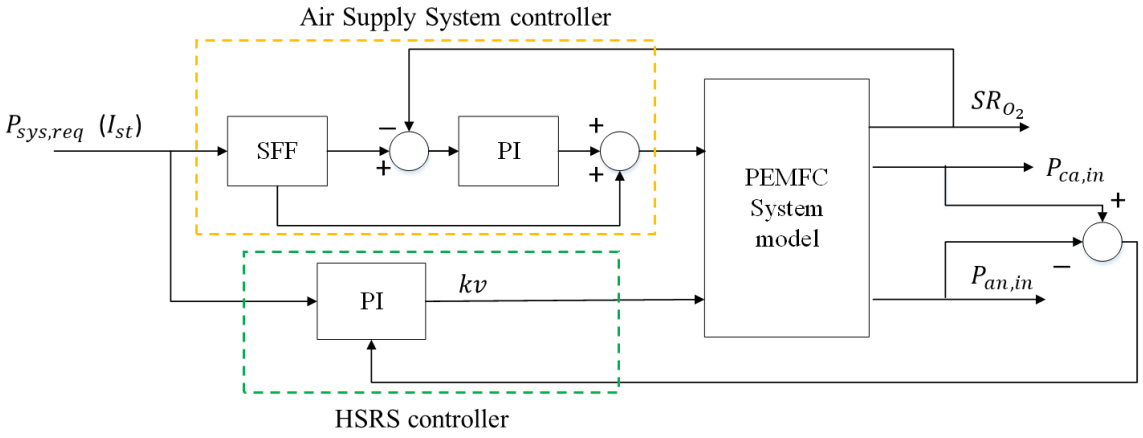

Figure 57: Control strategies of the PEMFC system

Specifically, a rule-based control strategy is developed for the HSRS controller to regulate the PVs during dynamic load changes, as shown in Figure 58. According to the PEMFC system required stack total power $P_{sys,req,t(i)}$, the system determines which H_2 proportional valve is involved for fuel delivery. As discussed in Chapter 4, a critical power P_{switch} can be determined after the multi-ejector or nested-nozzle ejector is designed. When $P_{sys,req,t(i)}$ is larger than P_{switch}, PV1 is activated for the large ejector or large nozzle of the nested-nozzle ejector. When $P_{sys,req,t(i)}$ is below P_{switch}, PV2 is activated for the small ejector or small nozzle of the nested-nozzle ejector. To broaden the ejector working range, a bypass with PV3 is applied in HSRS. Hence, when the required mass flow rate $\dot{m}_{sys,req,t(i)}$ at current power exceeds the maximal mass flow $\dot{m}_{prv,max}$ of PV1 or PV2, PV3 is activated to supply the mass flow difference through the bypass. In addition,

when system required power undergoes an instant and dramatic increase, PV3 can provide plentiful H_2 gas to ensure the rapid dynamic responses. According to the difference between anode inlet pressure and cathode inlet pressure, the valve opening of operating PV k_v is calculated by PI control.

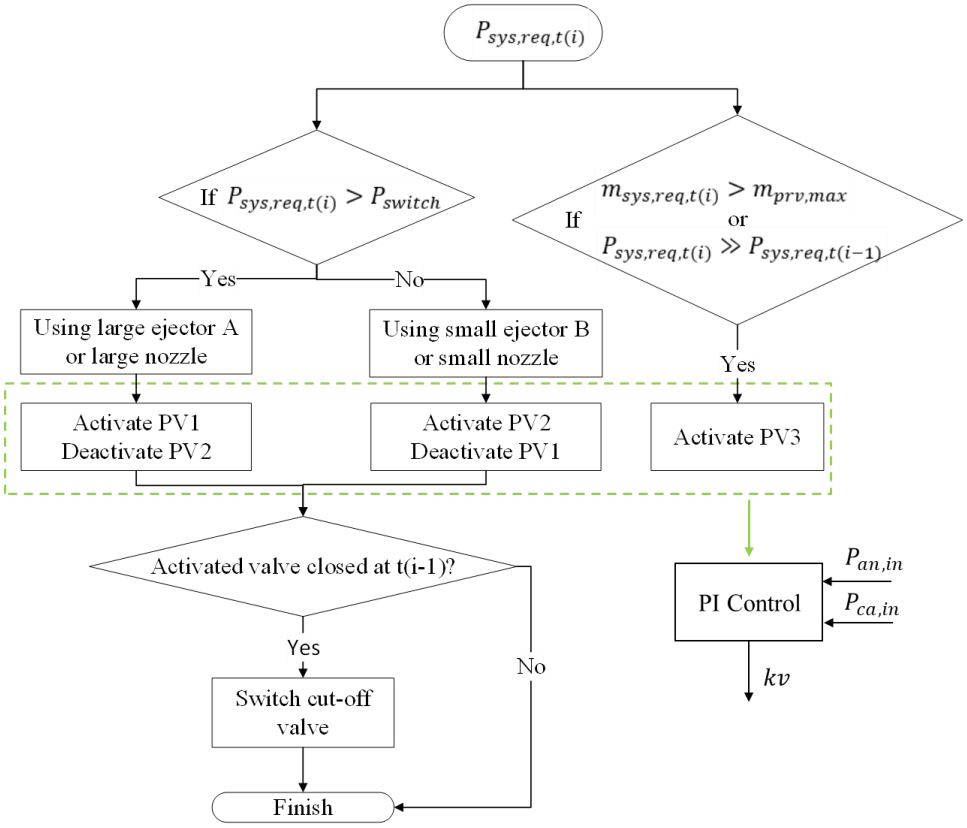

Figure 58: Rule-based control strategy of HSRS

6.2.2 Dynamic Simulation Results and Analysis

The PEMFC system adopts two 75kW fuel cell stacks [50] connected in series to form a 150kW PEMFC system. The two stacks share one HSRS, as mentioned in Chapter 4, including one nested-nozzle ejector, three PVs, one bypass and one pressure regulator. The transient behaviours of the closed-loop system are evaluated by manipulating the dynamic models of system components.

A series of step changes in required stack net power $P_{net,sys,req}$ is used as input for this closed-loop PEMFC system simulator, as shown in Figure 59(a). The stack output power is the sum of stack net power required by the PEMFC system and the parasitic power mainly consumed by the air compressor and cooling water pump. In Figure 59(a), the

simulator accurately calculates the stack output power to follow the system power request. Figure 59(b) shows the stack current, voltage, and efficiency. The stack efficiency is confirmed within the 60% to 70% range from 20 to 150 kW. Since two fuel cell stacks are connected in series, the stack output voltage doubles single stack voltage, ranging from 580 to 670 V, and the output current is around 35 to 260 A.

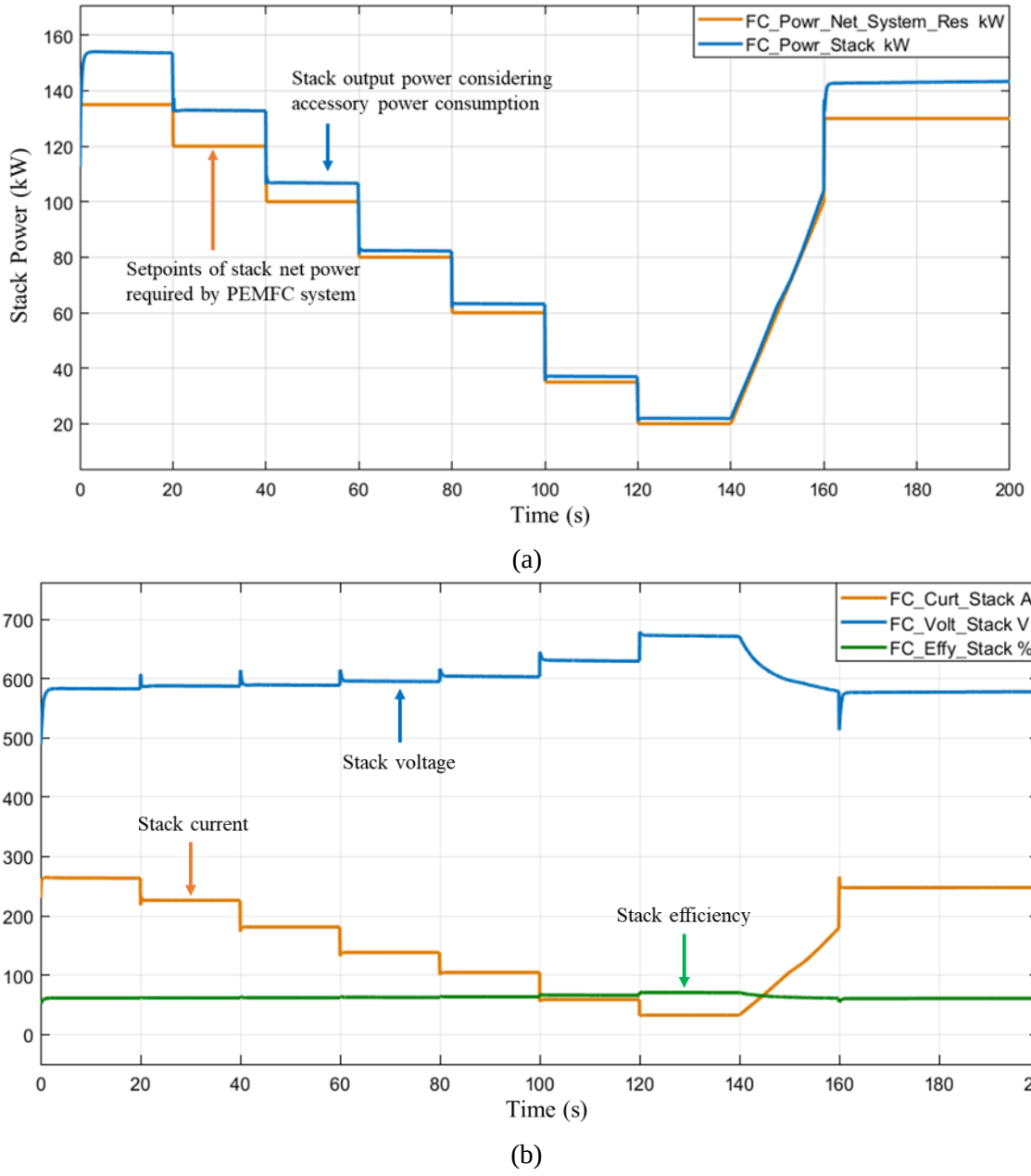

Figure 59: Simulation results of (a) stack output power; (b) stack current, voltage, and efficiency

By taking advantage of the feedforward with PI control of air supply system, the O_2 stoichiometric ratio is controlled to the desired valve $SR_{O_2} = 2$ with fast response. When the $P_{net,sys,req}$ decreases, the O_2 stoichiometric ratio firstly increases because there exists unconsumed O_2, and then quickly drops since the excess O_2 is depleted to maintain the desired SR_{O_2} at lower required system power, as shown in Figure 60(a). The dynamic response of SR_{O_2} also results in similar transient behaviour of stack voltage (Figure 59(b)).

HSRS control aims to balance the pressure difference between the anode and cathode sides to ensure accurate and safe operation. Advanced proportional control solenoid valves applied in HSRS can precisely and quickly adjust its PWM control signal to a desiredH_2 mass flow rate. Therefore, using a PI controller, the anode pressure can quickly respond to the dynamic change of cathode inlet pressure. As shown in Figure 60(b), the cathode inlet pressure is determined by the calculated SR_{O_2}, and the anode inlet pressure perfectly follows the cathode pressure at different system-required power. According to the anode inlet pressure and channel volume, the H_2 stoichiometric ratio is calculated as shown in Figure 60(a). Stack low load has a large H_2 stoichiometric ratio to maintain a certain anode pressure and remove the liquid water in the channels.

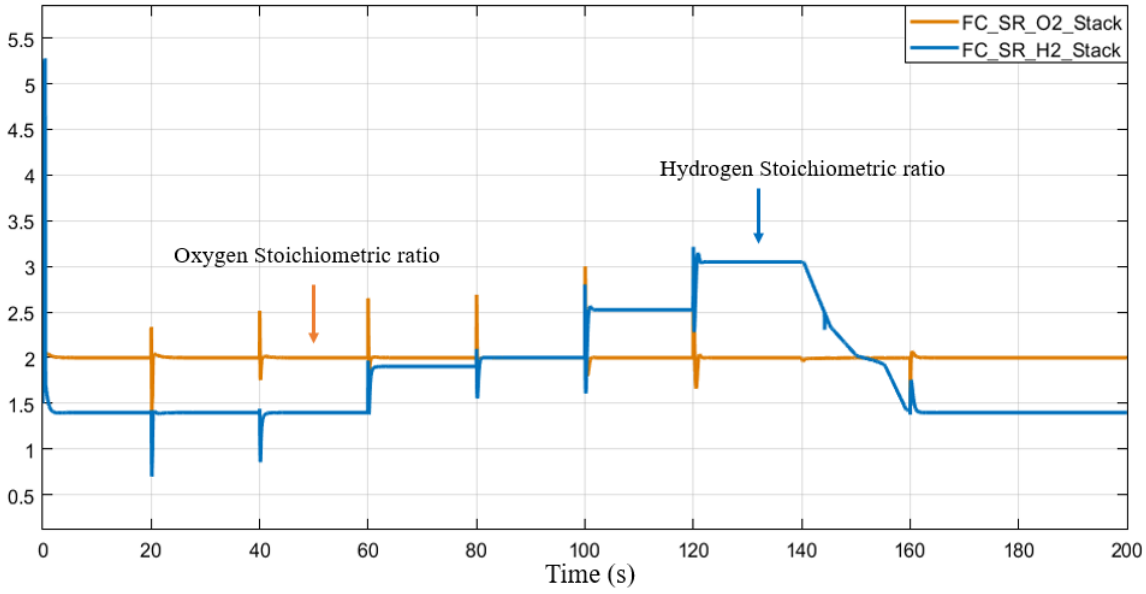

(a)

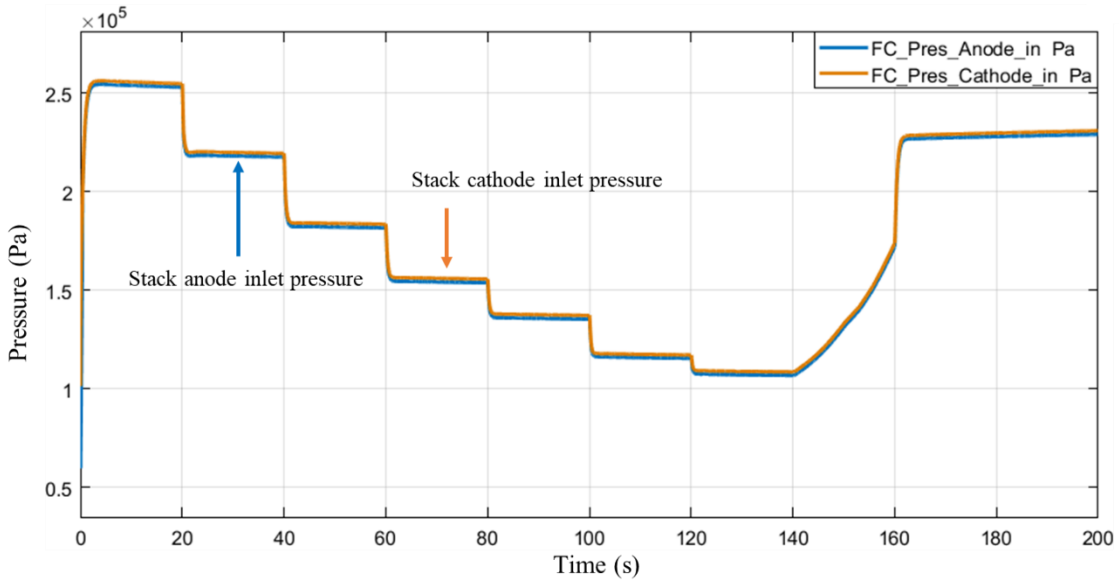

(b)

Figure 60: Simulation results of (a) oxygen and hydrogen stoichiometric ratio; (b) anode inlet pressure and cathode inlet pressure

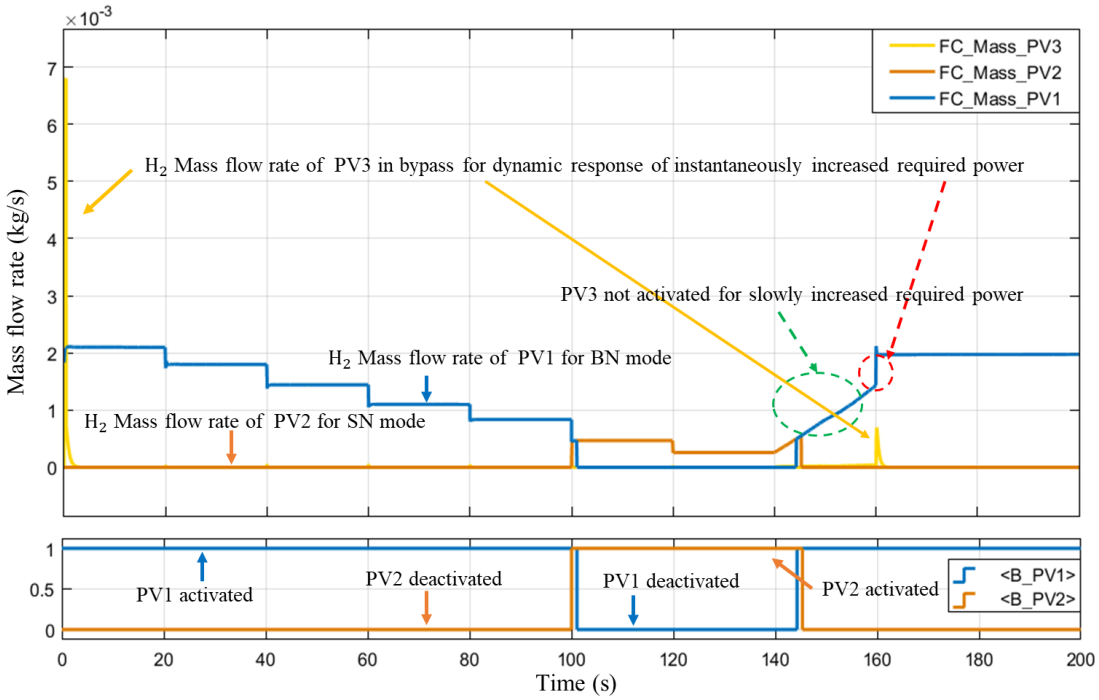

Figure 61: Simulation results of hydrogen mass flow rate of PVs

The nested-nozzle ejector is applied in this simulation. Each nozzle has an independent PV. The switching power point P_{switch} is set at 40 kW during the switching range between the BN and SN modes designed in Chapter 4. It can be seen that when the system output

power (in Figure 59(a)) is larger than P_{switch}, the PV1 is activated to supply the high-pressure H_2 and PV2 is deactivated, and vice versa, as shown in Figure 61.

Figure 61 also shows the simulation results of H_2 mass flow rate delivered by PVs. It can be observed the PV3 in bypass is activated at the beginning of the simulation and provides abundant H_2 mass flow to support the PV1 build the anode inlet pressure, and similar behaviour can be seen at 160s (red dash circle) as $P_{net,sys,req}$ increases instantaneously. When the $P_{net,sys,req}$ increases slowly between 140s and 160s (green dash circle), the PV3 is deactivated because other PVs can follow the dynamic response of the system power and supply enough H_2 mass.

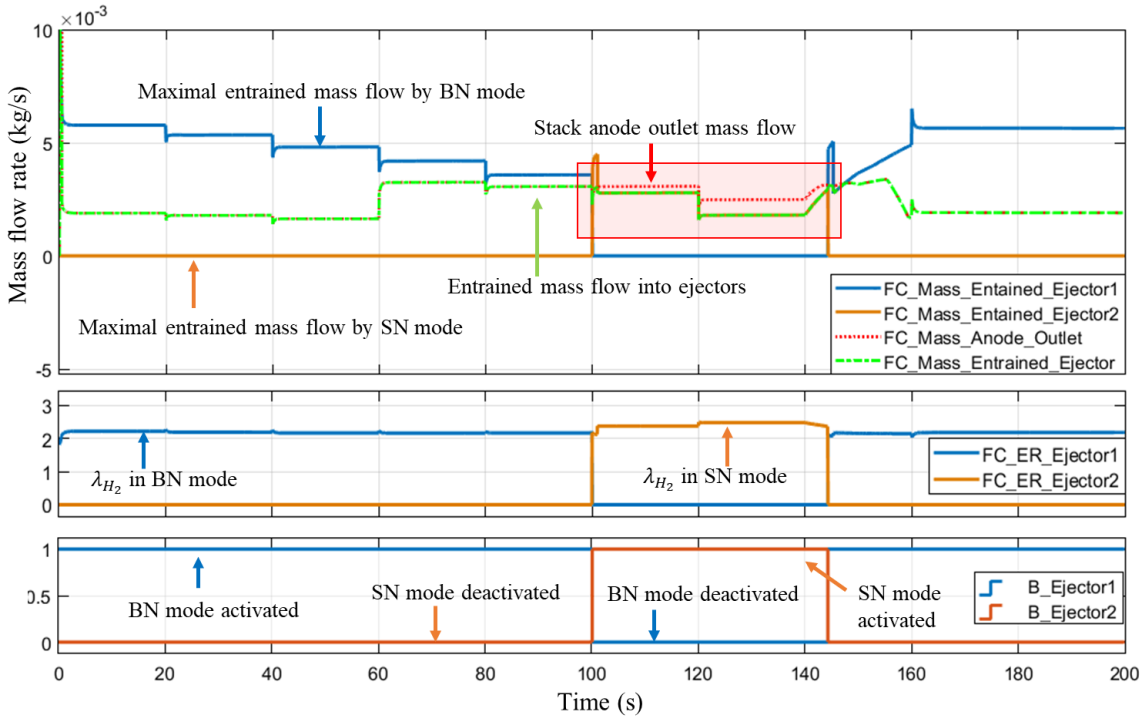

Figure 62: Simulation results of entrainment performance of nested-nozzle ejector

Figure 62 presents the H_2 entrainment performance of nested-nozzle ejector. The large nozzle (BN mode) provides H_2 entrainment capability λ_{H_2} of 2.05 to 2.15 at stack power range from 40 to 150 kW, while the λ_{H_2} of small nozzle is between 2.35 and 2.45 at stack power from 30 to 40 kW. Hence, the maximal secondary mass flow entrained by BN and SN mode can be represented by the solid blue line and solid orange line according to the λ_{H_2}, as shown in Figure 62. When the anode outlet mass flow (red dash line) is below the maximal entrained secondary mass flow, all the anode outlet mixture can be pumped into

the ejector. However, as the anode outlet mass flow is larger than the maximal entrained mass flow (red rectangle area), the excessive mass flow should be removed from the purge valve.

6.3 Summary

In this chapter, the dynamic models of HSRS components are developed using the model-based design method. The rule-based controllers for the air supply system (feedforward with PI) and HSRS system (feedback with PI) are developed and integrated with the PEMFC system models to form a closed-loop simulator. The transient system behaviour is validated in a 150 kW PEMFC system with a nested-nozzle ejector and one bypass. The simulation results demonstrate that the control strategies can provide a quick dynamic response of stack state variables, including cathode pressure, anode pressure, mass flow rate supplied by PV, O_2 stoichiometric ratio, H_2 stoichiometric ratio, and stack power, current, voltage and efficiency.

Chapter 7 Conclusions

7.1 Summary

This research investigated the ejector-based HSRS for the PEMFC system through simulation, modelling, and testing. The ejector theoretical background, analytic models, and different structures were reviewed, as well as the HSRS architectures. The key geometric parameters and operating conditions for single nozzle ejectors were investigated using CFD simulations to analyze their effects on the ejector's H_2 entrainment performance. However, the results demonstrated the conventional single nozzle ejector could only perform in a limited PEMFC system power operating range.

The nested-nozzle ejector was designed to satisfy the PEMFC stack anode H_2 stoichiometric ratio during the full operation of a PEMFC stack from idle power 13.9 kW to a maximum of 150 kW. The nested-nozzle ejector includes one large nozzle (BN) and one small nozzle (SN) nested inside the big nozzle chamber. The two coaxial nozzles share the common suction chamber, mixing chamber and diffuser chamber. A bypass was applied to overcome the mass flow limitations of PV and design a smaller D_{BN} to provide a higher pressure potential energy, thus, an extended fuel cell power operating range can be achieved. The optimal ejector geometric parameters, including D_{BN}, D_{SN}, L_n, D_m and L_m, are obtained using CFD simulations, considering nozzle wall thickness. The nested-nozzle ejector sample is manufactured and two test benches using air as working fluid were built to validate the ejector entrainment performance and anode inlet pressure fluctuation, respectively. The experimental results of ejector air entrainment capabilities have shown good consistency with the CFD simulations, resulting in MAPE of 5.51% and 10.28% for BN and SN mode. Moreover, it also verified the CFD simulation approach adopted in this research is reliable and feasible for ejector designs. Compared to the dual-ejector system, although the H_2 entrainment performance of nested-nozzle ejector was slightly smaller during low operating range, the measured system pressure fluctuation of nested-nozzle ejector during shifting between BN and SN was negligible.

A supervised machine learning (ML) model was developed using data-driven approach adopting massive CFD simulation results. The linear regression model can predict the ejector H_2 entrainment performance for both conventional ejector and newly designed

nested-nozzle ejector with accurate results of less than 10% MAPE and greatly reduced simulation time. Moreover, a linear programming (LP) optimization problem is formulated based on the developed ML model to obtain the optimal ejector geometric parameters. The H_2 entrainment performance of the optimized ejectors for three PEMFC stacks (large-size 150 kW, mid-size 84 kW and small-size 24 kW) was validated by CFD simulation and demonstrated high accuracy of less than 8% mean absolute percentage error. Thus, the proposed method can substitute the conventional design method using trail-and-error through CFD simulation.

The modelling and control of the H_2 supply and recirculation system (HSRS) with different configurations, including dual-ejector and nested-nozzle ejector, with or without bypass, were conducted in MATLAB/Simulink using a model-based design method. In addition, a closed-loop simulation of the PEMFC system was built to investigate the system performance using a rule-based control strategy. The air supply system controller adopted feedforward and feedback with PI control, while the HSRS used feedback and PI control methods. The simulation results of a 150 kW PEMFC system have demonstrated that the system model can provide rapid dynamic responses during transit load conditions.

7.2 Research Contributions

The main contributions of this research include:

1) analyzed and identified the main factors that affect ejector performance, including geometric parameters and operation conditions, using CFD simulations based on a thorough understanding of the ejector's working principles;
2) optimally designed a novel structure of ejector with nested nozzles to provide the effective H_2 gas entrainment capabilities during the full range of PEMFC stack power operations;
3) investigated the nested-nozzle ejector H_2 entrainment performance and pressure stability through simulation and test;
4) developed a machine learning model of ejector using a data-driven approach to predict its H_2 entrainment performance with high accuracy and reduced simulation time;
5) designed an optimization method to obtain the optimal ejector geometries by solving a formulated linear programming (LP) problem;

6) built the anode supply and recirculation system model and controller using a model-based design method to form a closed-loop PEMFC system simulator, which can be used to evaluate the system performance.

7.3 Future Work

The optimally designed nested-nozzle ejector has been tested using air as working gas. Since hydrogen has different physical properties from the air, it is necessary to experiment with the ejector performance with hydrogen as a working fluid. In the future, the nested-nozzle ejector needs to be installed in the PEMFC stack and tested under real operating conditions to investigate the full H_2 entrainment performance.

More data from CFD simulations and experiments will be collected for the training and validation process to improve the accuracy of a linear regression model.

The temperature changes are not considered during the H_2 discharge process in the current HSRS accessories models, such as storage tank, pressure regulator and proportional valve. However, the temperature can affect the operation of these components. It is necessary to capture the dynamic temperature response associated with the pressure change. Besides, the pressure regulator and proportional valve are modelled using static characteristic maps or equations. In the future, physical models based on the geometric parameters of components inside these valves will be built using conservation equations of mass, momentum, and energy to present dynamic behaviours of pressure and temperature. Besides, anode pressure drop greatly influences ejector performance and is strongly determined by the condition parameters of the PEMFC anode flow channel. Hence, a realistic anode flow channel model instead of a look-up table will be established to describe the dynamic changes of anode pressure drop.

Bibliography

[1] NASA, "Global Warming vs. Climate Change," *https://climate.nasa.gov/global-warming-vs-climate-change/*, Sep. 1, 2022.

[2] "The Paris Agreement," *2018 United Nations Framework Convention on Climate Change*.

[3] U. EPA, "Global Greenhouse Gas Emissions Data," *https://www.epa.gov/ghgemissions/global-greenhouse-gas-emissions-data*, Feb, 25, 2022.

[4] H. Ritchie, "Road travel," *https://ourworldindata.org/transport*, Sep, 2021.

[5] U. EPA, "Sources of Greenhouse Gas Emissions," *https://www.epa.gov/ghgemissions/sources-greenhouse-gas-emissions*, Aug. 5, 2022.

[6] D. L. Bleviss, "Transportation is critical to reducing greenhouse gas emissions in the United States," *Wiley Interdisciplinary Reviews: Energy and Environment*, vol. 10, no. 2, p. e390, 2021.

[7] J. T. Pukrushpan, *Modeling and control of fuel cell systems and fuel processors*. University of Michigan Ann Arbor, Michigan, USA, 2003.

[8] A. D. James Larminie, "Fuel Cell Systems Explained," 2000.

[9] M. M.Mench, "Fuel Cell Engines," 2008.

[10] B. James, "2018 Cost Projections of PEM Fuel Cell Systems for Automobiles and Meduium-Duty Vehicles," *US Department of Energy*, 2018.

[11] H. Yumiya, M. Kizaki, and H. Asai, "Toyota fuel cell system (TFCS)," *World Electric Vehicle Journal*, vol. 7, no. 1, pp. 85-92, 2015.

[12] F. Barbir and H. Görgün, "Electrochemical hydrogen pump for recirculation of hydrogen in a fuel cell stack," *Journal of Applied Electrochemistry*, vol. 37, no. 3, pp. 359-365, 2007.

[13] I. Eames, S. Aphornratana, and H. Haider, "A theoretical and experimental study of a small-scale steam jet refrigerator," *International journal of refrigeration*, vol. 18, no. 6, pp. 378-386, 1995.

[14] Y. Yin, M. Fan, K. Jiao, Q. Du, and Y. Qin, "Numerical investigation of an ejector for anode recirculation in proton exchange membrane fuel cell system," *Energy conversion and management*, vol. 126, pp. 1106-1117, 2016.

[15] Q. Zhang, J. Feng, Q. Zhang, and X. Peng, "Performance prediction and evaluation of the scroll-type hydrogen pump for FCEVs based on CFD–Taguchi method," *International Journal of Hydrogen Energy*, vol. 44, no. 29, pp. 15333-15343, 2019.

[16] M. Kim, W.-Y. Lee, and C.-S. Kim, "Development of the Variable Multi-ejector for a Mini-bus PEMFC System," *ECS Transactions*, vol. 5, no. 1, pp. 773-780, 2007.

[17] E. Hosseinzadeh, M. Rokni, M. Jabbari, and H. Mortensen, "Numerical analysis of transport phenomena for designing of ejector in PEM forklift system," *International journal of hydrogen energy*, vol. 39, no. 12, pp. 6664-6674, 2014.

[18] J. He, J. Ahn, and S.-Y. Choe, "Analysis and control of a fuel delivery system considering a two-phase anode model of the polymer electrolyte membrane fuel cell stack," *Journal of Power Sources*, vol. 196, no. 10, pp. 4655-4670, 2011.

[19] L. Chen, K. Xu, Z. Yang, Z. Yan, and Z. Dong, "Optimal Design and Operation of Dual-Ejector PEMFC Hydrogen Supply and Circulation System," *Energies,* vol. 15, no. 15, p. 5427, 2022.

[20] D. A. Brunner, S. Marcks, M. Bajpai, A. K. Prasad, and S. G. Advani, "Design and characterization of an electronically controlled variable flow rate ejector for fuel cell applications," *International journal of hydrogen energy,* vol. 37, no. 5, pp. 4457-4466, 2012.

[21] T. Sugawara, S. Kizaki, and Y. Nuiya, "Variable flow-rate ejector and fuel cell system having the same," ed: Google Patents, 2005.

[22] T. Meakhail, Y. Zien, M. Elsallak, and S. AbdelHady, "Experimental study of the effect of some geometric variables and number of nozzles on the performance of a subsonic air—Air ejector," *Proceedings of the Institution of Mechanical Engineers, Part A: Journal of Power and Energy,* vol. 222, no. 8, pp. 809-818, 2008.

[23] H. Xue, L. Wang, H. Zhang, L. Jia, and J. Ren, "Design and investigation of multi-nozzle ejector for PEMFC hydrogen recirculation," *International journal of hydrogen energy*, vol. 45, no. 28, pp. 14500-14516, 2020.

[24] J. Han, J. Feng, T. Hou, and X. Peng, "Performance investigation of a multi‐nozzle ejector for proton exchange membrane fuel cell system," *International Journal of Energy Research,* vol. 45, no. 2, pp. 3031-3048, 2021.

[25] Z. Du, Q. Liu, X. Wang, and L. Wang, "Performance investigation on a coaxial-nozzle ejector for PEMFC hydrogen recirculation system," *International Journal of Hydrogen Energy,* vol. 46, no. 76, pp. 38026-38039, 2021.

[26] L. Zhu, J. Yu, M. Zhou, and X. Wang, "Performance analysis of a novel dual-nozzle ejector enhanced cycle for solar assisted air-source heat pump systems," *Renewable energy*, vol. 63, pp. 735-740, 2014.

[27] J. Keenan and E. Neumann, "A simple air ejector," 1942.

[28] J. H. Keenan, E. P. Neumann, and F. Lustwerk, "An investigation of ejector design by analysis and experiment," *Journal of Applied Mechanics,* vol. 17, no. 3, pp. 299-309, 1950.

[29] L. Defrate and A. Hoerl, "Optimum design of ejector using digital computers," in *Chem. Eng. Prog. Symp. Ser*, 1959, vol. 55, no. 21, p. 12.

[30] G. Emanuel, "Optimum performance for a single-stage gaseous ejector," *AIAA Journal,* vol. 14, no. 9, pp. 1292-1296, 1976.

[31] B. Huang, J. Chang, C. Wang, and V. Petrenko, "A 1-D analysis of ejector performance," *International journal of refrigeration,* vol. 22, no. 5, pp. 354-364, 1999.

[32] C. Liao, *Gas ejector modeling for design and analysis*. Texas A&M University, 2008.

[33] Y. Zhu, W. Cai, C. Wen, and Y. Li, "Shock circle model for ejector performance evaluation," *Energy Conversion and Management*, vol. 48, no. 9, pp. 2533-2541, 2007, doi: 10.1016/j.enconman.2007.03.024.

[34] Y. Zhu and Y. Li, "New theoretical model for convergent nozzle ejector in the proton exchange membrane fuel cell system," *Journal of Power Sources,* vol. 191, no. 2, pp. 510-519, 2009.

[35] J. John D. Aderson, "Fundamentals of AERODYNAMICS," 2010.

[36] G. Besagni, R. Mereu, and F. Inzoli, "Ejector refrigeration: A comprehensive review," *Renewable and Sustainable Energy Reviews*, vol. 53, pp. 373-407, 2016, doi: 10.1016/j.rser.2015.08.059.

[37] Y. Bartosiewicz, Z. Aidoun, P. Desevaux, and Y. Mercadier, "Numerical and experimental investigations on supersonic ejectors," *International Journal of Heat and Fluid Flow*, vol. 26, no. 1, pp. 56-70, 2005.

[38] P. Pei *et al.*, "Numerical studies on wide-operating-range ejector based on anodic pressure drop characteristics in proton exchange membrane fuel cell system," *Applied Energy*, vol. 235, pp. 729-738, 2019, doi: 10.1016/j.apenergy.2018.11.005.

[39] S. Riffat and P. Everitt, "Experimental and CFD modelling of an ejector system for vehicle air conditioning," *Journal of the Institute of Energy*, vol. 72, no. 491, pp. 41-47, 1999.

[40] Y. Zhu, W. Cai, C. Wen, and Y. Li, "Numerical investigation of geometry parameters for design of high performance ejectors," *Applied Thermal Engineering*, vol. 29, no. 5-6, pp. 898-905, 2009.

[41] A. Hemidi, F. Henry, S. Leclaire, J.-M. Seynhaeve, and Y. Bartosiewicz, "CFD analysis of a supersonic air ejector. Part I: Experimental validation of single-phase and two-phase operation," *Applied Thermal Engineering*, vol. 29, no. 8-9, pp. 1523-1531, 2009.

[42] F. Mazzelli, A. B. Little, S. Garimella, and Y. Bartosiewicz, "Computational and experimental analysis of supersonic air ejector: Turbulence modeling and assessment of 3D effects," *International Journal of Heat and Fluid Flow*, vol. 56, pp. 305-316, 2015.

[43] K. Nikiforow, P. Koski, H. Karimäki, J. Ihonen, and V. Alopaeus, "Designing a hydrogen gas ejector for 5 kW stationary PEMFC system–CFD-modeling and experimental validation," *International Journal of Hydrogen Energy*, vol. 41, no. 33, pp. 14952-14970, 2016.

[44] A. Maghsoodi, E. Afshari, and H. Ahmadikia, "Optimization of geometric parameters for design a high-performance ejector in the proton exchange membrane fuel cell system using artificial neural network and genetic algorithm," *Applied Thermal Engineering*, vol. 71, no. 1, pp. 410-418, 2014.

[45] Q. Ding, K.-Q. Zhu, C. Yang, X. Chen, Z.-M. Wan, and X.-D. Wang, "Performance investigation of proton exchange membrane fuel cells with curved membrane electrode assemblies caused by pressure differences between cathode and anode," *International Journal of Hydrogen Energy*, vol. 46, no. 75, pp. 37393-37405, 2021.

[46] S. University, "Machine Learning and AI via Brain simulations," 2019-08-01.

[47] S. P. B. Michael C. Grant, "The CVX Users' Guide Release 2.2," Jan. 28 2020.

[48] "TESCOMTM Pressure Reducing Regulators," *Emerson.com*.

[49] P. Pei, M. Ouyang, W. Feng, L. Lu, H. Huang, and J. Zhang, "Hydrogen pressure drop characteristics in a fuel cell stack," *International Journal of Hydrogen Energy*, vol. 31, no. 3, pp. 371-377, 2006.

[50] J. A. Adams, W.-c. Yang, K. A. Oglesby, and K. D. Osborne, "The development of Ford's P2000 fuel cell vehicle," *SAE transactions*, pp. 1634-1645, 2000.